석사 학위논문
Master's Thesis

수중터널의 내진해석을 위한 수치해석기법 개발

Numerical method for seismic analysis of submerged floating tunnels

김 정 호 (金 政 湖 Kim, Jeong Ho)
기계항공시스템학부 해양시스템공학전공
School of Mechanical, Aerospace and Systems Engineering,
Division of Ocean Systems Engineering

KAIST

2014

수중터널의 내진해석을 위한 수치해석기법 개발

Numerical method for seismic analysis of submerged floating tunnels

Numerical method for seismic analysis of submerged floating tunnels

Advisor : Professor Phill-Seung Lee

by

Jeong Ho Kim

School of Mechanical, Aerospace and Systems Engineering,

Division of Ocean Systems Engineering

KAIST

A thesis submitted to the faculty of KAIST in partial fulfillment of the requirements for the degree of Master of Science and Engineering in the School of Mechanical, Aerospace and Systems Engineering, Division of Ocean Systems Engineering. The study was conducted in accordance with Code of Research Ethics[1]

2013. 12. 23

Approved by

Associate Professor Phill-Seung Lee

____

[1] Declaration of Ethical Conduct in Research: I, as a graduate student of KAIST, hereby declare that I have not committed any acts that may damage the credibility of my research. These include, but are not limited to: falsification, thesis written by someone else, distortion of research findings or plagiarism. I affirm that my thesis contains honest conclusions based on my own careful research under the guidance of my thesis advisor.

수중터널의 내진해석을 위한
수치해석기법 개발

김 정 호

위 논문은 한국과학기술원 석사학위논문으로
학위논문심사위원회에서 심사 통과하였음.

2013 년 12 월 23 일

심사위원장 이 필 승 (인)

심사위원 정 형 조 (인)

심사위원 김 병 완 (인)

MOSE
20123146

김 정 호. Kim, Jeong Ho. Numerical method for seismic analysis of submerged floating tunnels. 수중터널의 내진해석을 위한 수치해석기법 개발. Division of Ocean Systems Engineering. 2014. 96 p. Advisor Prof. Lee, Phill-Seung, Text in English.

ABSTRACT

The purpose of this study is to develop the formulation for 3D hydroelastic analysis of tension leg type submerged floating tunnel (SFT) under seismic ground motion and evaluate numerical solutions for the dynamic response of SFT in time domain. In order to consider fluid-structure interaction, we linearize the Morison equation and apply in terms of hydrodynamic force from relative motion between structure and ground motion. We demonstrate the numerical procedure to solve the problem by finite element discretization of the equation of motion. Continuum mechanics based 3-D beam element is applied to the tunnel modeling. Then, we conduct numerical analysis to the several kilometers SFT model and discuss the structure dynamic response of numerical results.

Keywords: 3D hydroelastic analysis, submerged floating tunnel(SFT), Morison equation, finite element method(FEM), seismic analysis

Table of Contents

Chapter 4. Numerical results and discussion

List of Tables

List of Figures

Chapter 1. Introduction

Connecting two continents or islands has always been considered difficult problem because of crossing great distances of waterways and deep water depth. There are 3 typical ways to connect transportation over the sea; long span bridge, immersed tunnel and underground tunnel. However, all of these typical solutions should satisfy the condition that structure should be fixed on the seabed or ground. For example, long span bridge need to put series of bridge piers out in the ocean, and immersed tunnel also need earthwork underwater to sink tunnel segments on the exact position. These conditions are possible only shallow water condition.

One innovative solution for crossing wide expanse of the ocean could install a tunnel tube which is placed at the middle of the sea water. This type of tunnel is called submerged floating tunnel (SFT), or Archimedes bridges because its dead and live loads are counterbalanced by Archimedes buoyancy (Martire, 2000). There are four principle types of SFT in Fig. 1, tension leg type has considered suitable for any length and water depth (Østlid, 2010).

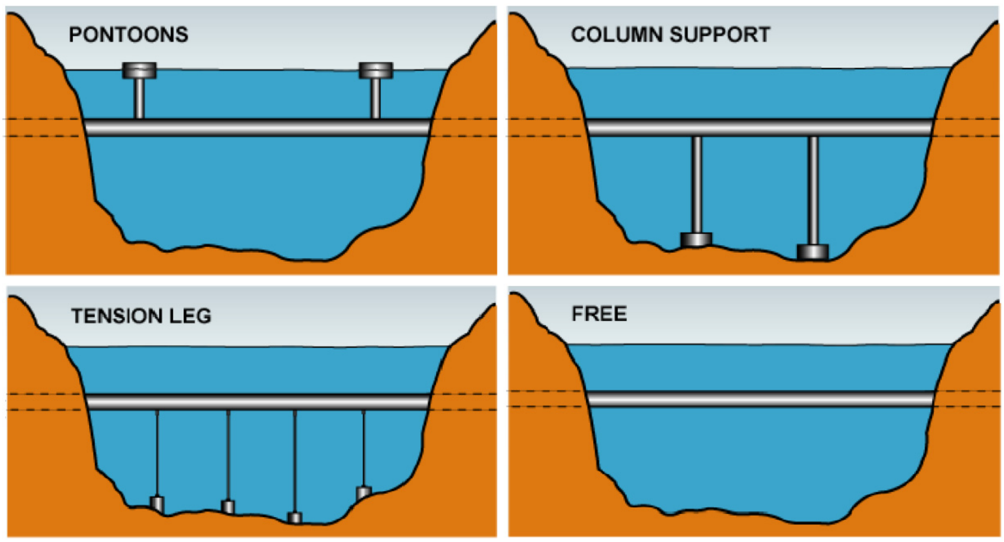

Fig. 1. Principle types of SFT (Østlid, 2010)

The strengths of SFT compare with other types of structure are as follows:

- The shortest route relative to other structure types (bridges, immersed tunnel, etc.).
- SFT is located at the specific depth which can minimize the effect of seabed condition, earthquake, surface wave, wind, etc.
- SFT have no obstruction to ship traffic to pass on water surface.
- SFT can reduce the construction space, cost and period.

Based on the strengths discussed, many countries have developed several concepts and ideas of SFTs previously. In the 1880s, the concept of SFT is proposed for the first time in England. From the late 1960s to 1980s, many research institutes in Europe performed studies about SFT design and engineering system for each Strait of Messina in Italy and fjords in Norway. Recently, China and Italy organized joint research laboratory in 2004, for the realization of the first SFT prototype in Qiandao Lake, China (Mazzolani et al., 2008).

But, so far, no SFT has been constructed anywhere because it has complicated interaction with its external environment and internal traffic load, and it has never been tested experimentally. This is major difference compare with bottom mounted structures, SFT demands new technology for the analysis of its dynamic structure behavior caused by ocean environments. Since SFT is surrounded by water, surface wave and current will effect to the structure as hydrodynamic loads. Also, earthquake from seabed is applied through the tension leg cable, it should consider fluid-structure interaction.

Since SFT is several kilometers long and its cross-section is relatively too small, we should analyze not only rigid body motion but also elastic motion. So, hydroelastic analysis is necessary to estimate exact behavior of SFT. Nevertheless, only few studies have been performed on the hydroelastic behavior of full-model SFT. For example, the dynamic behavior under seismic and wave excitation of a tunnel model is investigated, which is applied to the crossing of the Messina Strait, characterized by a total length of 4680 m and a maximum depth of about 285 m (Pilato et al., 2008). However, it focused on the anchoring system, whose behavior is assumed of extreme importance in determining the overall structural dynamic response, and it neglected longitudinal deformation and torsional behavior of tunnel. Ge et al. (2010) investigated the dynamic behavior under wave excitation of a Qiandao Lake prototype model in China, which is much smaller: a total length of 100 m and average depth of water about 17 m. Its dynamic behavior is solved in frequency domain. A hydroelastic model of SFT is presented based on three-dimensional finite element model, fluid-structural interaction is solved using boundary element method (BEM) (Ge et al., 2010).

In this study, a formulation for 3D hydroelastic analysis of tension leg type SFT under seismic ground motion has been developed. We focus on a dynamic behavior of SFT in time domain, especially under seismic ground motion from seabed. Seismic effect can be a severe risk for the safety of SFT. In order to consider fluid-structure interaction effectively, the present formulation estimate hydrodynamic loadings during seismic ground motion by Morison equation. Therefore, structure-fluid relative velocity and acceleration are considered to estimate inertia and drag force. Next, we demonstrate the numerical procedure to solve the problem by finite element discretization of the equation of motion. Finally, we apply it to the several kilometers SFT model and discuss the structure dynamic response of numerical results.

Chapter 2. General theory

In this chapter, we describe mathematical formulation of a hydroelastic analysis of SFT. For the structure, stiffness and mass properties of tunnel and tension cables are considered. For external loads, being different from onshore structures, not only seismic ground motion but also hydrodynamic forces by fluid-structure interaction are considered.

Hydrodynamic forces have been developed based on Morison equation to estimate fluid-structure interaction. Therefore, it is applied in terms of inertia force and drag force, these are applied on the tunnel as added mass, added damping, drag force effect. Finally, equation of motion of SFT for seismic ground motion is established.

2.1 Overall description and assumptions

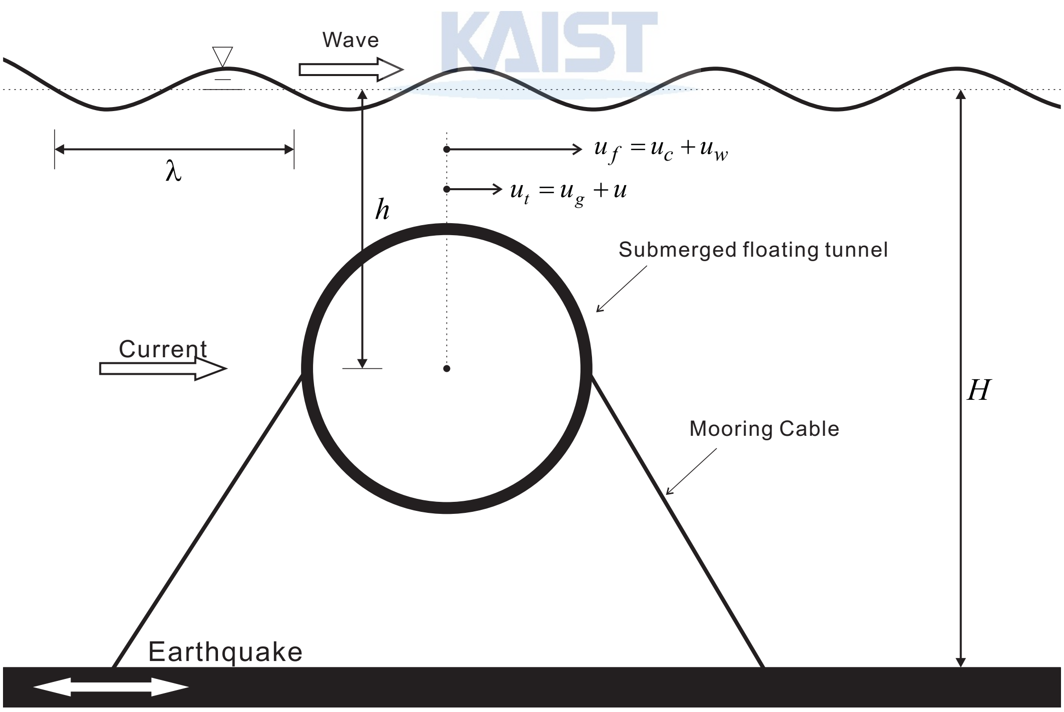

Fig. 2. Hydroelastic model of SFT

SFT is very large submerged floating structure, which is characterized by very long tunnel length compare to its cross-section. Furthermore, SFT is not supported like bottom mounted structures but it floating appropriate depth by tension leg cables which counterbalance the buoyancy. These are main reasons to make the problem complicated.

Fig. 2 provides an overall description of the hydroelastic model of a SFT. Total water depth, depth from water surface to the center of tunnel and wave length are denoted by H, h and λ, respectively. If surface wave and current were applied, fluid displacement u_f will be existed and it consists of fluid displacements cause by current and wave, which is denoted by u_c and u_w, respectively. Also, absolute displacement of tunnel u_t is consist of displacement of seabed u_g and relative displacement of tunnel u.

To solve the hydroelastic behavior of SFT under seismic ground motion, there are some assumptions are as follows:

- Seismic motion is excited only parallel direction to the seabed.
- The same seismic motion is applied to all of supporting points on the seabed.
- Seabed is regarded as a rigid foundation.
- Surface of seabed is frictionless, so it cannot make water flow when seismic motion in parallel direction.
- There are no incident wave or current to surrounded water: still water.
- The structure is assumed to be a homogeneous, isotropic, and linear elastic material with small displacement and strain.
- Tension leg cables are assumed always maintain a straight line.

In addition, Morison equation is commonly used to compute the hydrodynamic forces induced by wind waves and currents on offshore structures but it can be used to roughly estimate hydrodynamic loadings during seismic events, once the water velocities and accelerations due to seaquake are determined (Martire et al., 2010) (Kunisu, 2010).

2.2 Formulation of the hydrodynamic loading

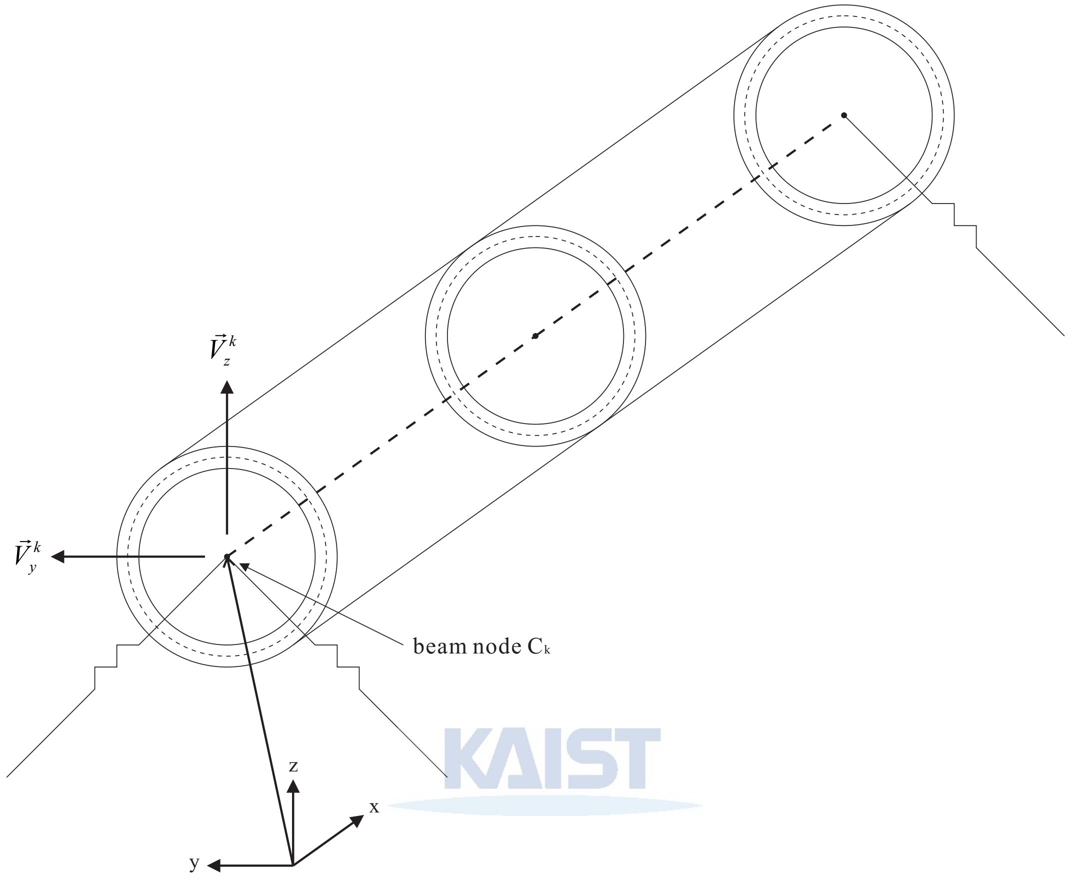

Fig. 3. Coordinate system of SFT

In this part, we describe formulations of hydrodynamic loading based on the Morison equation. By using the Morison equation, we can estimate the hydrodynamic force per unit length acting on a tunnel. Fig. 3 provides a global Cartesian coordinate system of SFT. In this figure, tunnel axis is parallel to the x axis, and tunnel cross-sections are defined by y and z axis.

The general Morison equation for moving body is a function of the components of kinematic vectors, these are relative velocity and acceleration between fluid and structure element (Martinelli et al., 2011), i.e.

$$\vec{f}(t) = \rho_w \frac{\pi D^2}{4}\ddot{\vec{u}}_f^N(t) + \rho_w C_A \frac{\pi D^2}{4}(\ddot{\vec{u}}_f^N(t) - \ddot{\vec{u}}_t^N(t)) + \frac{1}{2}\rho_w C_D D(\dot{\vec{u}}_f^N(t) - \dot{\vec{u}}_t^N(t))^2 \cdot sign(\dot{\vec{u}}_f^N(t) - \dot{\vec{u}}_t^N(t)) \tag{1}$$

$$m_w = \rho_w C_A \frac{\pi D^2}{4} \qquad m_a = \rho_w C_A \frac{\pi D^2}{4} \qquad c_w = \frac{1}{2}\rho_w C_D D \tag{2}$$

where $\vec{u}_f^N(t)$ and $\vec{u}_t^N(t)$ are displacement vector of fluid and structure respectively. Superscript N denotes the orthogonal components with respect to the element axis. ρ_w, D, C_A, and C_D are fluid density, external diameter of tunnel, added mass coefficient, and drag coefficient, respectively. The first term on the right hand side of Eq. (1) represents the inertia loading, the second term is added effect and the third term is drag loading with manipulation through the use of sign function to employ directions of relative velocity (Brancaleoni et al., 1989). m_w, m_a, and c_w are constant values of each terms in Eq. (1).

Because we assume that there are no flow in surrounding fluid, we obtain

$$\vec{u}_f(t) = \dot{\vec{u}}_f(t) = \ddot{\vec{u}}_f(t) \approx 0 \tag{3}$$

By applying Eqs. (2)-(3), Eq. (1) becomes

$$\vec{f}(t) = -m_a \ddot{\vec{u}}_t^N(t) - c_w\{\dot{\vec{u}}_t^N(t)\}^2 \cdot sign(\dot{\vec{u}}_t^N(t)) \tag{4}$$

where absolute displacement vector of structure $\vec{u}_t(t)$ can be separated by ground displacement vector $\vec{u}_g(t)$, and relative displacement vector of structure $\vec{u}(t)$. It is also applied to velocity and acceleration, i.e.

$$\vec{u}_t(t) = \vec{u}_g(t) + \vec{u}(t) \qquad \dot{\vec{u}}_t(t) = \dot{\vec{u}}_g(t) + \dot{\vec{u}}(t) \qquad \ddot{\vec{u}}_t(t) = \ddot{\vec{u}}_g(t) + \ddot{\vec{u}}(t) \tag{5}$$

Then, Eq. (4) can be expressed

$$\vec{f}(t) = -m_a(\ddot{\vec{u}}_g^N(t) + \ddot{\vec{u}}^N(t)) - c_w\{\dot{\vec{u}}_g^N(t) + \dot{\vec{u}}^N(t)\}^2 \cdot sign(\dot{\vec{u}}_g^N(t) + \dot{\vec{u}}^N(t)) \tag{6}$$

The structure displacement and strain are assumed small, the square of structure displacement term in drag loading is neglected. Then, Eq. (6) is derived

$$\vec{f}(t) = -m_a(\ddot{\vec{u}}_g^N(t) + \ddot{\vec{u}}^N(t)) - c_w(\{\dot{\vec{u}}_g^N(t)\}^2 + 2\dot{\vec{u}}_g^N(t)\dot{\vec{u}}^N(t)) \cdot sign(\dot{\vec{u}}_g^N(t) + \dot{\vec{u}}^N(t)) \tag{7}$$

By rearranging the right hand side of Eq. (7), the hydrodynamic force per unit length acting on the tunnel can be stated as

$$\vec{f}(t) = -m_a\ddot{\vec{u}}^N(t) \tag{8a}$$
$$- m_a\ddot{\vec{u}}_g^N(t) \tag{8b}$$
$$- 2c_w\dot{\vec{u}}_g^N(t)\dot{\vec{u}}^N(t) \cdot sign(\dot{\vec{u}}_g^N(t) + \dot{\vec{u}}^N(t)) \tag{8c}$$
$$- c_w\{\dot{\vec{u}}_g^N(t)\}^2 \cdot sign(\dot{\vec{u}}_g^N(t) + \dot{\vec{u}}^N(t)) \tag{8d}$$

Eqs. (8a)-(8d), each term can be defined as added mass effect, seismic loading by added mass effect, added damping effect, and drag loading, respectively.

Considering the interpolation of displacement, we obtain

$$\vec{u} = \underline{\underline{H}}\vec{U}, \quad \delta\vec{u} = \underline{\underline{H}}\delta\vec{U}, \quad \vec{u}^N = \underline{\underline{N}}\vec{u} = \underline{\underline{N}}\,\underline{\underline{H}}\vec{U}, \quad \vec{u}_g^N = \underline{\underline{N}}\vec{u}_g, \tag{9}$$

To interpolate $\vec{u}^N$, we use matrix $\underline{\underline{N}}$ which is consist of direction cosines of the tangent to the tunnel axis. It can determine only normal components of the element displacement vector (Martinelli et al., 2011).

$$[N] = \begin{bmatrix} 1-\cos^2\theta_x & -\cos\theta_x\cos\theta_y & -\cos\theta_x\cos\theta_z \\ -\cos\theta_y\cos\theta_x & 1-\cos^2\theta_y & -\cos\theta_y\cos\theta_z \\ -\cos\theta_z\cos\theta_x & -\cos\theta_z\cos\theta_y & 1-\cos^2\theta_z \end{bmatrix} \tag{10}$$

Eq. (8a) can be transformed by integrating over the tunnel length as

$$\vec{R}_1(t) = -m_a \int_0^L \underline{\underline{H}}^T \ddot{\vec{u}}^N(t) ds = -m_a \int_0^L \underline{\underline{H}}^T \underline{\underline{N}}\,\underline{\underline{H}} ds \ddot{\vec{U}}(t) = -\underline{\underline{M}}_{added} \ddot{\vec{U}}(t) \tag{11}$$

Then, we can obtain consistent added mass matrix which is proportional to the acceleration of structure motion. Next, Eq. (8b) can be transformed as

$$\vec{R}_2(t) = -m_a \int_0^L \underline{\underline{H}}^T \ddot{\vec{u}}_g^N(t) ds = -m_a \int_0^L \underline{\underline{H}}^T \underline{\underline{N}}\,\underline{\underline{H}} ds \ddot{\vec{U}}_g(t) = -\underline{\underline{M}}_{added} \ddot{\vec{U}}_g(t) \tag{12}$$

Eq. (12) define the seismic force by added mass effect which is proportional to the acceleration of ground motion. Ground motion is known at all location and time. Also, Eqs. (8c)-(8d) can be expressed as

$$\begin{aligned} \vec{R}_3(t) &= -2c_w \int_0^L \underline{\underline{H}}^T \dot{\vec{u}}_g^N(t) \cdot sign(\dot{\vec{u}}_g^N(t) + \dot{\vec{u}}^N(t)) \dot{\vec{u}}^N(t) ds \\ &= -2c_w \dot{\vec{u}}_g(t) \cdot sign(\dot{\vec{U}}_g^N(t) + \dot{\vec{U}}^N(t)) \int_0^L \underline{\underline{H}}^T \underline{\underline{N}}\,\underline{\underline{H}} ds \dot{\vec{U}}(t) \\ &= -\underline{\underline{C}}_w(t) \dot{\vec{U}}(t) \end{aligned} \tag{13}$$

$$\begin{aligned} \vec{R}_4(t) &= -2c_w \int_0^L \underline{\underline{H}}^T \{\dot{\vec{u}}_g^N(t)\}^2 \cdot sign(\dot{\vec{u}}_g^N(t) + \dot{\vec{u}}^N(t)) ds \\ &= -2c_w \cdot sign(\dot{\vec{U}}_g^N(t) + \dot{\vec{U}}^N(t)) \int_0^L \underline{\underline{H}}^T \underline{\underline{N}} ds \{\dot{\vec{u}}_g(t)\}^2 \\ &= -\vec{R}_{drag}(t) \end{aligned} \tag{14}$$

Added damping matrix proportional to the velocities of ground and structure can be defined by Eq. (13), and drag loading which is proportional to the square of magnitude of ground velocity on each direction also can be defined by Eq. (14). Finally, hydrodynamic forces from fluid-structure interaction is stated as

$$\begin{aligned} \vec{R}(t) &= \vec{R}_1(t) + \vec{R}_2(t) + \vec{R}_3(t) + \vec{R}_4(t) \\ &= -\underline{\underline{M}}_{added} \ddot{\vec{U}}(t) - \underline{\underline{M}}_{added} \ddot{\vec{U}}_g(t) - \underline{\underline{C}}_w(t) \dot{\vec{U}}(t) - \vec{R}_{drag}(t) \end{aligned} \tag{15}$$

2.3 Formulation of the seismic ground motion for multi-DOF system

To describe the formulation of seismic loading for SFT, we need to consider its supports. The support of SFT is a lot of tension leg cables, which are spaced regularly, from tens to hundreds of meters. So, formulation of seismic excitation is similar to that of long span bridges.

The equation of motion of SFT for seismic excitation loading can be written as

$$\begin{bmatrix} M_{ss} & M_{sg} \\ M_{sg}^T & M_{gg} \end{bmatrix} \begin{Bmatrix} \ddot{\vec{U}}_s^t(t) \\ \ddot{\vec{U}}_g(t) \end{Bmatrix} + \begin{bmatrix} C_{ss} & C_{sg} \\ C_{sg}^T & C_{gg} \end{bmatrix} \begin{Bmatrix} \dot{\vec{U}}_s^t(t) \\ \dot{\vec{U}}_g(t) \end{Bmatrix} + \begin{bmatrix} K_{ss} & K_{sg} \\ K_{sg}^T & K_{gg} \end{bmatrix} \begin{Bmatrix} \vec{U}_s^t(t) \\ \vec{U}_g(t) \end{Bmatrix} = \begin{Bmatrix} \vec{R}(t) \\ 0 \end{Bmatrix} \tag{16}$$

where subscript s and g mean structure and support ground, respectively. And superscript t means absolute value of displacement, velocity, or acceleration. Mass, damping, and stiffness matrix are denoted M, C, and K, respectively. $\vec{R}(t)$ is the external forces that apply to the structure. If we assume that same seismic motion is applied to all of supporting points on the seabed (also called identical support excitation), absolute displacement of structure can be separated by ground displacement, and relative displacement vector of structure. It also applied to velocity and acceleration, i.e.

$$\begin{aligned} &\begin{bmatrix} M_{ss} & M_{sg} \\ M_{sg}^T & M_{gg} \end{bmatrix} \begin{Bmatrix} \ddot{\vec{U}}_s(t) + \ddot{\vec{U}}_g(t) \\ \ddot{\vec{U}}_g(t) \end{Bmatrix} + \begin{bmatrix} C_{ss} & C_{sg} \\ C_{sg}^T & C_{gg} \end{bmatrix} \begin{Bmatrix} \dot{\vec{U}}_s(t) + \dot{\vec{U}}_g(t) \\ \dot{\vec{U}}_g(t) \end{Bmatrix} \\ &\qquad + \begin{bmatrix} K_{ss} & K_{sg} \\ K_{sg}^T & K_{gg} \end{bmatrix} \begin{Bmatrix} \vec{U}_s(t) + \vec{U}_g(t) \\ \vec{U}_g(t) \end{Bmatrix} = \begin{Bmatrix} \vec{R}(t) \\ 0 \end{Bmatrix} \end{aligned} \tag{17}$$

Because of the above mentioned assumption, ground displacement becomes rigid body motion. So, this relation is valid, i.e.

$$\begin{bmatrix} K_{ss} & K_{sg} \\ K_{sg}^T & K_{gg} \end{bmatrix} \begin{Bmatrix} \vec{U}_g(t) \\ \vec{U}_g(t) \end{Bmatrix} = \begin{Bmatrix} 0 \\ 0 \end{Bmatrix} \tag{18}$$

Then, terms in Eq. (17), which are related to ground motion are moved to the right hand side, we obtain

$$\begin{aligned} &\begin{bmatrix} M_{ss} & M_{sg} \\ M_{sg}^T & M_{gg} \end{bmatrix} \begin{Bmatrix} \ddot{\vec{U}}_s(t) \\ 0 \end{Bmatrix} + \begin{bmatrix} C_{ss} & C_{sg} \\ C_{sg}^T & C_{gg} \end{bmatrix} \begin{Bmatrix} \dot{\vec{U}}_s(t) \\ 0 \end{Bmatrix} + \begin{bmatrix} K_{ss} & K_{sg} \\ K_{sg}^T & K_{gg} \end{bmatrix} \begin{Bmatrix} \vec{U}_s(t) \\ 0 \end{Bmatrix} \\ &\qquad = \begin{Bmatrix} \vec{R}(t) \\ 0 \end{Bmatrix} - \begin{bmatrix} M_{ss} & M_{sg} \\ M_{sg}^T & M_{gg} \end{bmatrix} \begin{Bmatrix} \ddot{\vec{U}}_g(t) \\ \ddot{\vec{U}}_g(t) \end{Bmatrix} - \begin{bmatrix} C_{ss} & C_{sg} \\ C_{sg}^T & C_{gg} \end{bmatrix} \begin{Bmatrix} \dot{\vec{U}}_g(t) \\ \dot{\vec{U}}_g(t) \end{Bmatrix} \end{aligned} \tag{19}$$

Then, we return to the first of the two partitioned equations, i.e.

$$\begin{aligned} &\underline{\underline{M}}_{ss}\ddot{\vec{U}}_s(t) + \underline{\underline{C}}_{ss}\dot{\vec{U}}_s(t) + \underline{\underline{K}}_{ss}\vec{U}_s(t) \\ &\qquad = \vec{R}(t) - \underline{\underline{M}}_{ss}\ddot{\vec{U}}_g(t) - \underline{\underline{M}}_{sg}\ddot{\vec{U}}_g(t) - \underline{\underline{C}}_{ss}\dot{\vec{U}}_g(t) - \underline{\underline{C}}_{sg}\dot{\vec{U}}_g(t) \\ &\qquad = \vec{R}(t) + \vec{R}_{eff}(t) \end{aligned} \tag{20}$$

where the vector of effective seismic forces $\vec{R}_{eff}(t)$ is stated as

$$\vec{R}_{eff}(t) = -\underline{\underline{M}}_{ss}\ddot{\vec{U}}_g(t) - \underline{\underline{M}}_{sg}\ddot{\vec{U}}_g(t) - \underline{\underline{C}}_{ss}\dot{\vec{U}}_g(t) - \underline{\underline{C}}_{sg}\dot{\vec{U}}_g(t) \tag{21}$$

For many practical applications, simplification of the effective force vector is possible on two parts. First, the damping term in Eq. (21) is zero if the damping matrices are proportional to the stiffness matrices (i.e., $C_{ss} = \beta K_{ss}$ and $C_{sg} = \beta K_{sg}$) because of Eq. (18). While the damping term in Eq. (21) is not zero for arbitrary forms of damping, it is usually small relative to the inertia term and may therefore be dropped. Second, for structures with mass idealized as lumped at the DOFs, the mass matrix is diagonal, implying that M_{sg} is a null matrix and M_{ss} is diagonal (Chopra, 1995). With these simplification, Eq. (21) reduced to

$$\vec{R}_{eff}(t) = -\underline{\underline{M}}_{ss}\ddot{\vec{U}}_g(t) \tag{22}$$

Then we obtain the equation of motion of SFT for seismic excitation loading, i.e.

$$\underline{\underline{M}}_{ss}\ddot{\vec{U}}_s(t) + \underline{\underline{C}}_{ss}\dot{\vec{U}}_s(t) + \underline{\underline{K}}_{ss}\vec{U}_s(t) = \vec{R}(t) - \underline{\underline{M}}_{ss}\ddot{\vec{U}}_g(t) \tag{23}$$

2.4 Equation of motion for fluid-structure interaction of submerged floating tunnel

From section 2.2 and 2.3, we has been described hydrodynamic force caused by fluid-structure interaction and equation of motion for identical support excitation loading, respectively. Then, we will bring the hydrodynamic force acting on SFT to the equation of motion without considering the fluid-structure interaction.

Rewrite the Eq. (23) as

$$\underline{\underline{M}}_{ss}\ddot{\vec{U}}_s(t)+\underline{\underline{C}}_{ss}\dot{\vec{U}}_s(t)+\underline{\underline{K}}_{ss}\vec{U}_s(t)=\vec{R}(t)-\underline{\underline{M}}_{ss}\ddot{\vec{U}}_g(t) \tag{24}$$

To consider the fluid-structure interaction between external fluid and SFT, $\vec{R}(t)$ will be changed as four types of hydrodynamic force which was stated in section 2.2, i.e.

$$\underline{\underline{M}}_{ss}\ddot{\vec{U}}_s(t)+\underline{\underline{C}}_{ss}\dot{\vec{U}}_s(t)+\underline{\underline{K}}_{ss}\vec{U}_s(t)=\vec{R}_1(t)+\vec{R}_2(t)+\vec{R}_3(t)+\vec{R}_4(t)-\underline{\underline{M}}_{ss}\ddot{\vec{U}}_g(t) \tag{25}$$

Next, we can demonstrate $\vec{R}(t)$ from Eq. (15).

$$\begin{aligned}&\underline{\underline{M}}_{ss}\ddot{\vec{U}}_s(t)+\underline{\underline{C}}_{ss}\dot{\vec{U}}_s(t)+\underline{\underline{K}}_{ss}\vec{U}_s(t)\\&=-\underline{\underline{M}}_{added}\ddot{\vec{U}}_s(t)-\underline{\underline{M}}_{added}\ddot{\vec{U}}_g(t)-\underline{\underline{C}}_w(t)\dot{\vec{U}}_s(t)-\vec{R}_{drag}(t)-\underline{\underline{M}}_{ss}\ddot{\vec{U}}_g(t)\end{aligned} \tag{26}$$

From section 2.3, we assume identical support seismic excitation, Rayleigh structure damping $\underline{\underline{C}}_{ss}$ and lumped structure mass matrix $\underline{\underline{M}}_{ss}$ to simplify the effective force vector, and now we also consider the hydrodynamic force by lumped approach. So, added mass effect becomes a form of lumped mass matrix which has only diagonal component, translation DOFs in cross-sectional axes (i.e. y and z axis).

$$\underline{\underline{M}}_{added,tt} = m_a \cdot \frac{l_e}{2} \tag{27}$$

In which subscript tt indicates diagonal components of cross-sectional translation DOFs. The mass per unit length of displaced water by the tunnel and length of beam element for the tunnel is denoted by m_a and l_e, respectively.

Added damping matrix and drag loading vector has sign function and ground velocity. These terms make the time integration complicated, so we applied lumped approach to consider effectively, they also has component only at y and z translation DOF, i.e.

$$\begin{aligned} \underline{\underline{C}}_{w,yy}(t) &= sign\{\dot{U}_g^y(t) + \dot{U}^y(t)\} \cdot 2c_w \dot{U}_g^y(t) \cdot \frac{l_e}{2} \\ \underline{\underline{C}}_{w,zz}(t) &= sign\{\dot{U}_g^z(t) + \dot{U}^z(t)\} \cdot 2c_w \dot{U}_g^z(t) \cdot \frac{l_e}{2} \end{aligned} \tag{28}$$

$$\begin{aligned} \vec{R}_{drag,y}(t) &= -sign\{\dot{U}_g^y(t) + \dot{U}^y(t)\} \cdot c_w \{\dot{U}_g^y(t)\}^2 \cdot \frac{l_e}{2} \\ \vec{R}_{drag,z}(t) &= -sign\{\dot{U}_g^z(t) + \dot{U}^z(t)\} \cdot c_w \{\dot{U}_g^z(t)\}^2 \cdot \frac{l_e}{2} \end{aligned} \tag{29}$$

Finally, we can describe the final form of equation of motion for SFT, i.e.

$$[\underline{\underline{M}}_{ss} + \underline{\underline{M}}_{added}]\ddot{\vec{U}}_s(t) + [\underline{\underline{C}}_{ss} + \underline{\underline{C}}_w(t)]\dot{\vec{U}}_s(t) + \underline{\underline{K}}_{ss}\vec{U}_s(t) = -[\underline{\underline{M}}_{ss} + \underline{\underline{M}}_{added}]\ddot{\vec{U}}_g(t) - \vec{R}_{drag}(t) \tag{30}$$

Chapter 3. Numerical methods

In this chapter, we describe numerical methods for solving the equation of motion for fluid-structure interaction of SFT under seismic excitation. We applied the finite element method (FEM) for modeling the structural system of SFT. As an input ground motion, we employed the actual time history of seismic accelerations and velocities of some representative real earthquakes. And, Newmark method is employed to find the solution in time domain, which is one of typical dynamic-implicit solution method.

3.1 Continuum mechanics based beam element

For the tunnel structure of SFT system, continuum mechanics based 3-dimensional beam element is selected. It was developed as a general and efficient 3-D beam finite element with cross-sectional discretizations that allows for warping displacements and study the twisting behavior of the beam element under various modeling conditions (Yoon et al., 2012).

The novel features of the proposed beam element that originate from the inherent generality of the continuum mechanics based approach are as follows:

- The formulation is simple and straightforward.
- The formulation can handle all complicated 3-D geometries including curved geometries, varying cross-sections, and arbitrary cross-sectional shapes (including thin/thick-walled and open/closed cross-sections).
- Warping effects fully coupled with bending, shearing, and stretching are automatically included.
- Seven degrees of freedom (only one additional degree of freedom for warping) are used at each beam node to ensure inter-elemental continuity of warping displacements.
- The pre-calculation of cross-sectional properties (area, second moment of area, etc.) is not required because the beam formulation is based on continuum mechanics.
- Analyses of short, long, and deep beams are available, and eccentricities of

loadings and displacements on beam cross-sections are naturally considered.

- The basic formulation can be easily extended to general nonlinear analyses that considered geometrical and material nonlinearities.

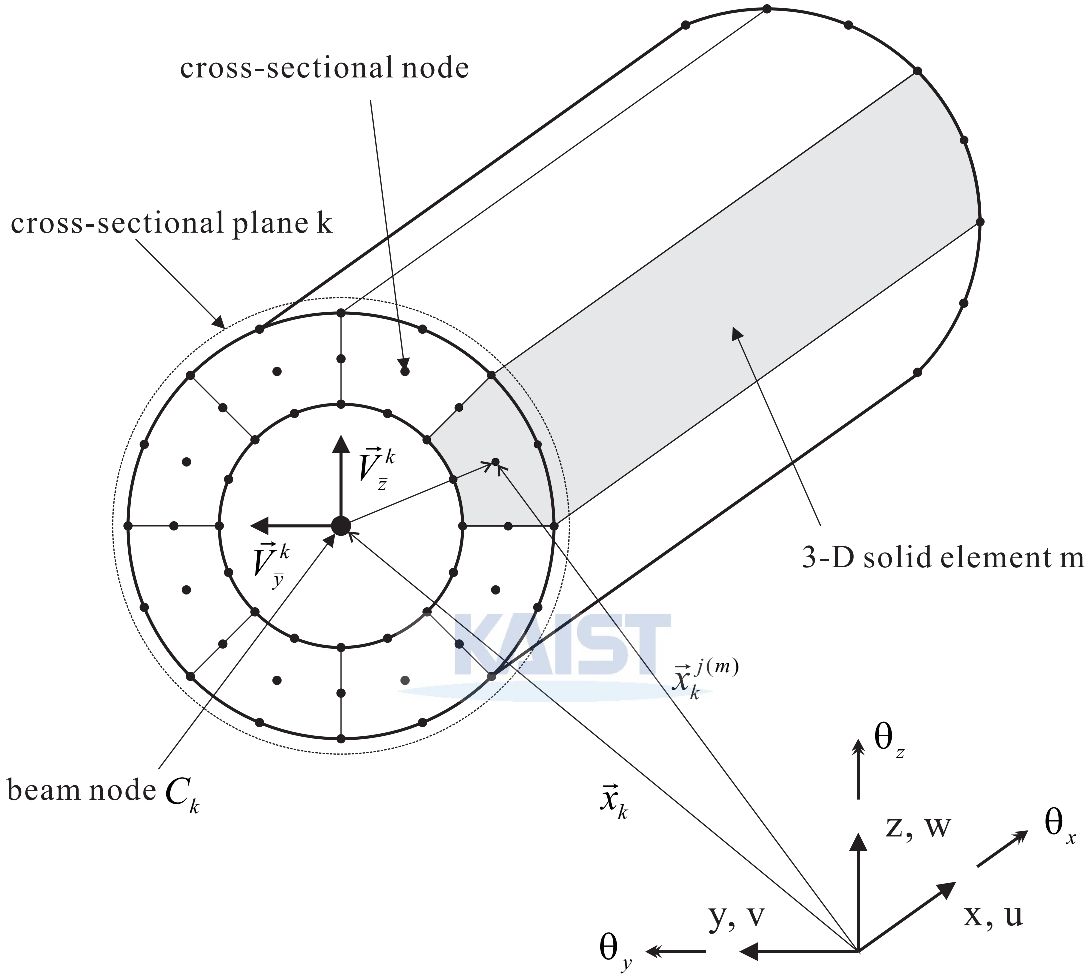

Fig. 4. Continuum mechanics based beam finite element with sectional discretization for SFT

3.1.1 Interpolation of geometry

The beam formulation is derived from the assemblage of solid finite elements. An arbitrary geometry of a beam for the tunnel can be modeled by 3-dimensional solid finite elements aligned in the beam length direction as shown in Fig. 4. Here, all the nodes of the solid elements are positioned on several cross-sectional planes of the beams. The geometry interpolation of the l-node solid element m is given by

$$\vec{x}^{(m)} = \sum_{i=1}^{l} h_i(r,s,t)\vec{x}_i^{(m)} \tag{31}$$

where $\vec{x}^{(m)}$ is the material position vector of the solid element m in the global Cartesian coordinate system, $h_i(r,s,t)$ are the 3-D interpolation polynomials for the usual isoparametric procedure (that is, shape functions) and $\vec{x}_i^{(m)}$ is the i th nodal position vector of the solid element m.

Since the nodes of the solid element are placed on the cross-sectional planes, the 3-D interpolation in Eq. (31) can be replaced by the multiplication of 1-D and 2-D shape functions,

$$\vec{x}^{(m)} = \sum_{k=1}^{q} h_k(r)\sum_{j=1}^{p} h_j(s,t)\vec{x}_k^{j(m)} \tag{32}$$

in which q is the number of the cross-sectional planes, p is the number of the nodes of the solid element m positioned at each cross-sectional plane (for example, q =2 and p =9, $l = p \times q = 18$ for the 18-node solid element m shaded in Fig. 4), $h_k(r)$ and $h_j(s,t)$ are the 1-D and 2-D interpolation polynomials for the usual isoparametric procedure, respectively, and $\vec{x}_k^{j(m)}$ are the j th nodal position vector of the solid element m on cross-sectional plane k, see Fig. 4. Here, we call $\vec{x}_k^{j(m)}$ the position vector of the j th cross-sectional node on cross-sectional plane k corresponding to the solid element m. In general, the order of the 2-D interpolation function does not need to be the same as the order of the 1-D interpolation function.

The kinematic assumption of the Timoshenko beam theory can be enforced at all the cross-sectional nodes (Živkovic et al. 2001), that is, plane cross-sections originally normal to the mid-line of the beam are not necessarily normal to the mid-line of the deformed beam (Timoshenko, 1970).

$$\vec{x}_k^{j(m)} = \vec{x}_k + \bar{y}_k^{j(m)} \vec{V}_{\bar{y}}^k + \bar{z}_k^{j(m)} \vec{V}_{\bar{z}}^k \tag{33}$$

where the unit vectors $\vec{V}_{\bar{y}}^k$ and $\vec{V}_{\bar{z}}^k$ are the director vectors placed on cross-sectional plane k, the two vectors and the position $\vec{x}_k$ of origin at point C_k define the cross-sectional Cartesian coordinate system, $\bar{y}_k^{j(m)}$ and $\bar{z}_k^{j(m)}$ represent the material position of the jth cross-sectional node of the solid element m in the cross-sectional Cartesian coordinate system on cross-sectional plane k. Note that $\vec{V}_{\bar{y}}^k$ and $\vec{V}_{\bar{z}}^k$ are normal to each other and determine the direction of cross-sectional plane k. The vector relation in Eq. (33) is graphically represented in Fig. 4.

The use of Eq. (33) in (32) results in the geometry interpolation of the q-node continuum mechanics based beam finite element corresponding to the solid element m.

$$\vec{x}^{(m)} = \sum_{k=1}^{q} h_k(r)\vec{x}_k + \sum_{k=1}^{q} h_k(r)\bar{y}_k^{(m)}\vec{V}_{\bar{y}}^k + \sum_{k=1}^{q} h_k(r)\bar{z}_k^{(m)}\vec{V}_{\bar{z}}^k \tag{34}$$

with $$\bar{y}_k^{(m)} = \sum_{j=1}^{p} h_j(s,t)\bar{y}_k^{j(m)}, \quad \bar{z}_k^{(m)} = \sum_{j=1}^{p} h_j(s,t)\bar{z}_k^{j(m)} \tag{35}$$

where $\bar{y}_k^{(m)}$ and $\bar{z}_k^{(m)}$ denote the material position of the solid element m in the cross-sectional Cartesian coordinate system on cross-sectional plane k. Eq. (35) indicates that the material position on the cross-sectional plane is interpolated by cross-sectional nodes. It is important to know that Eq. (34) is the geometry interpolation of the solid element m aligned in the beam length direction in which the kinematic assumption of the Timoshenko beam theory is enforced.

Then, the point C_k corresponds to the kth beam node. The beam node at point C_k can be arbitrarily positioned on cross-sectional plane k defined by the two director vectors and in Fig. 4. The longitudinal reference line that is used to define the geometry of the beam is created by connecting the beam nodes.

As mentioned, the geometry interpolation of the beam element in Eq. (34) corresponds to the solid element m. The simple assemblage of the interpolation functions corresponding to all the solid elements aligned along the beam length direction represents the geometry interpolation of the whole beam element. The size and shape of the cross-sections can arbitrarily vary but the cross-sectional mesh pattern should be the same to maintain the continuity of the geometry on all the cross-sectional planes.

3.1.2 Interpolation of displacements

From the interpolation of geometry in Eq. (34), the interpolation of displacements corresponding to the solid element m is derived as in (Bathe, 1996)

$$\vec{u}^{(m)} = \sum_{k=1}^{q} h_k(r)\vec{u}_k + \sum_{k=1}^{q} h_k(r)\bar{y}_k^{(m)}\{\vec{\theta}_k \times \vec{V}_{\bar{y}}^k\} + \sum_{k=1}^{q} h_k(r)\bar{z}_k^{(m)}\{\vec{\theta}_k \times \vec{V}_{\bar{z}}^k\} \tag{36}$$

in which $\vec{u}_k$ and $\vec{\theta}_k$ are the displacement and rotation vectors, respectively, in the global Cartesian coordinate system at beam node k

$$\vec{u}_k = \begin{Bmatrix} u^k \\ v^k \\ w^k \end{Bmatrix} \quad \text{and} \quad \vec{\theta}_k = \begin{Bmatrix} \theta_x^k \\ \theta_y^k \\ \theta_z^k \end{Bmatrix} \tag{37}$$

Eq. (36) indicates that the displacement fields of all the solid elements that compose the whole beam is determined by the three translations and three rotations (six degrees of freedom) at each beam node because the nodes of the solid elements are placed on the cross-sectional planes and the kinematic assumption of the Timoshenko beam theory is enforced. Therefore, the assemblage of the solid elements can act like a single beam element and the beam element can have the cross-sectional discretization.

3.2 Cable element

The tension leg cables which are anchored to the seabed to balance the net buoyancy. Tension leg cables are assumed always in tension, so it maintain a straight line. So, for these cables, we can select 2-node truss element. Two truss elements are installed at both sides of each supporting point, normal to the longitudinal axis of tunnel, see Fig. 5.

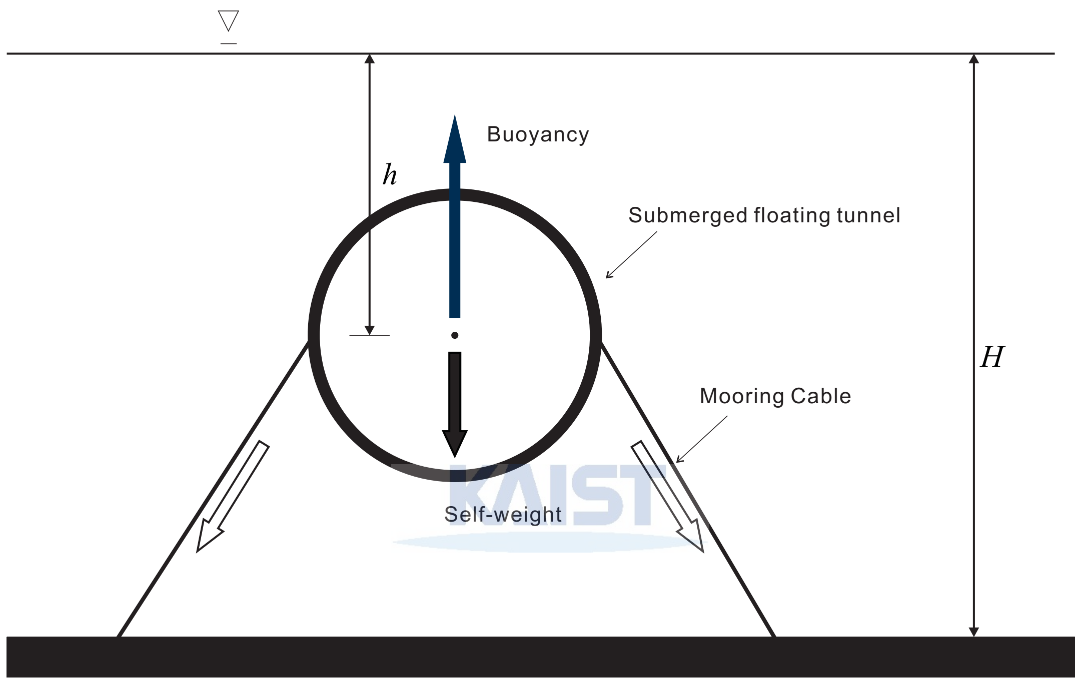

Fig. 5. Tension leg cable system of SFT in hydrostatic condition

In this study, we only consider the SFT type with buoyancy-weight ratio(BWR) larger than unity, the tunnel buoyancy is larger than tunnel self-weight and the net buoyancy is balanced by cable systems which are assembled between tunnel and seabed (Long et al., 2009). Hence, initial tension of tension leg cables by net buoyancy is added by the type of axial stiffness in structural stiffness. For tension leg cable system, we consider mass and stiffness to the beam node for tunnel which is connected by cable element, see Fig. 6.

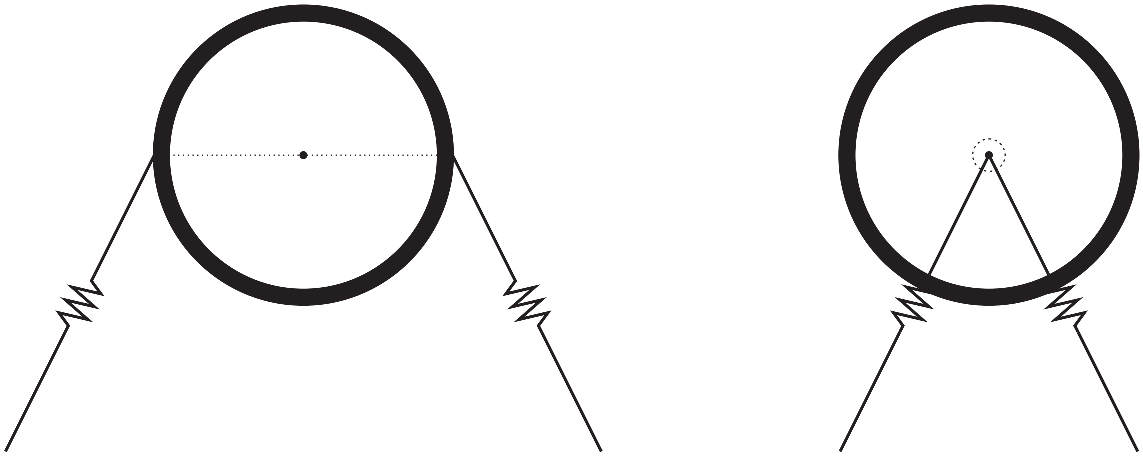

Fig. 6. Modeling of tension leg cable as the truss element

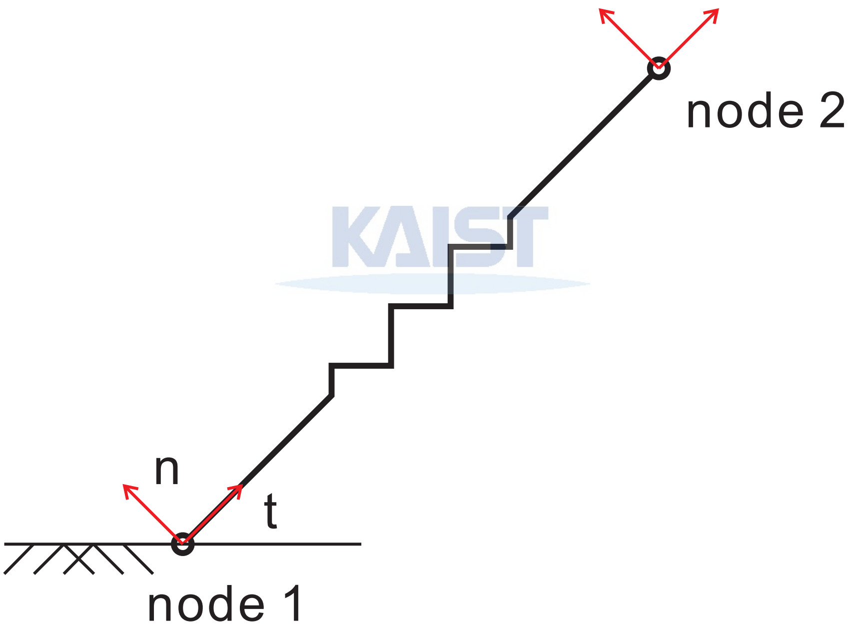

Fig. 7. Truss element for tension leg cable on the left side of tunnel

$$\underline{\underline{K}}_{cable}\vec{U} = \underline{\underline{K}}_{T}\vec{U} + \underline{\underline{K}}_{s}\vec{U} = \frac{T_0}{l}\begin{bmatrix} 1 & -1 \\ -1 & 1 \end{bmatrix}\begin{bmatrix} U_1^t \\ U_2^t \end{bmatrix} + \frac{EA}{l}\begin{bmatrix} 1 & -1 \\ -1 & 1 \end{bmatrix}\begin{bmatrix} U_1^t \\ U_2^t \end{bmatrix} \tag{38}$$

$$\underline{\underline{M}}_{cable}\ddot{\vec{U}} = \frac{\rho A l}{6}\begin{bmatrix} 2 & 1 \\ 1 & 2 \end{bmatrix}\begin{bmatrix} \ddot{U}_1^t \\ \ddot{U}_2^t \end{bmatrix} \tag{39}$$

In Eqs. (38)-(39), K_{cable} and M_{cable} are stiffness and mass matrix of tension leg cable, respectively. T_0 is tensile force acting on cables by net buoyancy. Length, elastic modulus and cross-sectional area of cable are denoted by l, E and A, respectively. C is material law matrix and ρ is density of cable material.

To assemble the stiffness and mass matrix of cables about local coordinates to the global structure matrices of total SFT system, we consider coordinate transformation about rotation on the longitudinal axis of global coordinate and extend six degree of freedom for each node. Furthermore, cable mass is also idealized as lumped at both nodes.

3.3 Rayleigh structure damping

In this study, Rayleigh damping which proportional to the mass and stiffness is used for generating damping matrix for the SFT. Rayleigh damping is expressed as

$$\underline{\underline{C}} = \alpha \underline{\underline{M}} + \beta \underline{\underline{K}} \tag{40}$$

where α and β are the coefficient of Rayleigh damping and through the coefficient, we can judge the importance of mass or stiffness for the structure damping system. To calculate the coefficient of Rayleigh damping, we need to conduct frequency analysis to obtain first two mode of SFT-fluid system. The Rayleigh damping coefficient is calculated by following equation (Lee, 2012)

$$\alpha = \frac{2\omega_1\omega_2}{\omega_1 + \omega_2}\xi \quad \text{and} \quad \beta = \frac{2}{\omega_1 + \omega_2}\xi \tag{41}$$

The critical damping ratio of structure is represented by ξ. In this study, the damping ratio for SFT is taken as 5%.

3.4 Input seismic accelerations and velocities

For the seismic analysis of SFT which has hydroelastic behavior, three ground motions are selected. There are two real earthquakes and one harmonic ground motion is selected for the input seismic velocity and acceleration. The characteristics of applied ground motion are indicated as Table. 1 and the time history of velocity and acceleration are illustrated as Figs. 8-9.

Table. 1. Characteristics of selected ground motion

Earthquakes	PGA (g)	Range of dominant frequencies (Hz)
harmonic	0.3	0.25
El Centro – Imperial Valley	0.313	0.83-2.30
Kobe – Japan	0.599	0.97-2.50

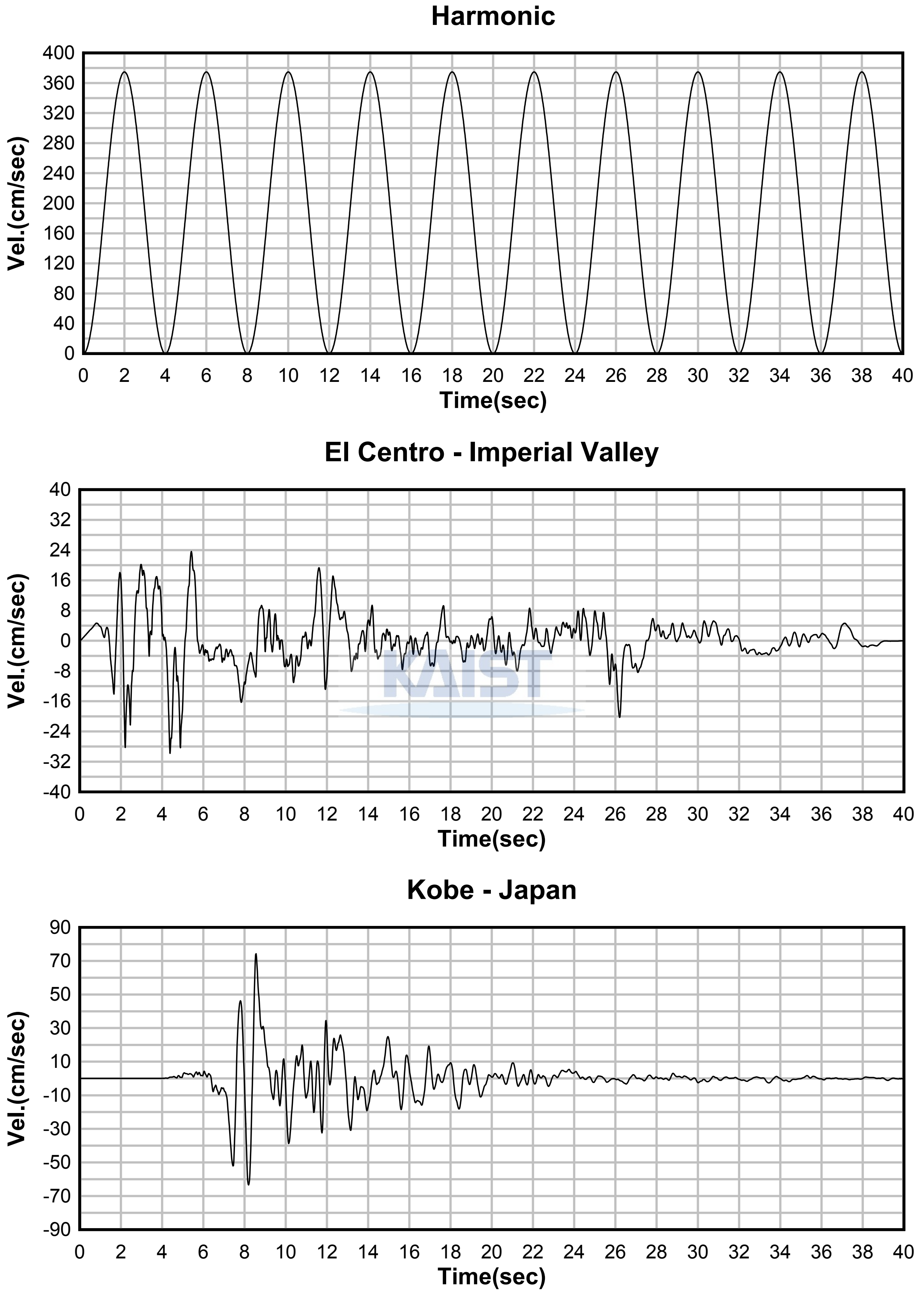

Fig. 8. Selected ground velocity time history : duration time 40 sec

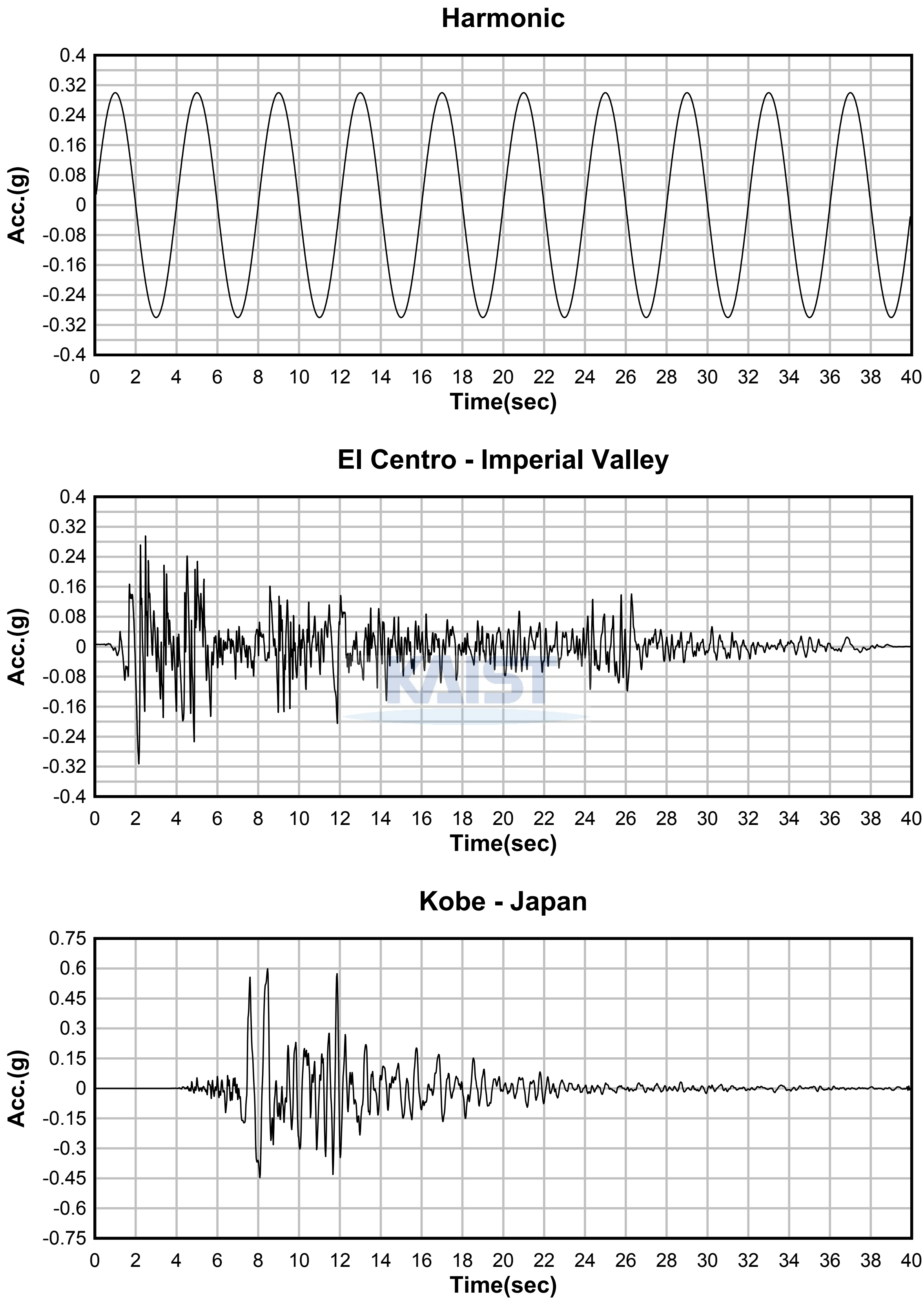

Fig. 9. Selected ground acceleration time history : duration time 40 sec

3.5 Time integration method

To solve the equation of motion of SFT in time domain, direct integration method is used. In direct integration the equation of motion is integrated using a numerical step-by-step procedure, the term "direct" meaning that prior to the numerical integration, no transformation of the equations into a different form is carried out (Bathe, 1996).

In this study, we use the Newmark method, which is a one-step implicit scheme for solving the dynamic transient problem. Because implicit schemes are unconditionally stable, we can obtain accuracy in the integration, the time step Δt can be selected without a requirement such as critical values, it can be larger than that of explicit schemes.

To use the Newmark method, the following assumptions are used

$$ {}^{t+\Delta t}\dot{\vec{U}} = {}^{t}\dot{\vec{U}} + \Delta t[(1-\delta)\,{}^{t}\ddot{\vec{U}} + \delta\,{}^{t+\Delta t}\ddot{\vec{U}}] \tag{42} $$

$$ {}^{t+\Delta t}\vec{U} = {}^{t}\vec{U} + \Delta t\,{}^{t}\dot{\vec{U}} + (\Delta t)^2[(\frac{1}{2}-\alpha)\,{}^{t}\ddot{\vec{U}} + \alpha\,{}^{t+\Delta t}\ddot{\vec{U}}] \tag{43} $$

where α and δ are parameters that can be determined to obtain integration accuracy and stability. We employed the constant average acceleration method (also called trapezoidal rule), in which case $\delta = \frac{1}{2}$ and $\alpha = \frac{1}{4}$.

In addition to Eqs. (42)-(43), for solution of the displacements, velocities, and accelerations at time $t+\Delta t$, the equilibrium equation at time $t+\Delta t$ are also considered

$$ \underline{\underline{M}}\,{}^{t+\Delta t}\ddot{\vec{U}} + \underline{\underline{C}}\,{}^{t+\Delta t}\dot{\vec{U}} + \underline{\underline{K}}\,{}^{t+\Delta t}\vec{U} = {}^{t+\Delta t}\vec{R} \tag{44} $$

Solving from Eq. (43) for ${}^{t+\Delta t}\ddot{\vec{U}}$ in terms of ${}^{t+\Delta t}\vec{U}$ and then substituting for ${}^{t+\Delta t}\ddot{\vec{U}}$ into Eq. (42), we obtain equations for ${}^{t+\Delta t}\ddot{\vec{U}}$ and ${}^{t+\Delta t}\dot{\vec{U}}$, each in terms of the unknown displacements ${}^{t+\Delta t}\vec{U}$ only. These two relations for ${}^{t+\Delta t}\ddot{\vec{U}}$ and ${}^{t+\Delta t}\dot{\vec{U}}$ are substitutes into Eq. (44) to solve for ${}^{t+\Delta t}\vec{U}$, after which, using Eqs. (42)-(43), ${}^{t+\Delta t}\ddot{\vec{U}}$ and ${}^{t+\Delta t}\dot{\vec{U}}$ can also be calculated. This algorithm to solve for ${}^{t+\Delta t}\vec{U}$ can be expressed by the forms of effective stiffness matrix and load vector, denoted by $\hat{\underline{\underline{K}}}$ and ${}^{t+\Delta t}\hat{\vec{R}}$, respectively.

$$\hat{\underline{\underline{K}}}\;{}^{t+\Delta t}\vec{U} = {}^{t+\Delta t}\hat{\vec{R}} \tag{45}$$

with

$$\hat{\underline{\underline{K}}} = \underline{\underline{K}} + \frac{1}{\alpha(\Delta t)^2}\underline{\underline{M}} + \frac{\delta}{2\Delta t}\underline{\underline{C}} \tag{46}$$

$$\begin{aligned} {}^{t+\Delta t}\hat{\vec{R}} = {}^{t+\Delta t}\vec{R} &+ \underline{\underline{M}}\left(\frac{1}{\alpha(\Delta t)^2}\,{}^{t}\vec{U} + \frac{1}{\alpha\Delta t}\,{}^{t}\dot{\vec{U}} + \frac{1-2\alpha}{2\alpha}\,{}^{t}\ddot{\vec{U}}\right) \\ &+ \underline{\underline{C}}\left(\frac{\delta}{\alpha\Delta t}\,{}^{t}\vec{U} + \frac{\delta-\alpha}{\alpha}\,{}^{t}\dot{\vec{U}} + \frac{\Delta t}{2}\left(\frac{\delta}{\alpha}-2\right){}^{t}\ddot{\vec{U}}\right) \end{aligned} \tag{47}$$

Now, we employ these complete algorithm of the Newmark time integration method to the equation of motion for SFT fluid-structure interaction model with seismic excitation, Eq. (30) i.e.

$$[\underline{\underline{M}}_{ss} + \underline{\underline{M}}_{added}]\;{}^{t+\Delta t}\ddot{\vec{U}} + [\underline{\underline{C}}_{ss} + {}^{t+\Delta t}\underline{\underline{C}}_{w}]\;{}^{t+\Delta t}\dot{\vec{U}} + \underline{\underline{K}}_{ss}\;{}^{t+\Delta t}\vec{U} = {}^{t+\Delta t}\vec{R} \tag{48}$$

where external load vector ${}^{t+\Delta t}\vec{R}$ can be expressed

$$[\underline{\underline{M}}_{ss} + \underline{\underline{M}}_{added}]\,{}^{t+\Delta t}\ddot{\vec{U}} + [\underline{\underline{C}}_{ss} + {}^{t+\Delta t}\underline{\underline{C}}_{w}]\,{}^{t+\Delta t}\dot{\vec{U}} + \underline{\underline{K}}_{ss}\,{}^{t+\Delta t}\vec{U} = -[\underline{\underline{M}}_{ss} + \underline{\underline{M}}_{added}]\,{}^{t+\Delta t}\ddot{\vec{U}}_{g} - {}^{t+\Delta t}\vec{R}_{drag} \tag{49}$$

with lumped added damping matrix and drag loading from Eqs. (28)-(29), i.e.

$$
\begin{aligned}
{}^{t+\Delta t}\underline{\underline{C}}_{w,yy}(t) &= sign\{{}^{t}\dot{U}_g^y(t)+{}^{t}\dot{U}^y(t)\}\cdot 2c_w\,{}^{t+\Delta t}\dot{U}_g^y(t)\cdot\frac{l_e}{2} \\
{}^{t+\Delta t}\underline{\underline{C}}_{w,zz}(t) &= sign\{{}^{t}\dot{U}_g^z(t)+{}^{t}\dot{U}^z(t)\}\cdot 2c_w\,{}^{t+\Delta t}\dot{U}_g^z(t)\cdot\frac{l_e}{2}
\end{aligned} \tag{50}
$$

$$
\begin{aligned}
{}^{t+\Delta t}\vec{R}_{drag,y}(t) &= -sign\{{}^{t}\dot{U}_g^y(t)+{}^{t}\dot{U}^y(t)\}\cdot c_w\{{}^{t+\Delta t}\dot{U}_g^y(t)\}^2\cdot\frac{l_e}{2} \\
{}^{t+\Delta t}\vec{R}_{drag,z}(t) &= -sign\{{}^{t}\dot{U}_g^z(t)+{}^{t}\dot{U}^z(t)\}\cdot c_w\{{}^{t+\Delta t}\dot{U}_g^z(t)\}^2\cdot\frac{l_e}{2}
\end{aligned} \tag{51}
$$

For the sign function in Eqs. (50)-(51), we consider the calculated translational degree of freedoms in current time step, which are orthogonal components to the tunnel longitudinal axis. Then, Eqs. (45)-(47) are changed

$$
\hat{\underline{\underline{K}}}\,{}^{t+\Delta t}\vec{U} = {}^{t+\Delta t}\hat{\vec{R}} \tag{52}
$$

$$
\hat{\underline{\underline{K}}} = \underline{\underline{K}}_{ss} + \frac{1}{\alpha(\Delta t)^2}[\underline{\underline{M}}_{ss} + \underline{\underline{M}}_{added}] + \frac{\delta}{2\Delta t}[\underline{\underline{C}}_{ss} + {}^{t+\Delta t}\underline{\underline{C}}_{w}] \tag{53}
$$

$$
\begin{aligned}
{}^{t+\Delta t}\hat{\vec{R}} &= -[\underline{\underline{M}}_{ss} + \underline{\underline{M}}_{added}]\,{}^{t+\Delta t}\ddot{\vec{U}}_g + {}^{t+\Delta t}\vec{R}_{drag} \\
&\quad + [\underline{\underline{M}}_{ss} + \underline{\underline{M}}_{added}]\left(\frac{1}{\alpha(\Delta t)^2}\,{}^{t}\vec{U} + \frac{1}{\alpha\Delta t}\,{}^{t}\dot{\vec{U}} + \frac{1-2\alpha}{2\alpha}\,{}^{t}\ddot{\vec{U}}\right) \\
&\quad + [\underline{\underline{C}}_{ss} + {}^{t+\Delta t}\underline{\underline{C}}_{w}]\left(\frac{\delta}{\alpha\Delta t}\,{}^{t}\vec{U} + \frac{\delta-\alpha}{\alpha}\,{}^{t}\dot{\vec{U}} + \frac{\Delta t}{2}\left(\frac{\delta}{\alpha}-2\right){}^{t}\ddot{\vec{U}}\right)
\end{aligned} \tag{54}
$$

By solving Eq. (52) from Eqs. (53)-(54), ${}^{t+\Delta t}\vec{U}$ can be calculated. Then, using Eqs. (42)-(43), we can also calculate ${}^{t+\Delta t}\ddot{\vec{U}}$ and ${}^{t+\Delta t}\dot{\vec{U}}$.

Chapter 4. Numerical results and discussion

In this chapter, we establish the imaginary model of SFT as an example and conduct numerical analysis to solve the fluid-structure interaction of SFT under seismic excitation. First, we define the characteristics of structures and external fluid. Next, we verify the SFT numerical model by comparing with commercial structure numerical analysis software, ADINA. Then, we study the maximum response distributions of displacement, velocity, and acceleration through the SFT length and calculate the time history of SFT responses at two locations for each ground motion and seismic excitation angle. Finally, we calculate the maximum responses of bending moment for harmonic excitation.

4.1 Characteristics of SFT model for application

The finite element model of SFT for dynamic analysis is illustrated on Fig. 10 below. The tunnel has same cross-section for all structure and straight line which is parallel to the flat bottom seabed and its longitudinal axis is also parallel to the x axis. The one segment of tunnel has 100m length and it discretized by four continuum mechanics based 3-D beam element. The tension leg cables are modeled by two-node truss element. Two truss elements are installed at both sides of each supporting point and inclined with angle ϕ between seabed, normal to the longitudinal axis of tunnel. The ratio of buoyancy and self-weight of tunnel (BWR) is about 1.25, cables assumed always maintain a straight line. The all structures are assumed to be a homogeneous, isotropic, and linear elastic material with small displacement and strain.

Flat bottom seabed is regarded as a frictionless rigid foundation and seismic motion is excited only parallel direction (i.e. directions of x and y axis). Therefore, it cannot make water flow when parallel seismic motion in still water. We conduct four cases of seismic excitation angle from the angle of parallel (named as longitudinal excitation) to normal (named as horizontal excitation) to the tunnel longitudinal axis (i.e. 0, 30, 60 and 90 deg.).

To use Morison equation, we determine inertial and drag coefficient. International codes or guidelines for the design of offshore structures recommend values of the drag and inertial coefficient ranging from 0.6 and 1.2, respectively, (smooth members) to 1.2 and 2.0 (rough members) for steady flows (Martire, 2000). So, we determine inertial and drag coefficient 2.0 and 1.0, respectively.

Characteristics of SFT model for application are arranged by Table. 2 below.

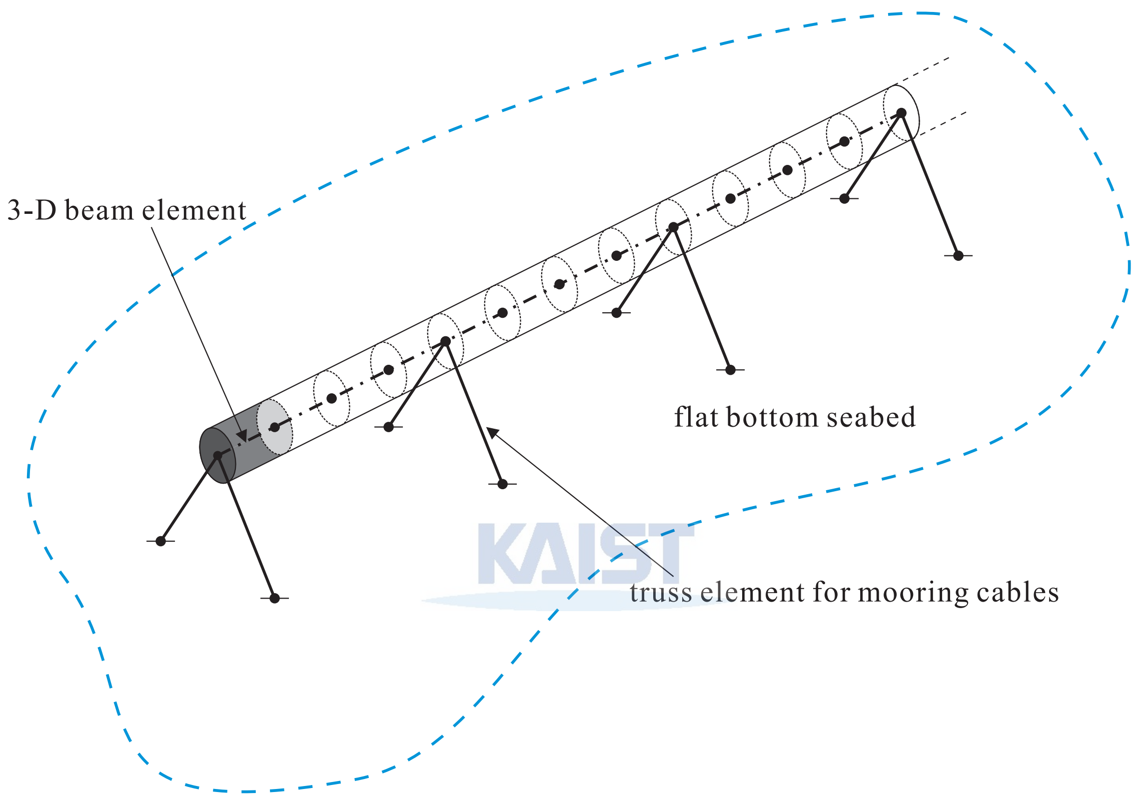

Fig. 10. SFT finite element model for application

Table. 2. Characteristics of SFT model for application

Structure				Fluid	
Tunnel length (L)	10km	Cable diameter (D_{cable})	0.120m	Waver depth (H)	120m
Element length (L_e)	25m	Cable density (ρ_{cable})	7850kg/m^3	Depth to the tunnel (h)	40m
Cable length (L_{cable})	92.4m	Tunnel density (ρ)	2400kg/m^3	Gravity acceleration (g)	9.81m/sec^2
Cable angle (ϕ)	60deg.	Cable elastic modulus (E_{cable})	200GPa	Water density (ρ_{water})	1025kg/m^3
Tunnel outer diameter (D)	16m	Tunnel elastic modulus (E)	31GPa	Inertial coefficient ($C_I = 1 + C_A$)	2.0
Tunnel inner diameter (D_{in})	13m	Spacing between supporting points	100m	Drag coefficient (C_D)	1.0
Seismic excitation angle (θ)	0~90 deg.	Poisson's ratio (ν)	0	BWR	1.25
Rayleigh damping ratio (ξ)	5%				

4.2 Verification

In this section, we compare the results from developed numerical analysis of SFT with commercial structure numerical analysis software, ADINA. For this, we organize the same SFT finite model in both ADINA and developed program, conduct seismic analysis for harmonic excitation as an example. ADINA modeling of one segment SFT is illustrated on Fig. 11 below.

From Fig. 11, we modeled one segment of SFT with ten 3-D beam elements, one segment means tunnel between the two nearby supporting point with tension leg cables. Harmonic ground motion is excited in horizontal direction (i.e. $\theta = 90\,\text{deg.}$). For the displacement boundary condition, all DOFs of supports on the seabed are fixed, longitudinal translation and rotation DOFs at tunnel ends are fixed. The response horizontal displacement time history at SFT midpoint of both systems are representatively expressed on Fig. 12 below.

The results are almost same at all locations of tunnel. But in verification, we cannot consider the hydrodynamic forces from fluid-structure interaction. Because there are no sufficient experimental data for the similar structure system or commercial software, which can conduct fluid-structure interaction when the structure are moving in fluid and seismic motion also excited at the same time. Now it has continuously studied for verification of full phenomenon, and should be considered in future works.

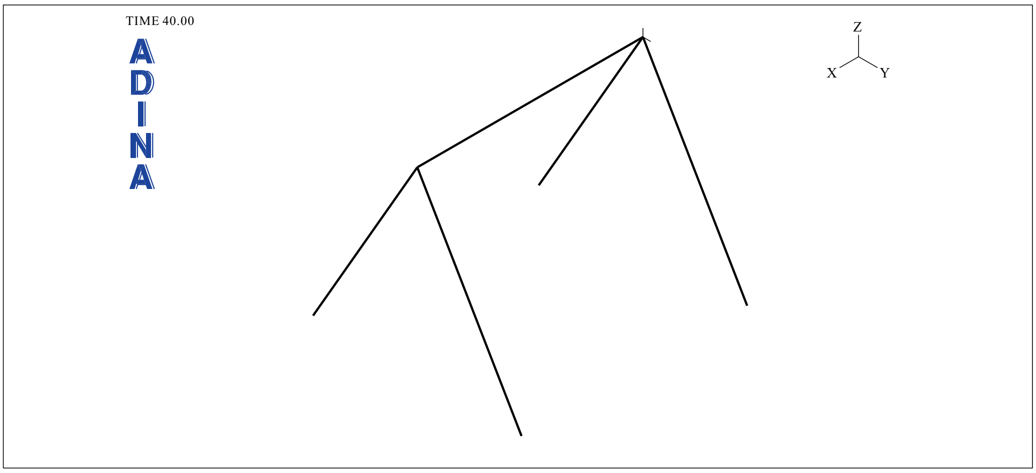

Fig. 11. ADINA modeling of one segment SFT

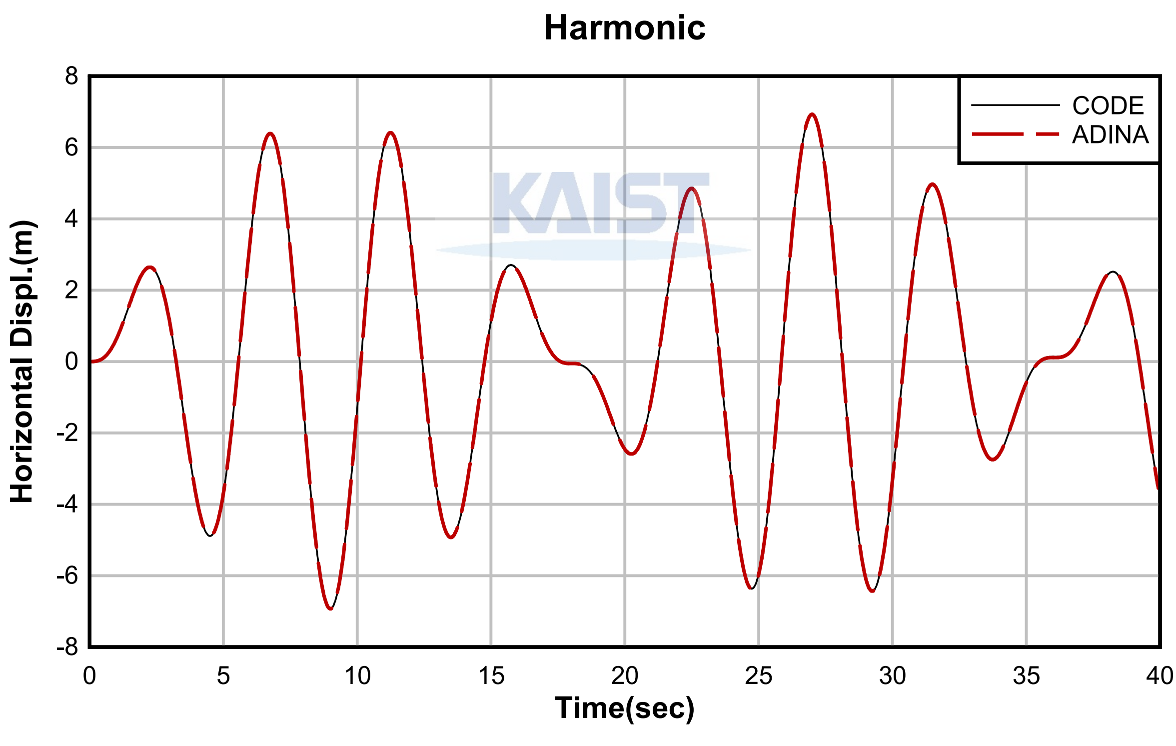

Fig. 12. Verification of SFT by comparing ADINA (harmonic, L=100m)

4.3 Modal analysis

By using the developed numerical analysis, we conduct modal analysis for suggested SFT. The added mass effect caused by fluid-structure interaction is added to the structure mass, natural frequencies are decreased compared with dry modes which neglect the hydrodynamic effects. By this reason, if the seismic ground motion is arrived to the SFT, it can occur resonance phenomenon at less frequencies. It can be a threat to the SFT safety condition.

Natural frequencies and dominant motion of suggested SFT model is indicated in Table. 3, and its mode shapes from first to thirtieth mode are illustrated in Figs.13-18 below.

Table. 3. Natural frequencies and dominent motion of suggested SFT model

Mode No.	Natural frequency (Hz)	Mode shape	Mode No.	Natural frequency (Hz)	Mode shape
1	0.57810	Horizontal	16	0.66603	Horizontal
2	0.57814	Horizontal	17	0.68749	Horizontal
3	0.57828	Horizontal	18	0.71212	Horizontal
4	0.57861	Horizontal	19	0.74003	Horizontal
5	0.57925	Horizontal	20	0.77131	Horizontal
6	0.58035	Horizontal	21	0.80601	Horizontal
7	0.58210	Horizontal	22	0.84413	Horizontal
8	0.58470	Horizontal	23	0.88568	Horizontal
9	0.58838	Horizontal	24	0.93064	Horizontal
10	0.59338	Horizontal	25	0.97704	X-rotational
11	0.59998	Horizontal	26	0.97896	Vertical
12	0.60844	Horizontal	27	1.00093	Vertical
13	0.61903	Horizontal	28	1.00095	Vertical
14	0.63200	Horizontal	29	1.00103	Vertical
15	0.64759	Horizontal	30	1.00121	Vertical

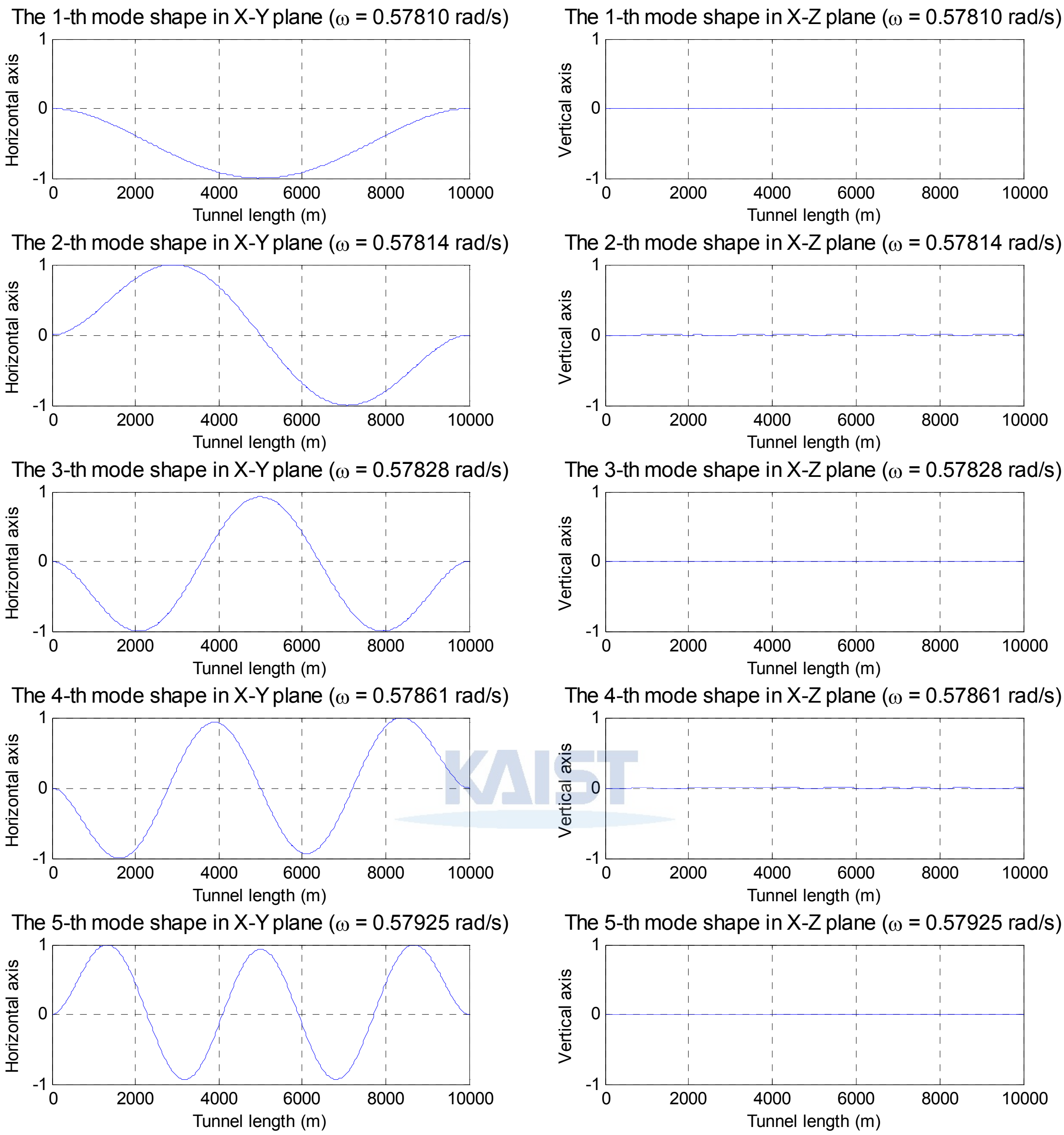

Fig. 13. Mode shapes of suggested SFT model (mode No. 1 ~ 5)

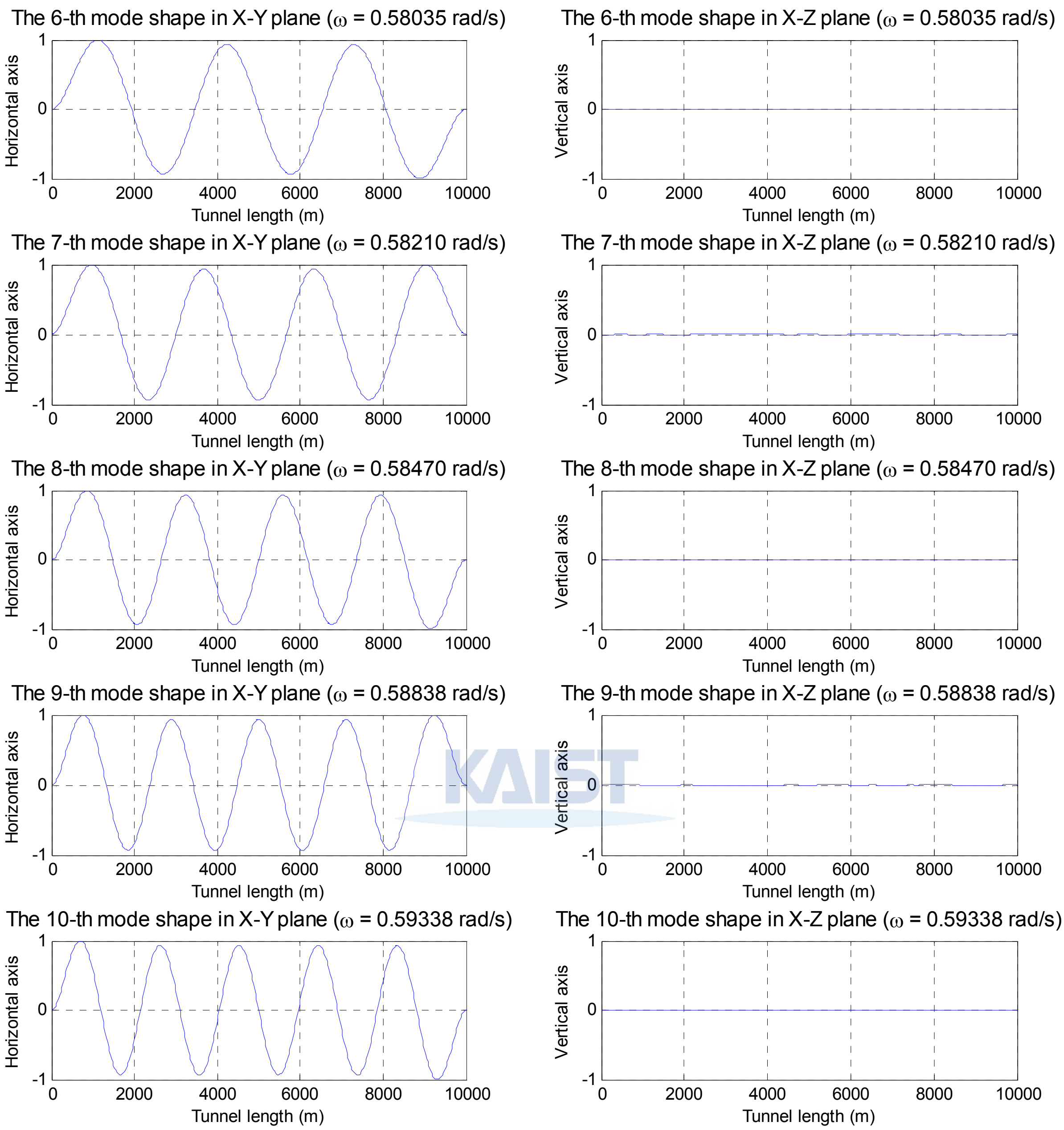

Fig. 14. Mode shapes of suggested SFT model (mode No. 6 ~ 10)

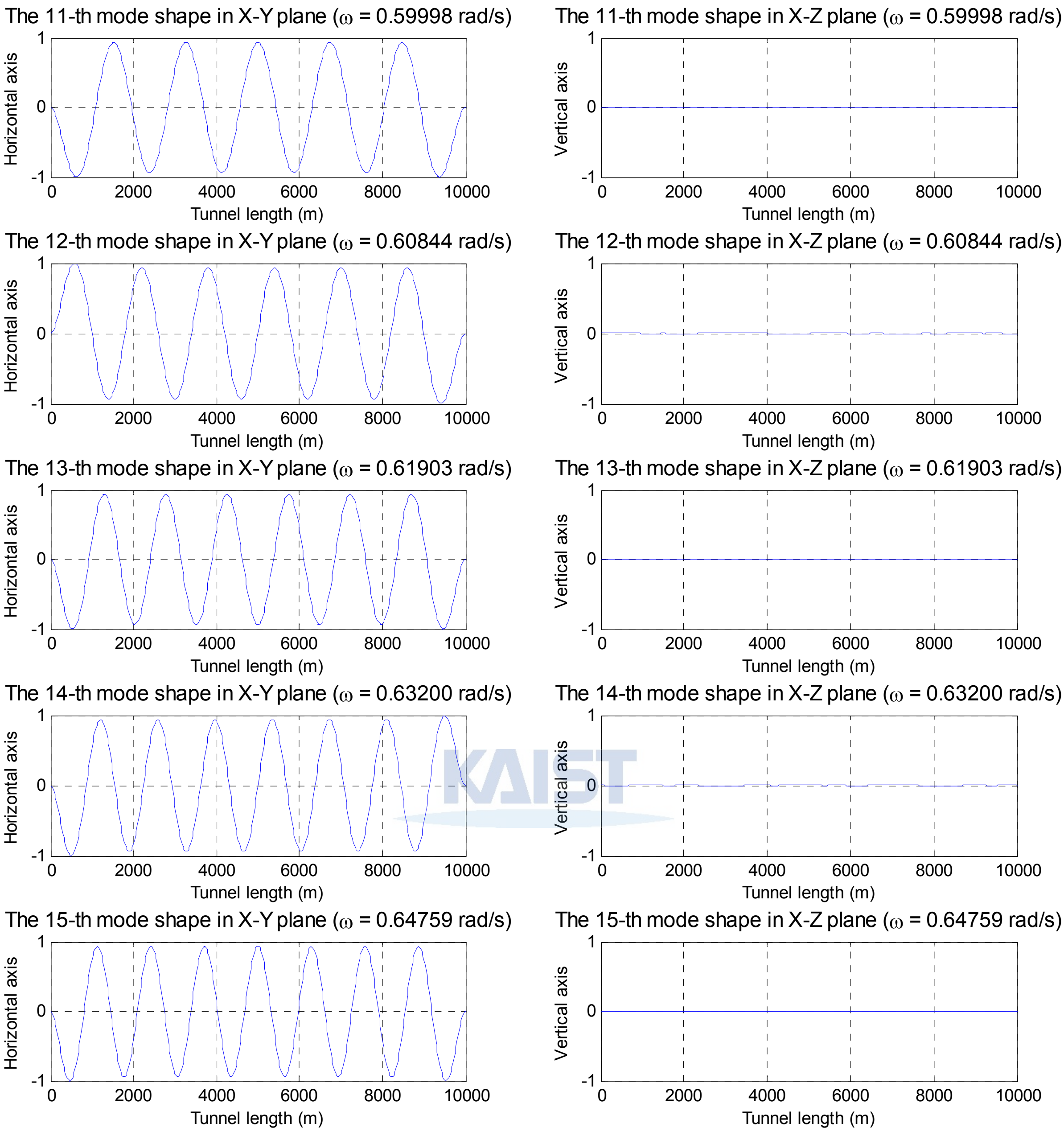

Fig. 15. Mode shapes of suggested SFT model (mode No. 11 ~ 15)

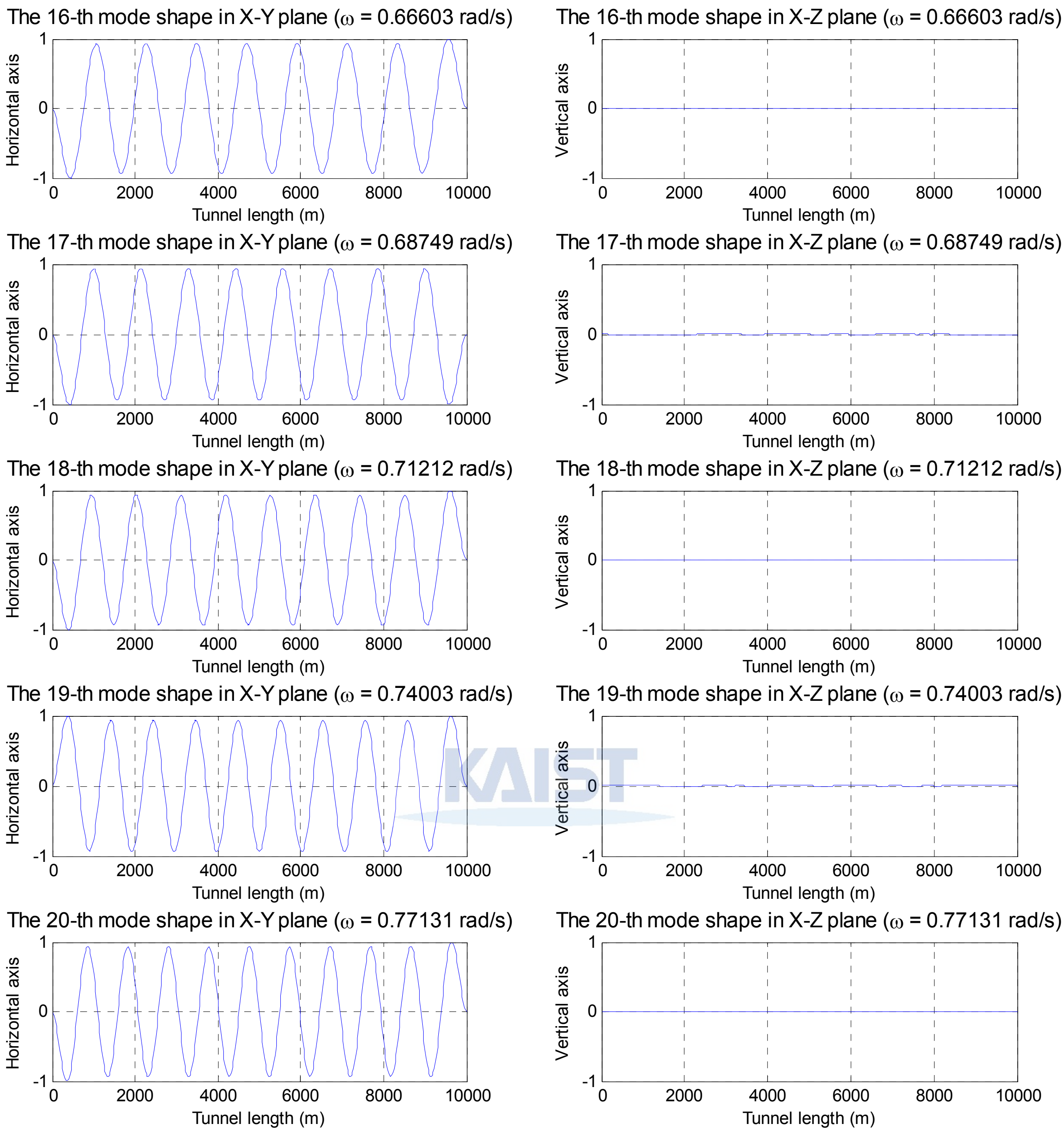

Fig. 16. Mode shapes of suggested SFT model (mode No. 16 ~ 20)

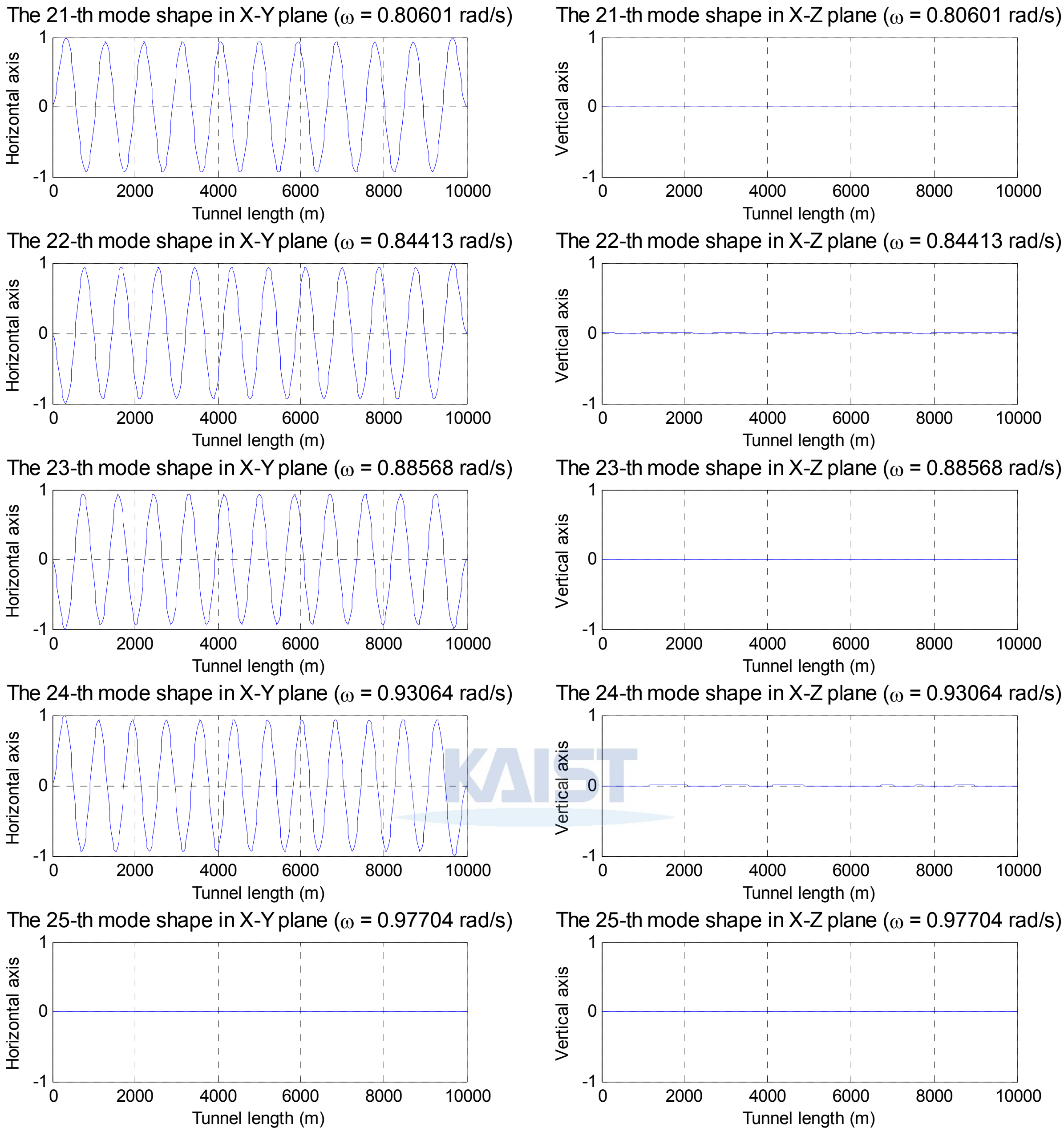

Fig. 17. Mode shapes of suggested SFT model (mode No. 21 ~ 25)

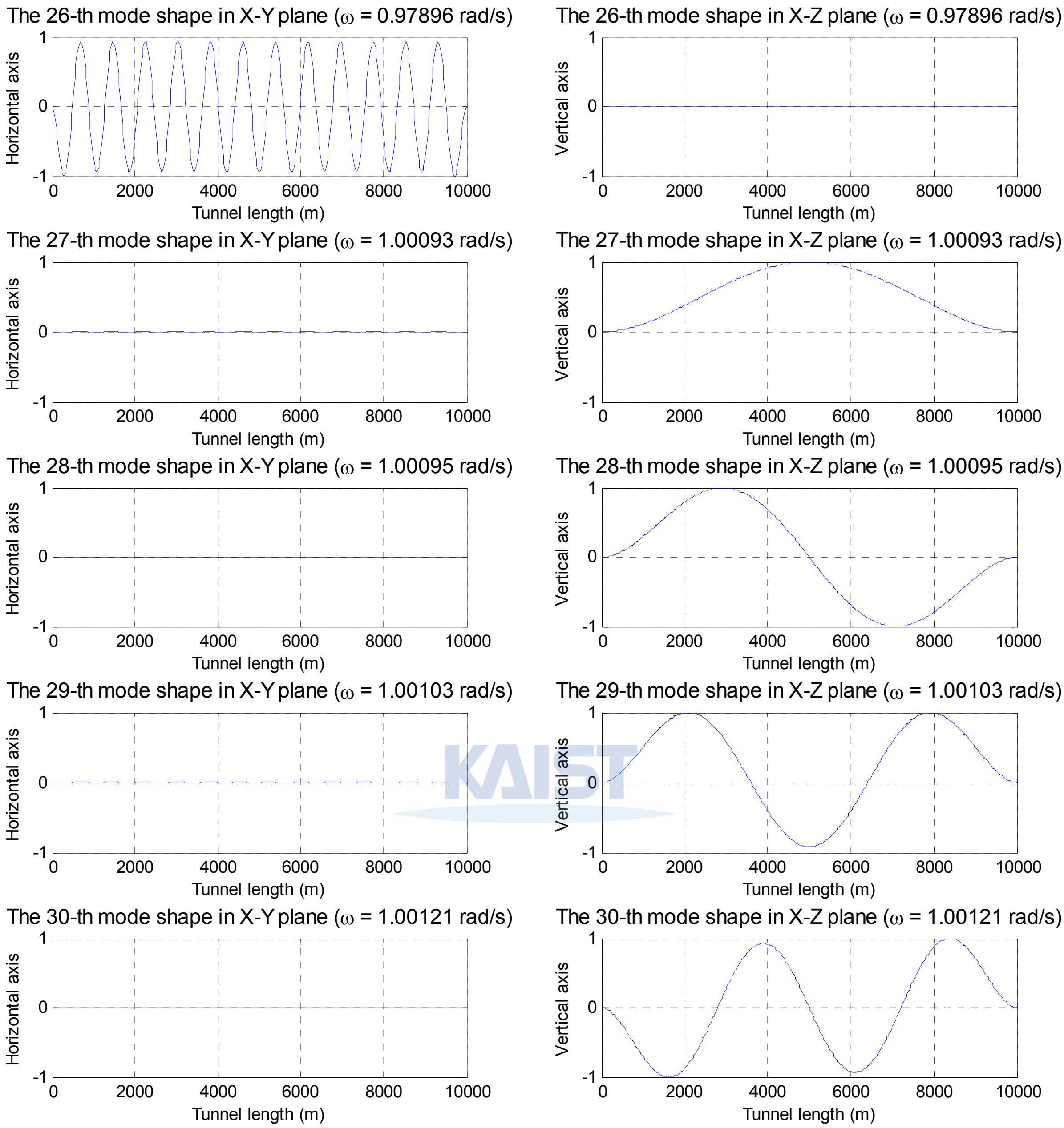

Fig. 18. Mode shapes of suggested SFT model (mode No. 26 ~ 30)

4.4 Displacement, velocity, acceleration responses of SFT

In this section, we studied about responses of suggested SFT model: displacement, velocity and acceleration. First, we considered the dominance of two hydrodynamic effects: inertia and drag. Next, we discussed the maximum response distributions through the tunnel length and chose two location to see the time history of responses. Two locations are the highest horizontal displacement response point and midpoint of tunnel length. Because SFT is very slender structure relative to its diameter, so horizontal motion of SFT can be more dangerous to the safety of structure and inner transportation than longitudinal motion. Finally, we discussed the responses time history at chosen points.

4.4.1 Dominance of inertia & drag effect of fluid

Before analyzing the seismic responses of SFT considering fluid-structure interaction, we discussed the dominance of two hydrodynamic effects. In Fig.19, we showed the horizontal displacement response at midpoint of SFT when El Centro earthquake was acted. There were two cases, considering only inertia effect or both inertia and drag effect.

As a result, inertia effect is dominant because SFT is in still water and it does not oscillate far enough relative to its diameter. So, we can neglect drag effect in this condition.

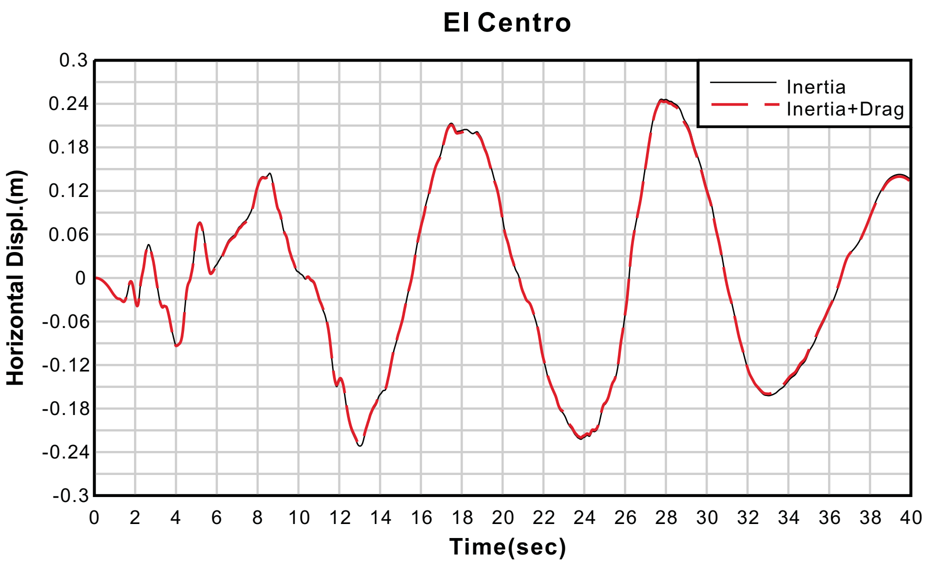

Fig. 19. Dominance of inertia & drag effect of fluid

4.4.2 Maximum response distribution of SFT

We discussed the maximum response distributions through the tunnel length. The maximum responses are occurred when seismic excitation angle $\theta = 0\deg.$ or $\theta = 90\deg.$, these are maximum longitudinal and horizontal case, respectively. For the three ground motions, we described the envelope of maximum displacement, velocity and acceleration response in Figs. 20-28 below.

The SFT satisfy bilateral symmetry, all responses also satisfy this condition between both ends. For all horizontal responses, rapid changes of motion is occurred at near the tunnel ends. Furthermore, the highest response of horizontal displacement, velocity and acceleration are also occurred at the point in 1km from the tunnel ends. On the other hand, longitudinal responses are distributed with different trend. Maximum response distribution is described more smoothly than that of horizontal cases through the tunnel length. In most cases, the highest longitudinal responses are occurred at the midpoint.

By these results, we chose two locations which were mentioned previously. For the harmonic, El Centro and Kobe ground motion, not only the midpoint of tunnel, but also each of the highest horizontal displacement points were decided at $x = 900m$, $x = 500m$ and $x = 400m$ in this order.

This suggested SFT model has similar motion widely in middle section. The main reason is the identical support excitation. So if we can consider multiple support excitation, its trends will be changed and also we estimate the magnitude of responses will be decreased.

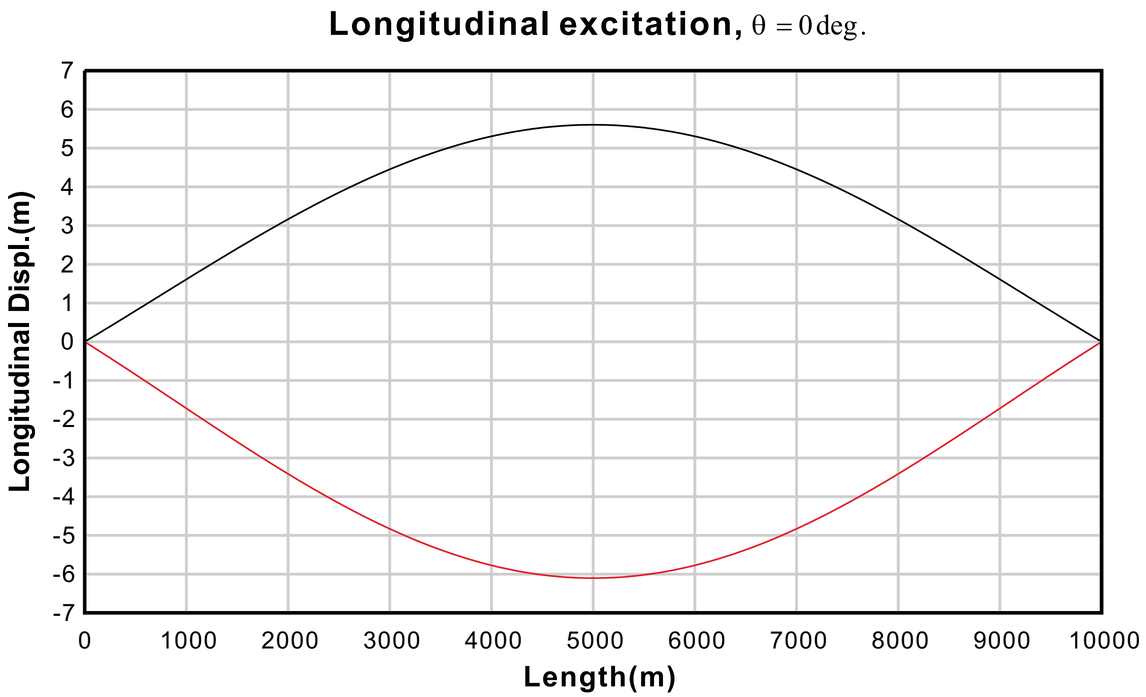

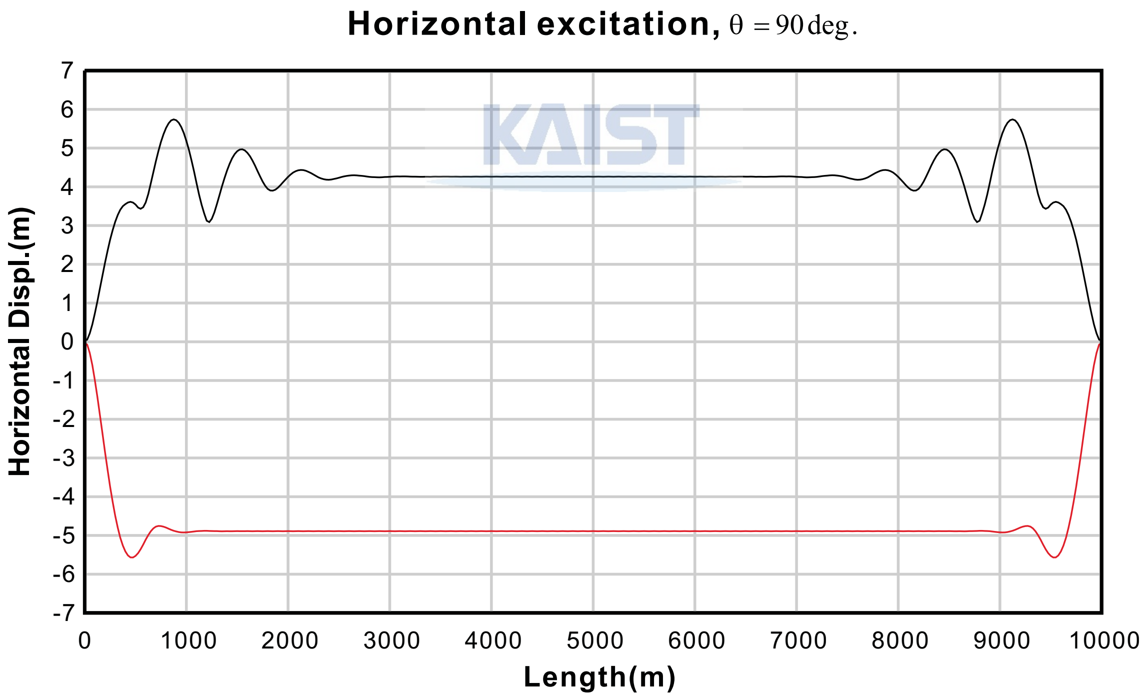

Fig. 20. Envelope of maximum displacement response for harmonic ground motion

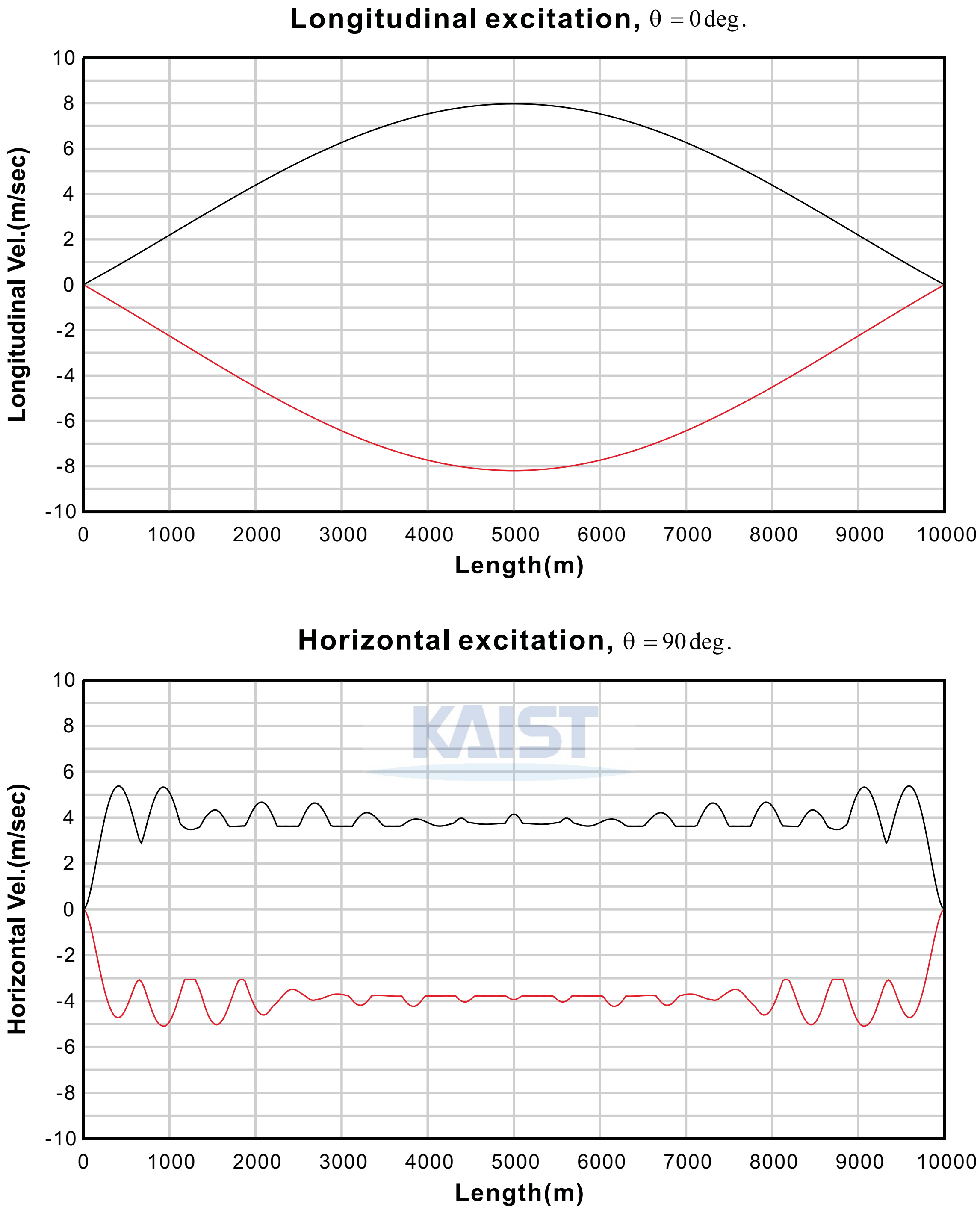

Fig. 21. Envelope of maximum velocity response for harmonic ground motion

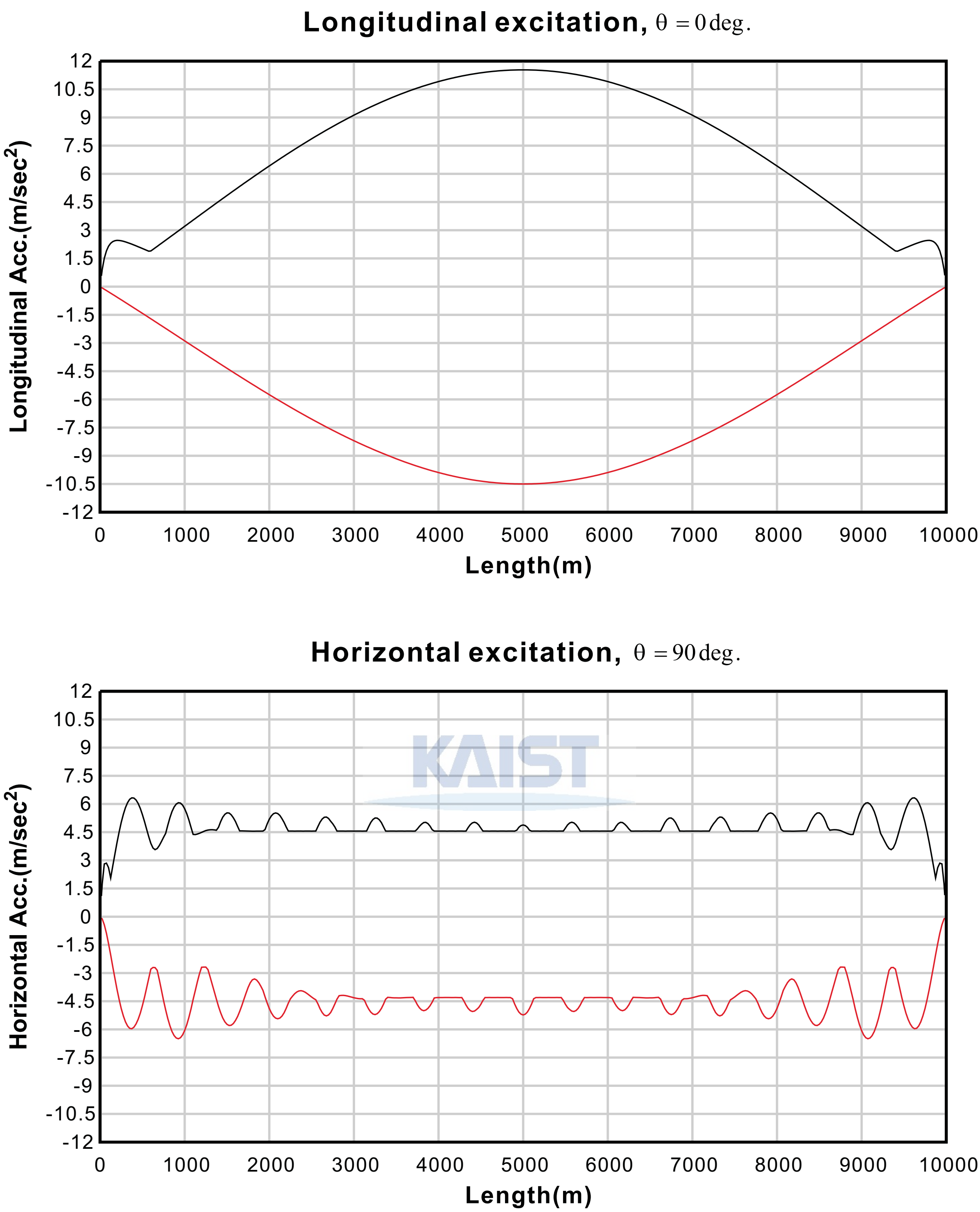

Fig. 22. Envelope of maximum acceleration response for harmonic ground motion

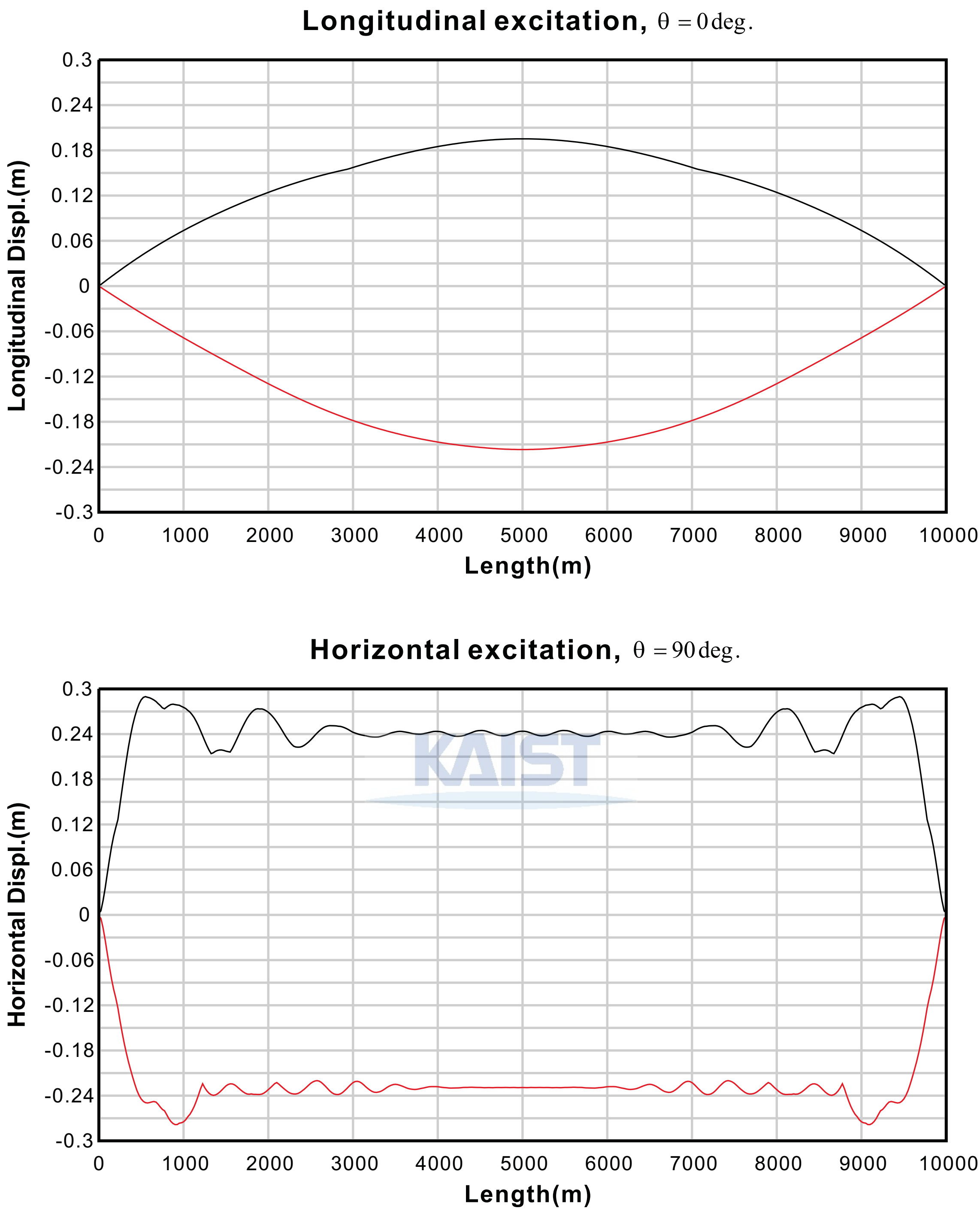

Fig. 23. Envelope of maximum displacement response for El Centro ground motion

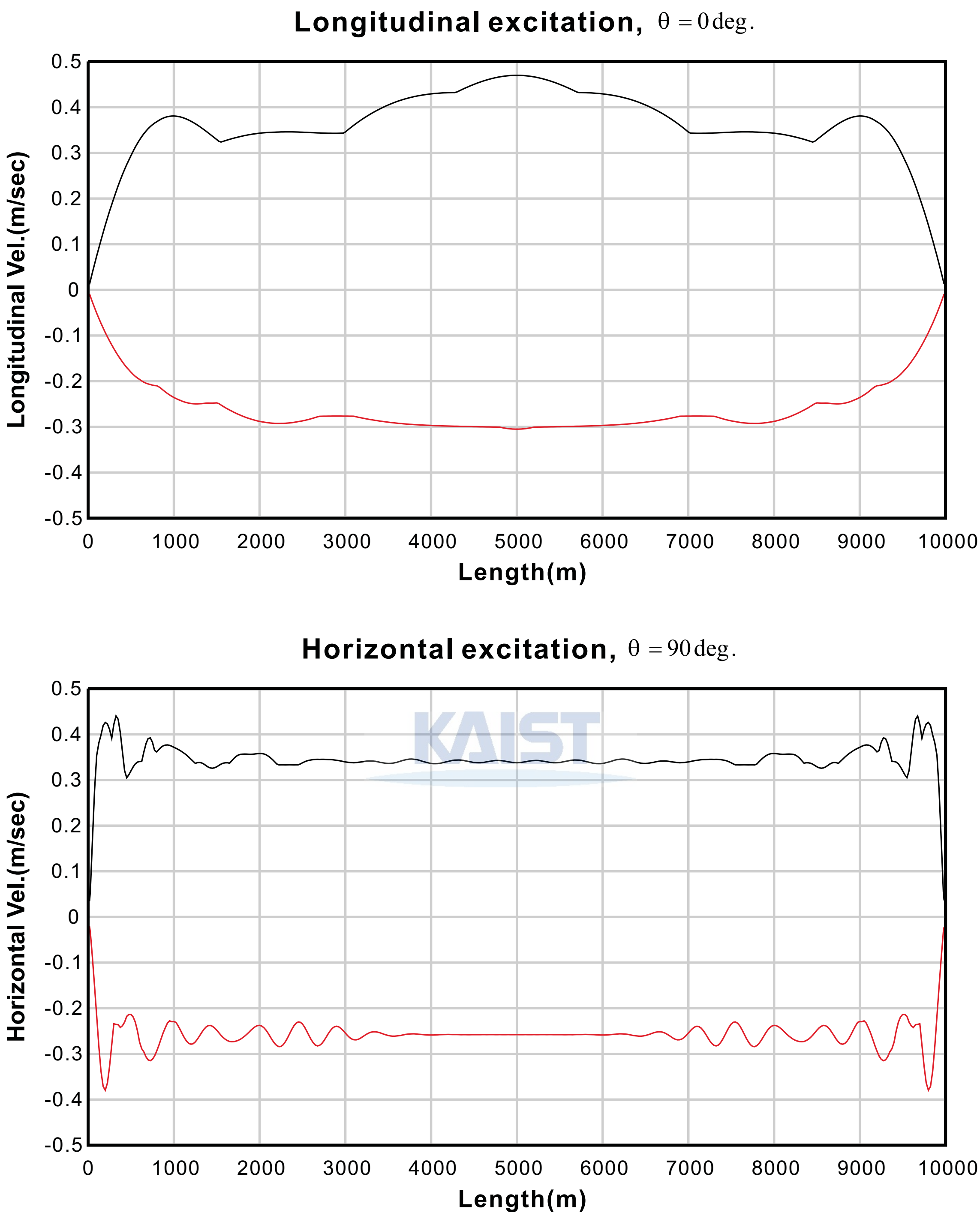

Fig. 24. Envelope of maximum velocity response for El Centro ground motion

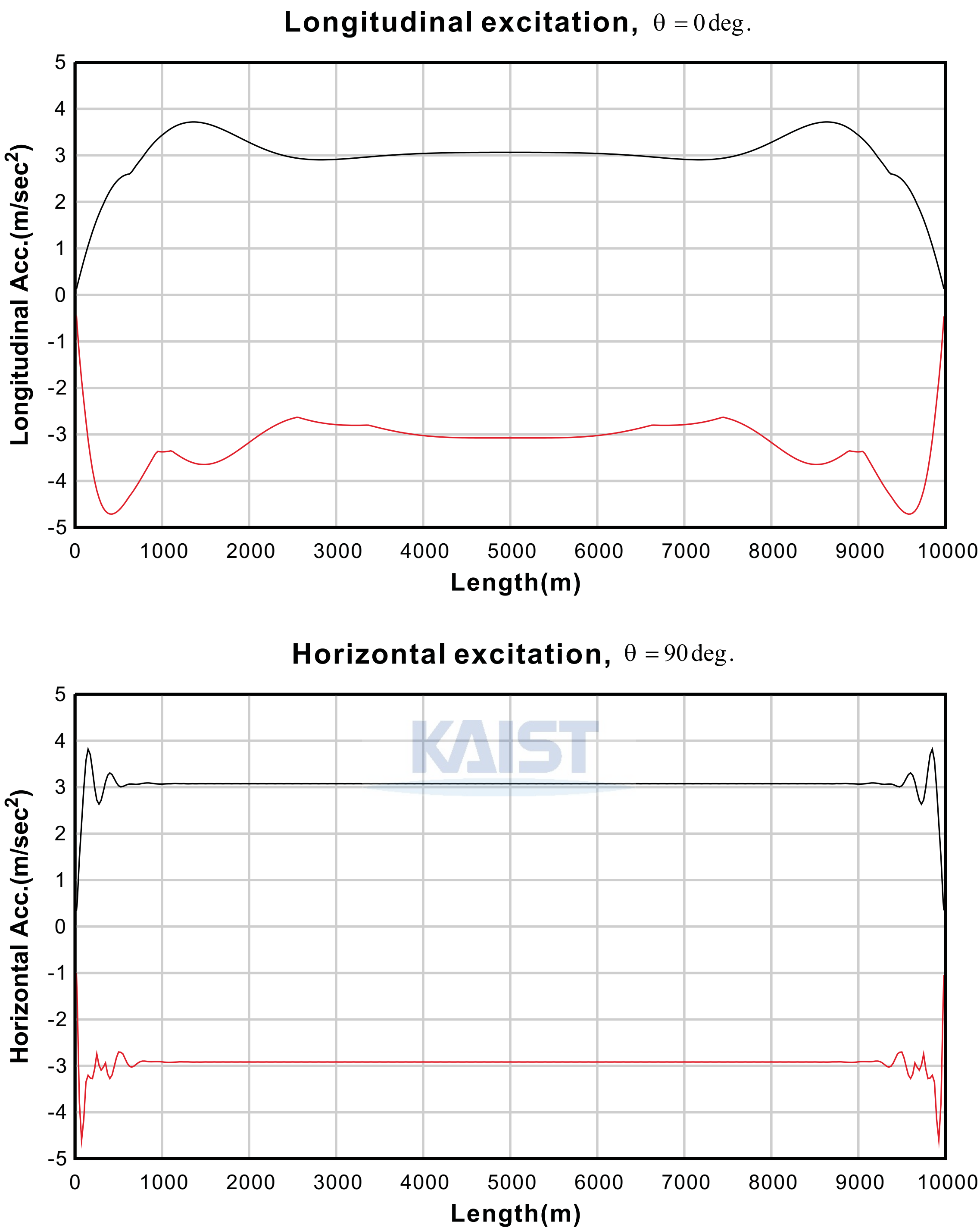

Fig. 25. Envelope of maximum acceleration response for El Centro ground motion

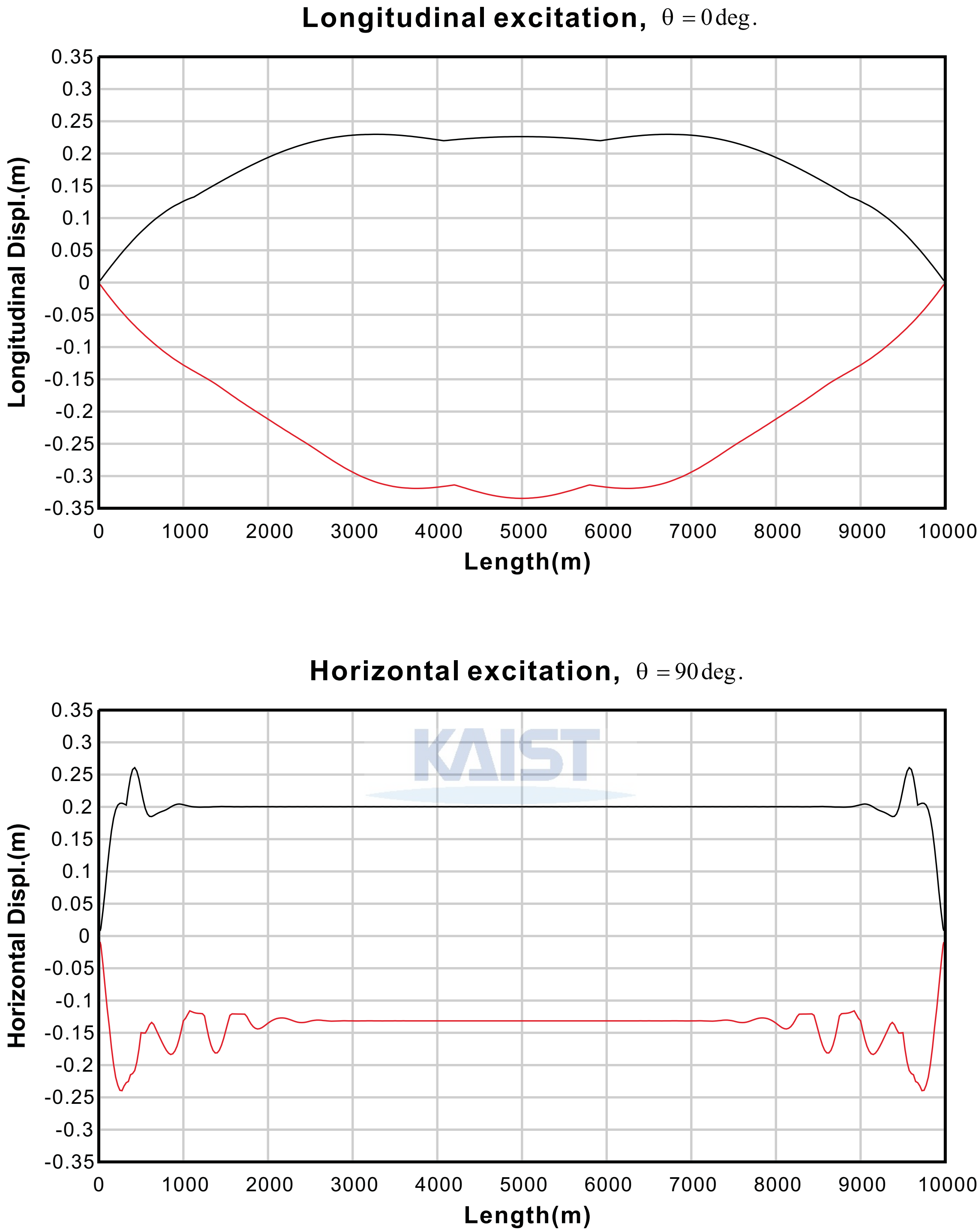

Fig. 26. Envelope of maximum displacement response for Kobe ground motion

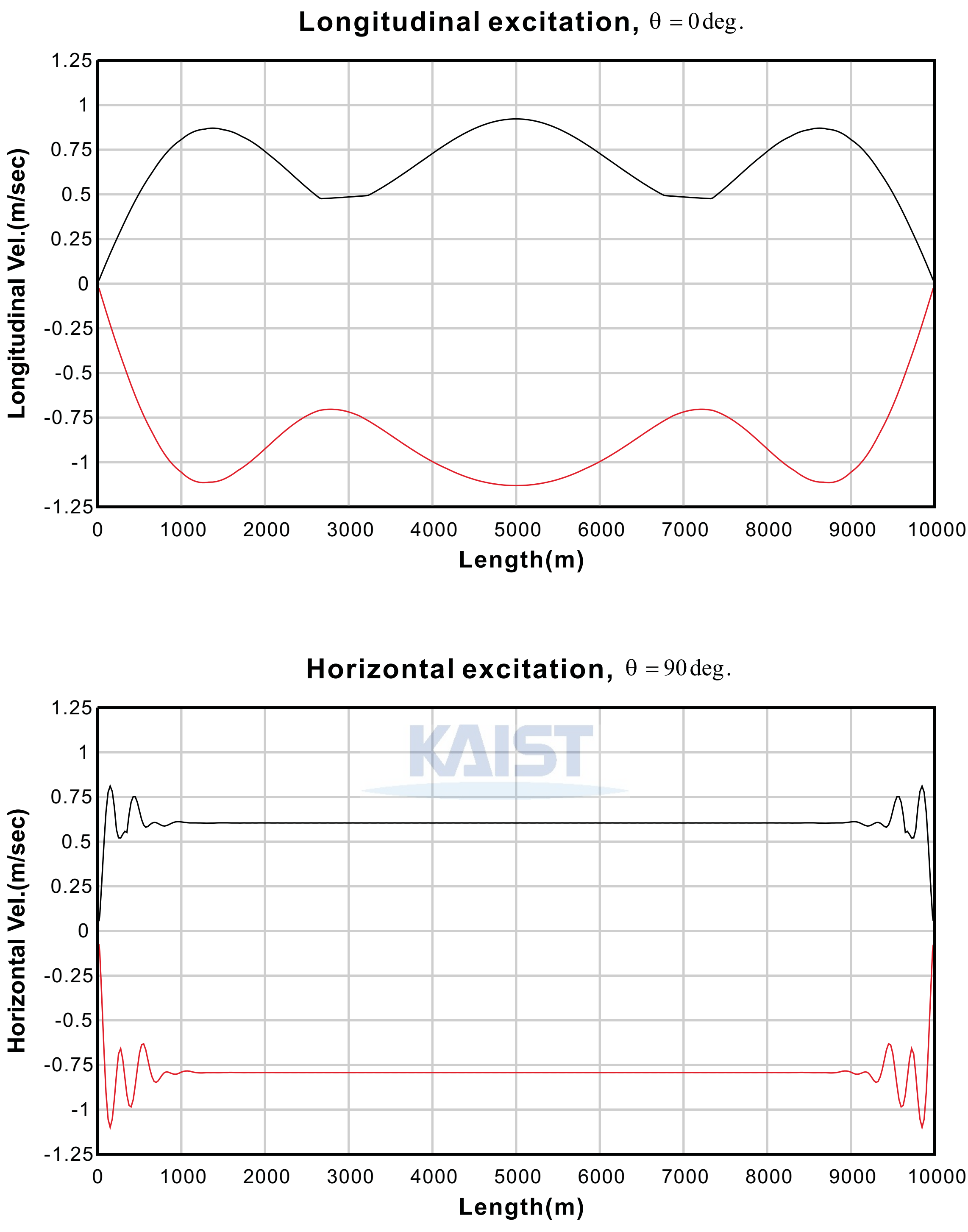

Fig. 27. Envelope of maximum velocity response for Kobe ground motion

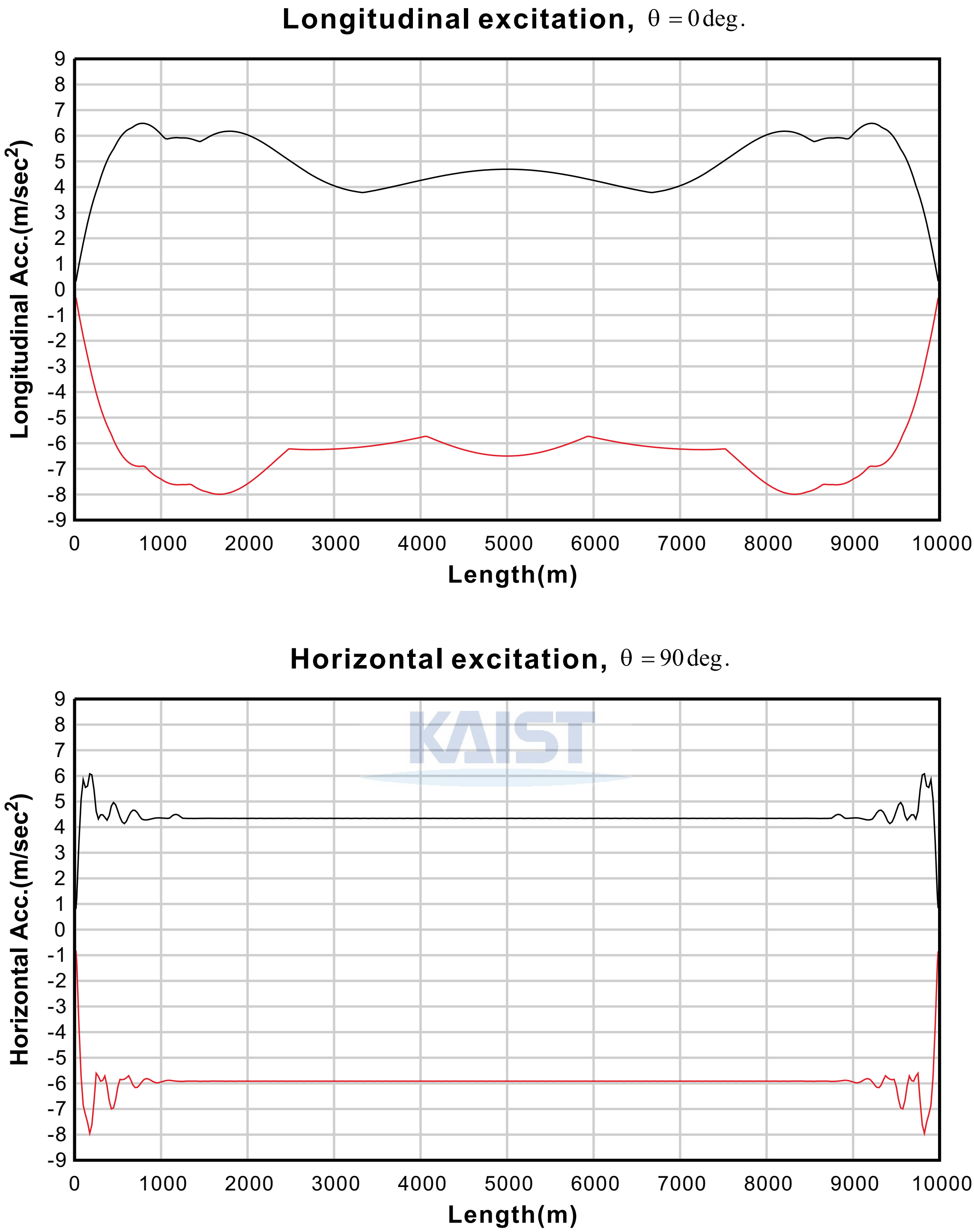

Fig. 28. Envelope of maximum acceleration response for Kobe ground motion

Table. 4. Magnitudes of maximum response for three ground motions

Ground motion		Max. Displ. (m)	Max. Vel. ($m/\sec$)	Max. Acc. ($m/\sec^2$)
Harmonic	Longitudinal	6.1026	8.1931	11.5330
	Horizontal	5.7402	5.3754	6.3287
El Centro	Longitudinal	0.2168	0.4698	4.7125
	Horizontal	0.2897	0.4402	4.5995
Kobe	Longitudinal	0.3346	1.1305	7.9926
	Horizontal	0.2608	1.0996	7.9510

From the Table.4, we can compare the responses of two real ground motions. The peak ground acceleration (PGA) of Kobe earthquake is bigger than that of El Centro earthquake, responses also show same trends.

4.4.3 Time history of displacement, velocity and acceleration responses

We conducted the time analysis to find the responses time history at chosen points. We changed the excitation angle of seismic motion from 0 to $90\,\text{deg.}$, and showed the time history of displacement, velocity and acceleration in longitudinal and horizontal direction, respectively. All of responses are illustrated from Figs. 29-64 below.

In harmonic ground motion, we can find the time history curve of responses are different between two directions. The reason is inertial effect from fluid-structure interaction, added mass is effected on horizontal structure mass. In longitudinal direction, only structural mass is taken for seismic load. Also, the frequency of harmonic ground motion is lower than range of SFT natural frequencies, resonance is not occurred. As a result, magnitude of horizontal responses are lower than these of longitudinal responses.

In two real ground motion, they have the range of frequencies and these are included the natural frequencies of suggested SFT model. Because of hydrodynamic effect, natural frequency can be founded much lower frequency level. So we estimate that it can increase the dynamic responses of SFT.

4.4.3.1 Displacement responses time history

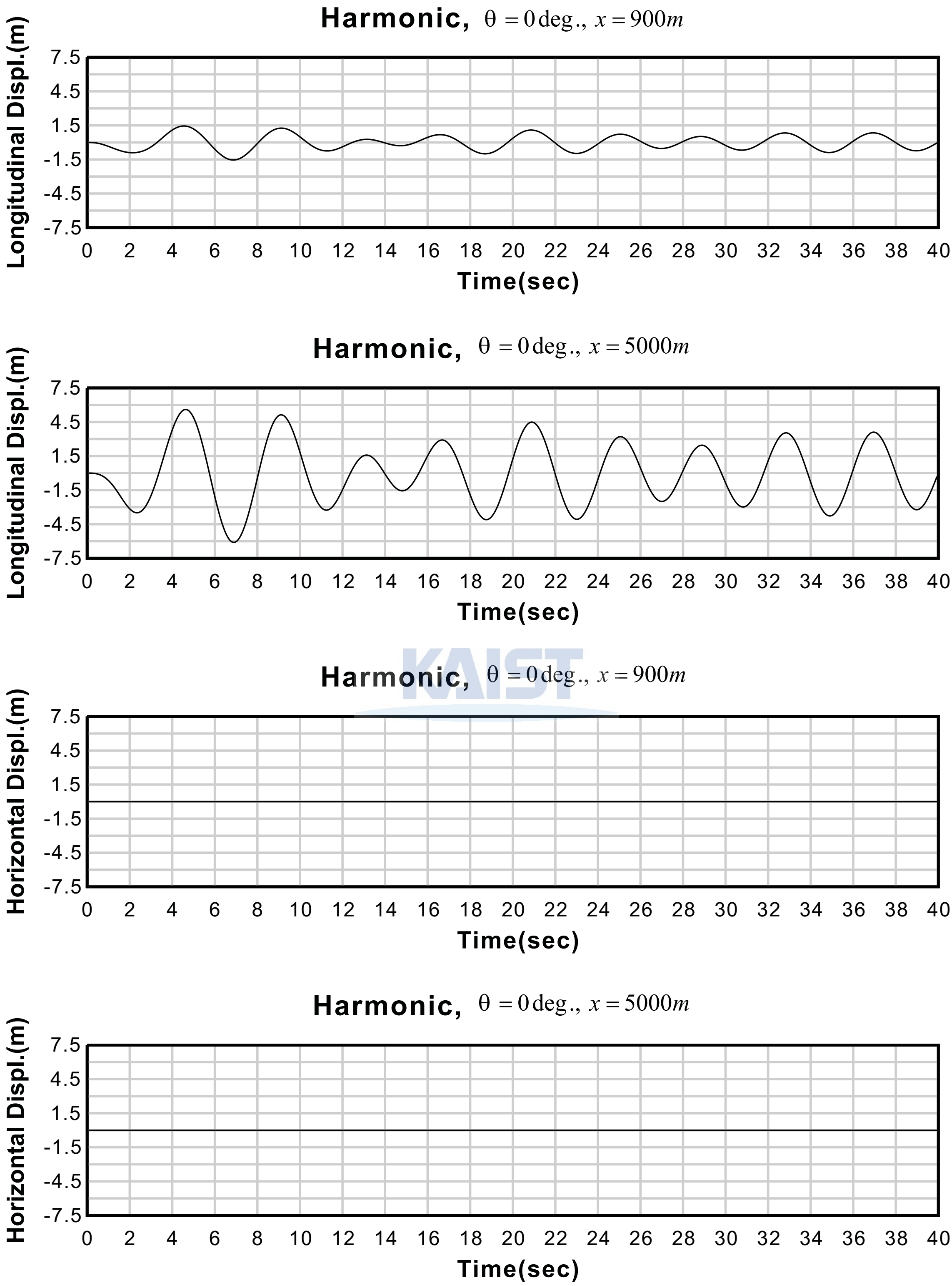

Fig. 29. Displacement response time history for harmonic ground motion, $\theta = 0\deg.$

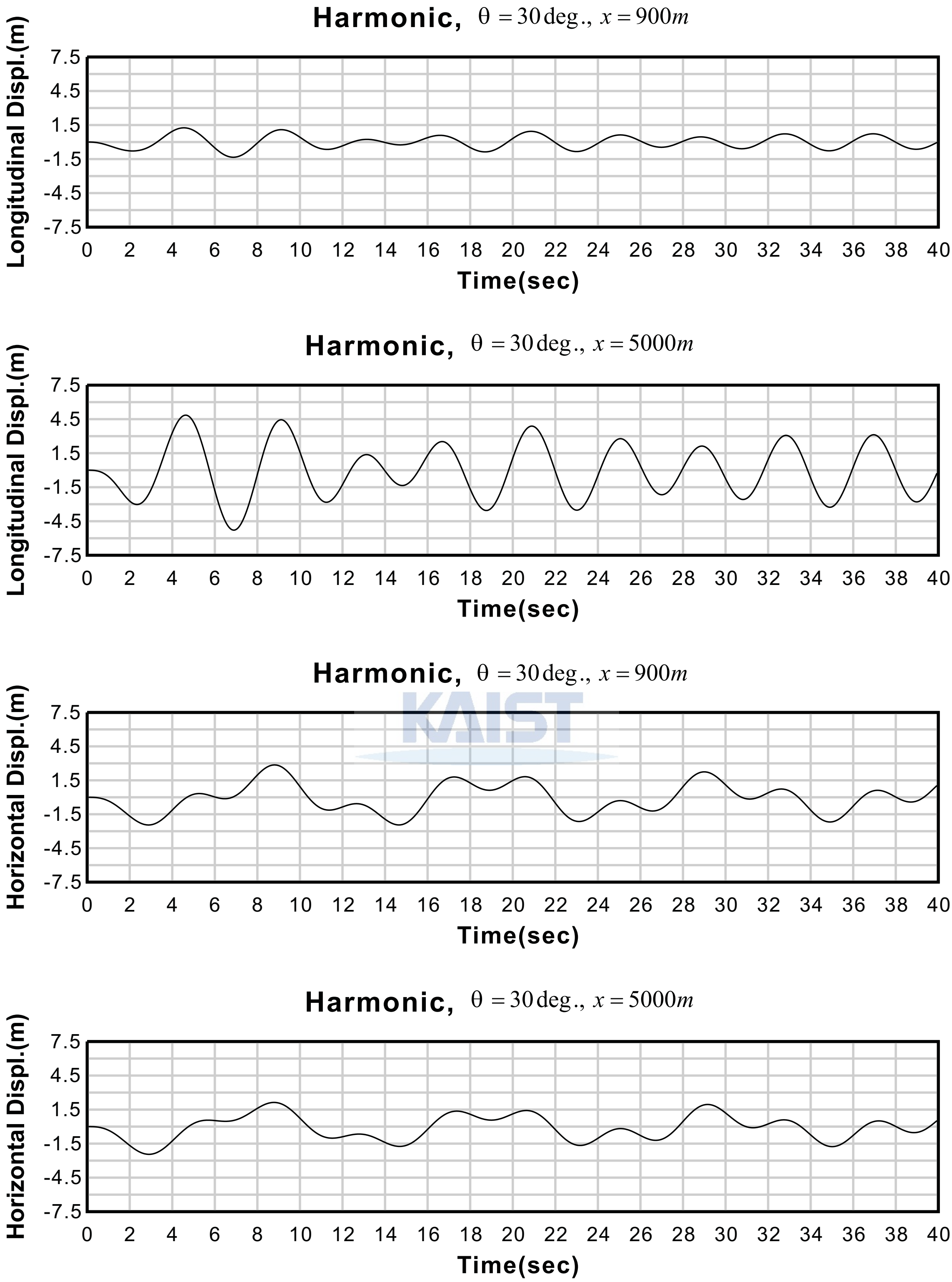

Fig. 30. Displacement response time history for harmonic ground motion, $\theta = 30\,\deg.$

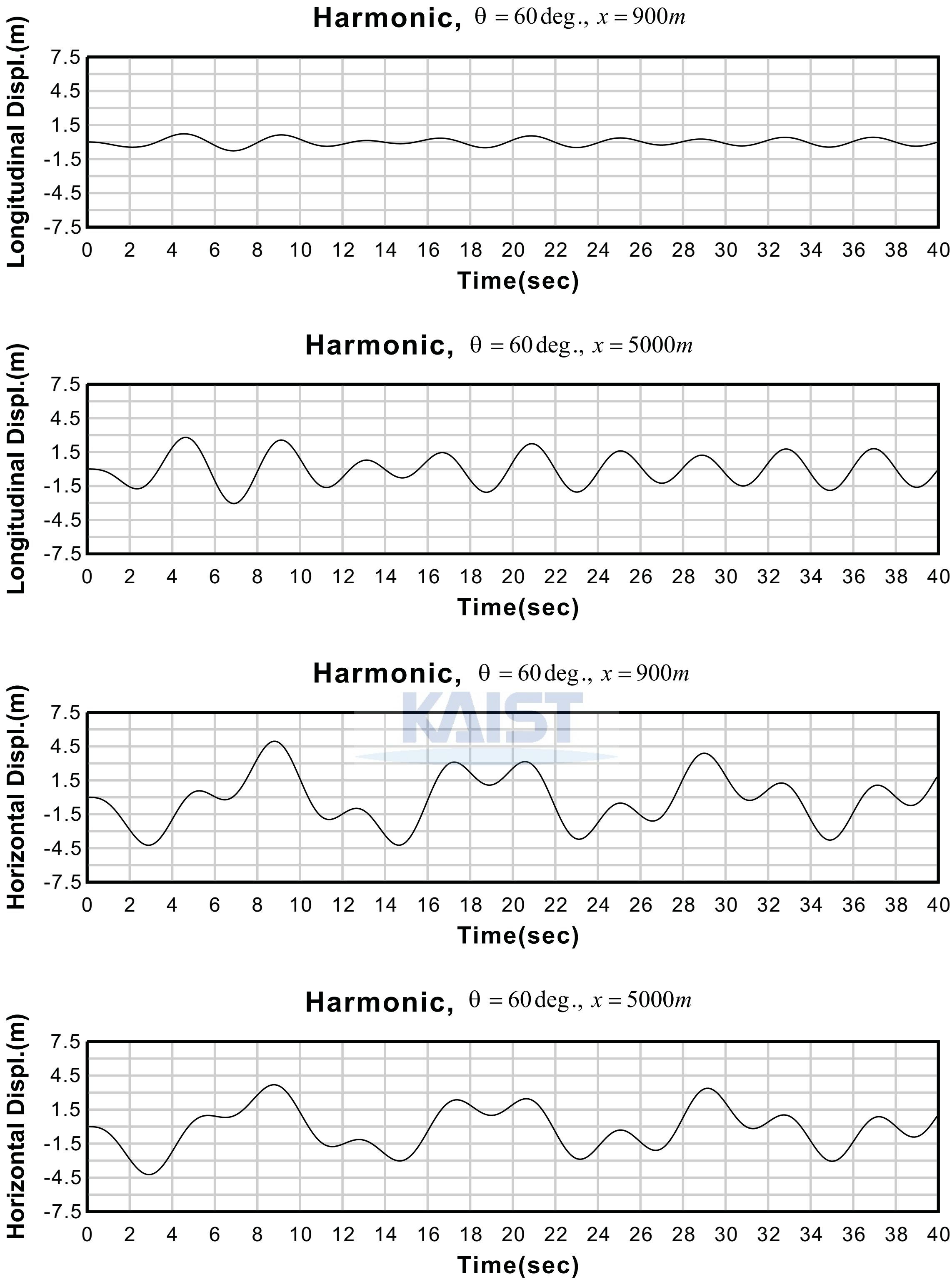

Fig. 31. Displacement response time history for harmonic ground motion, $\theta = 60\,\deg.$

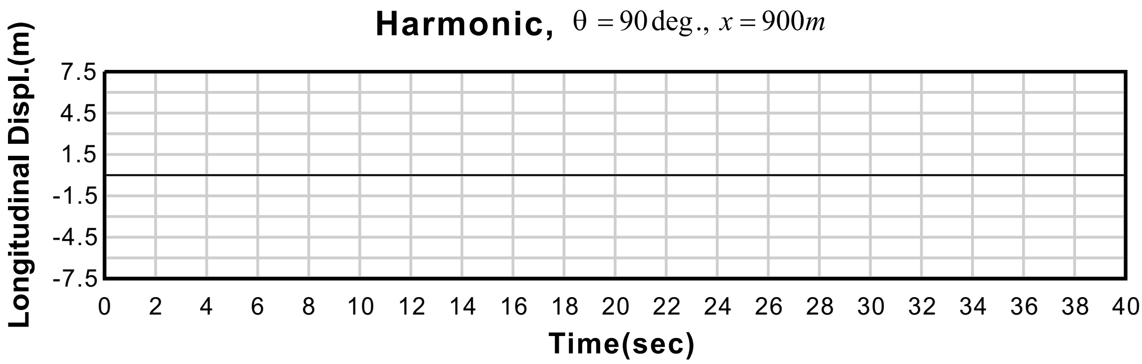

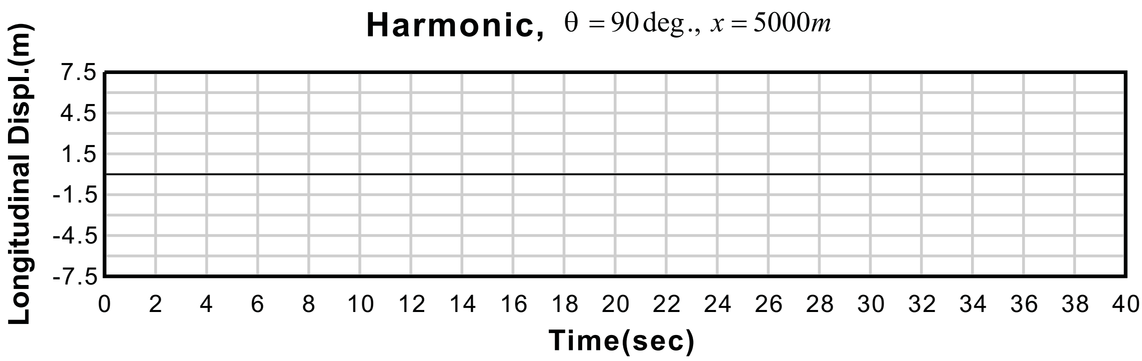

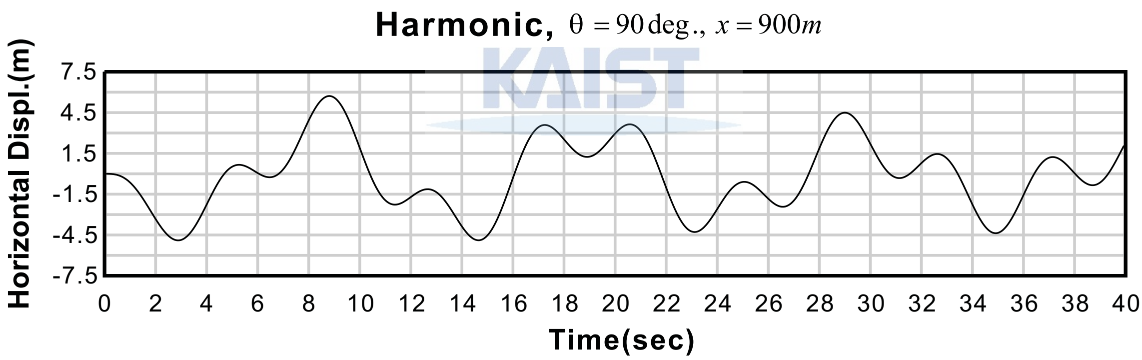

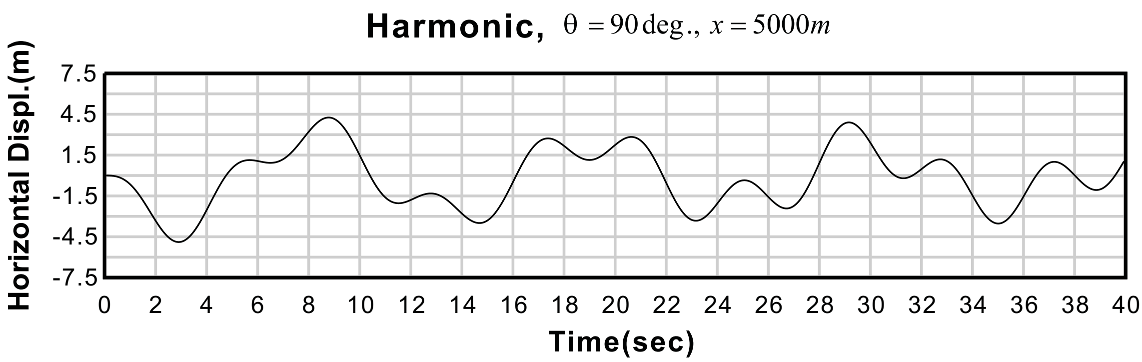

Fig. 32. Displacement response time history for harmonic ground motion, $\theta = 90\,\deg.$

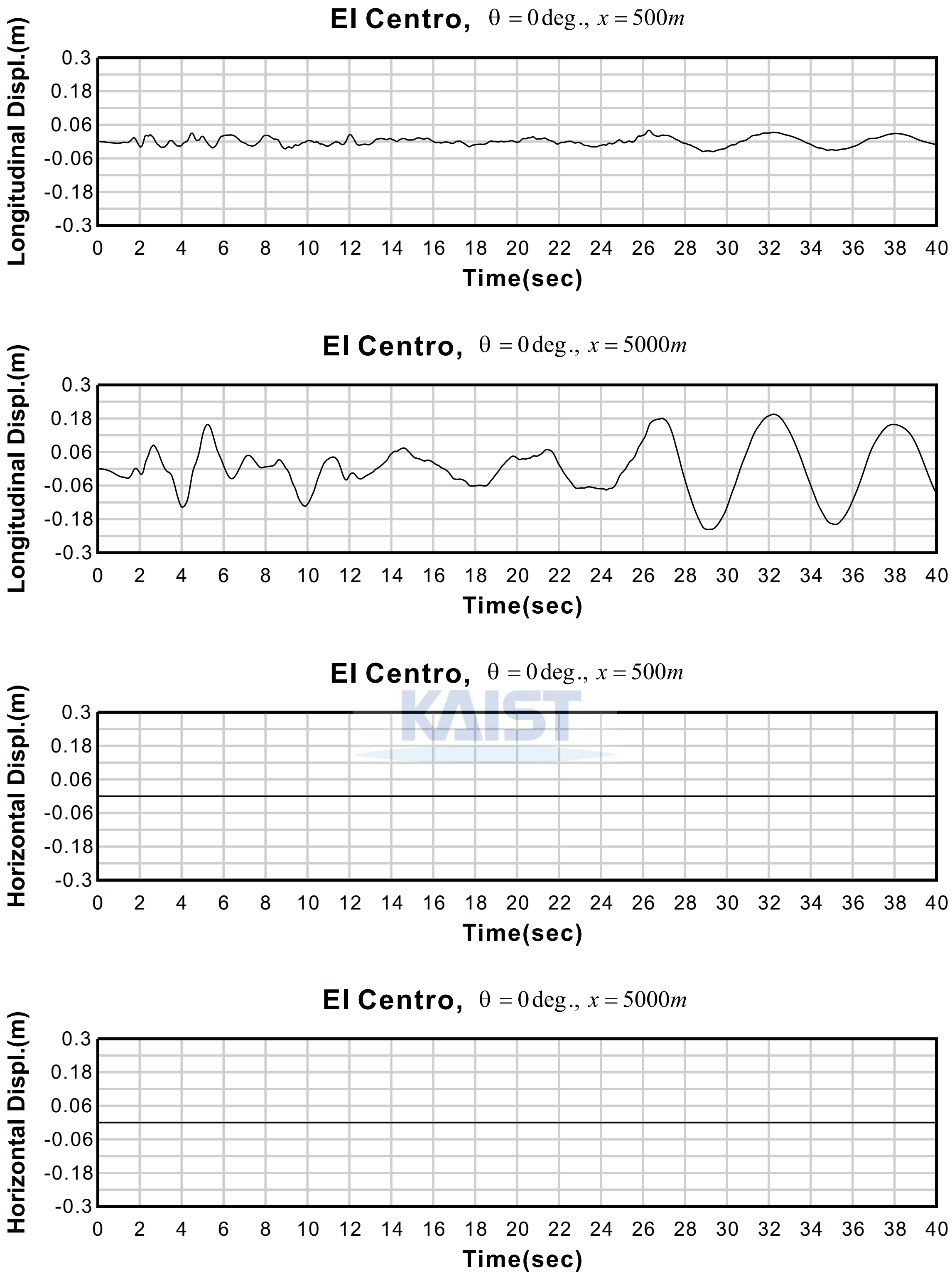

Fig. 33. Displacement response time history for El Centro ground motion, $\theta = 0\,\text{deg}.$

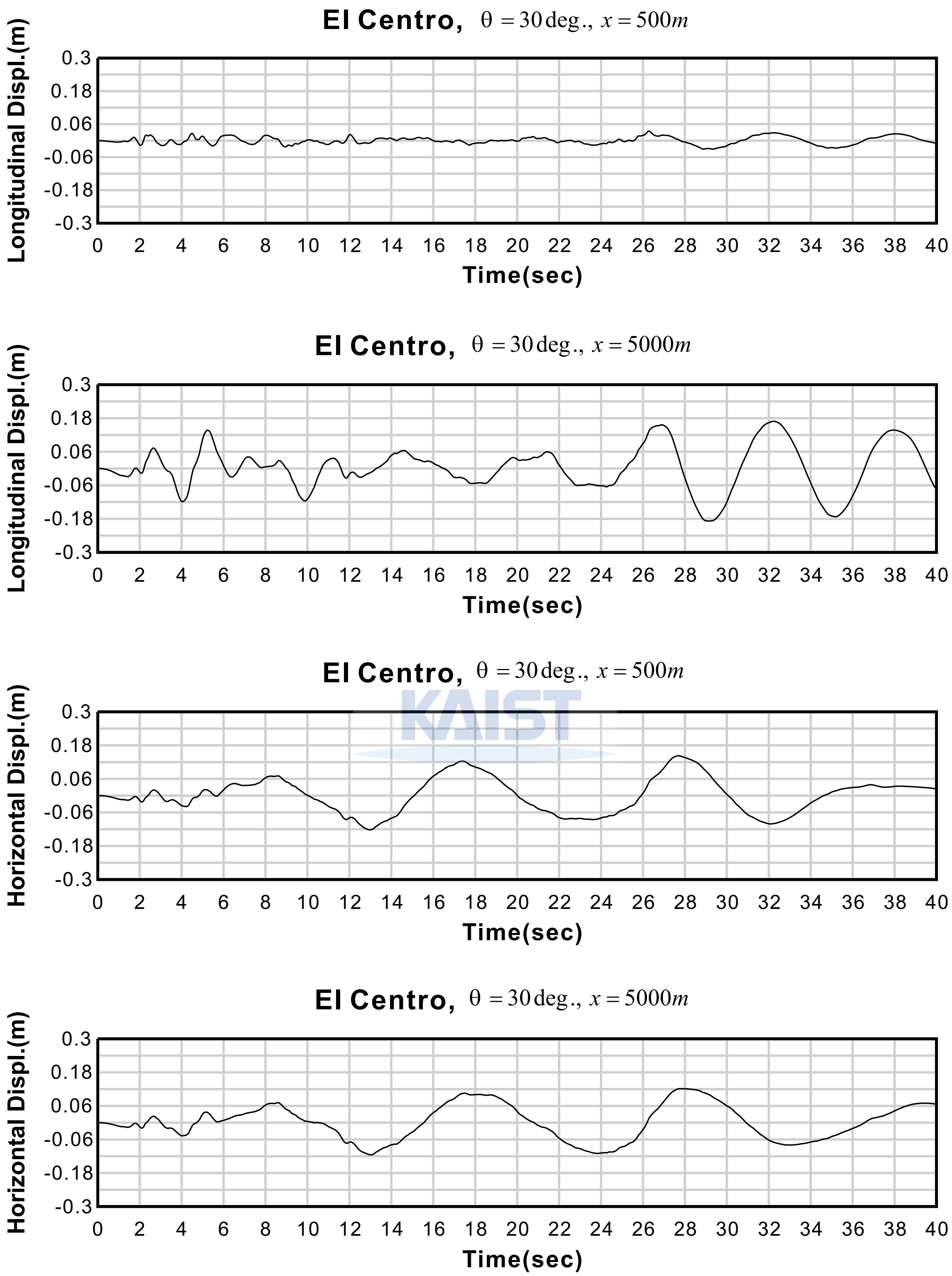

Fig. 34. Displacement response time history for El Centro ground motion, $\theta = 30\,\text{deg.}$

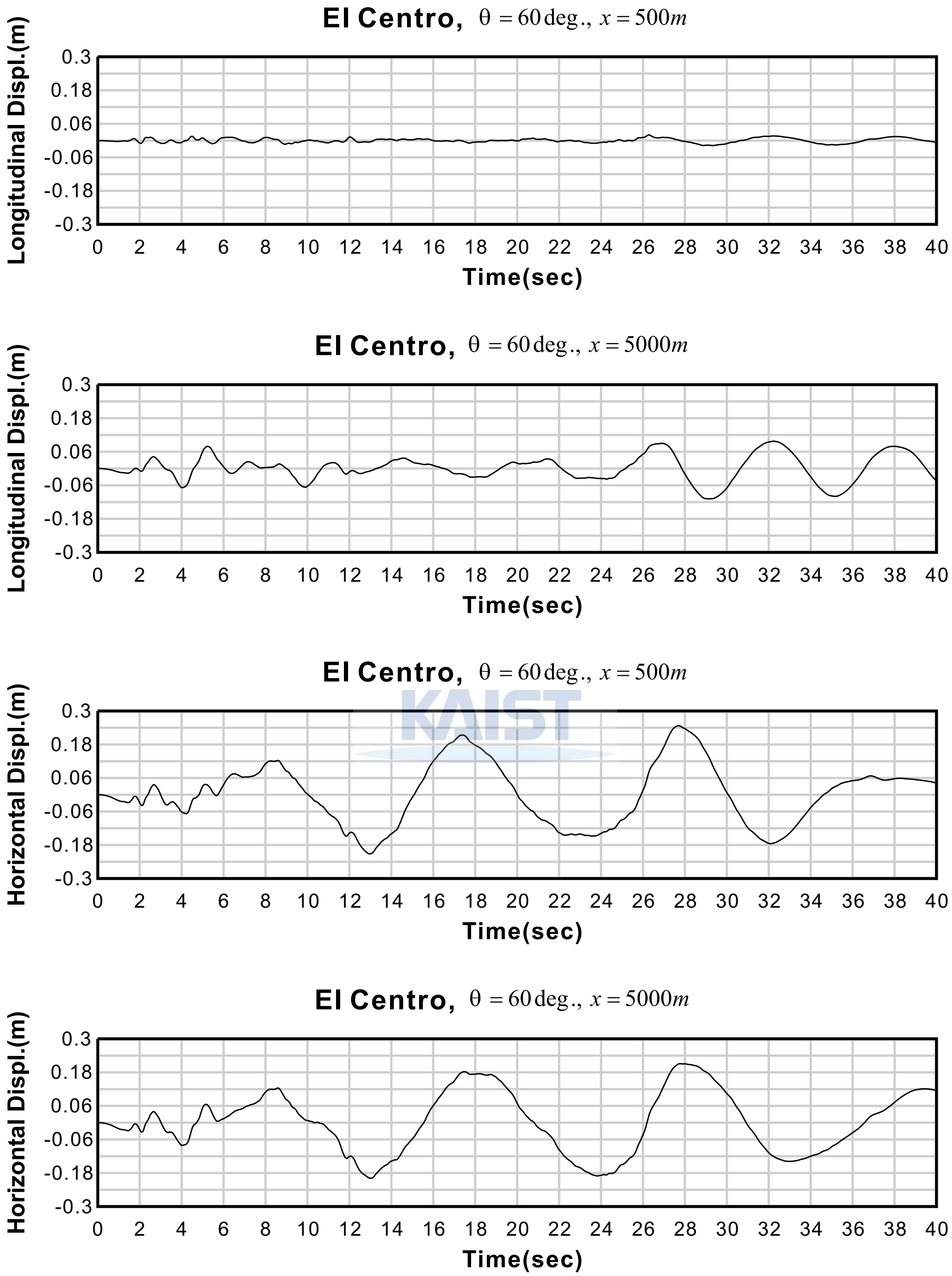

Fig. 35. Displacement response time history for El Centro ground motion, $\theta = 60\,\text{deg.}$

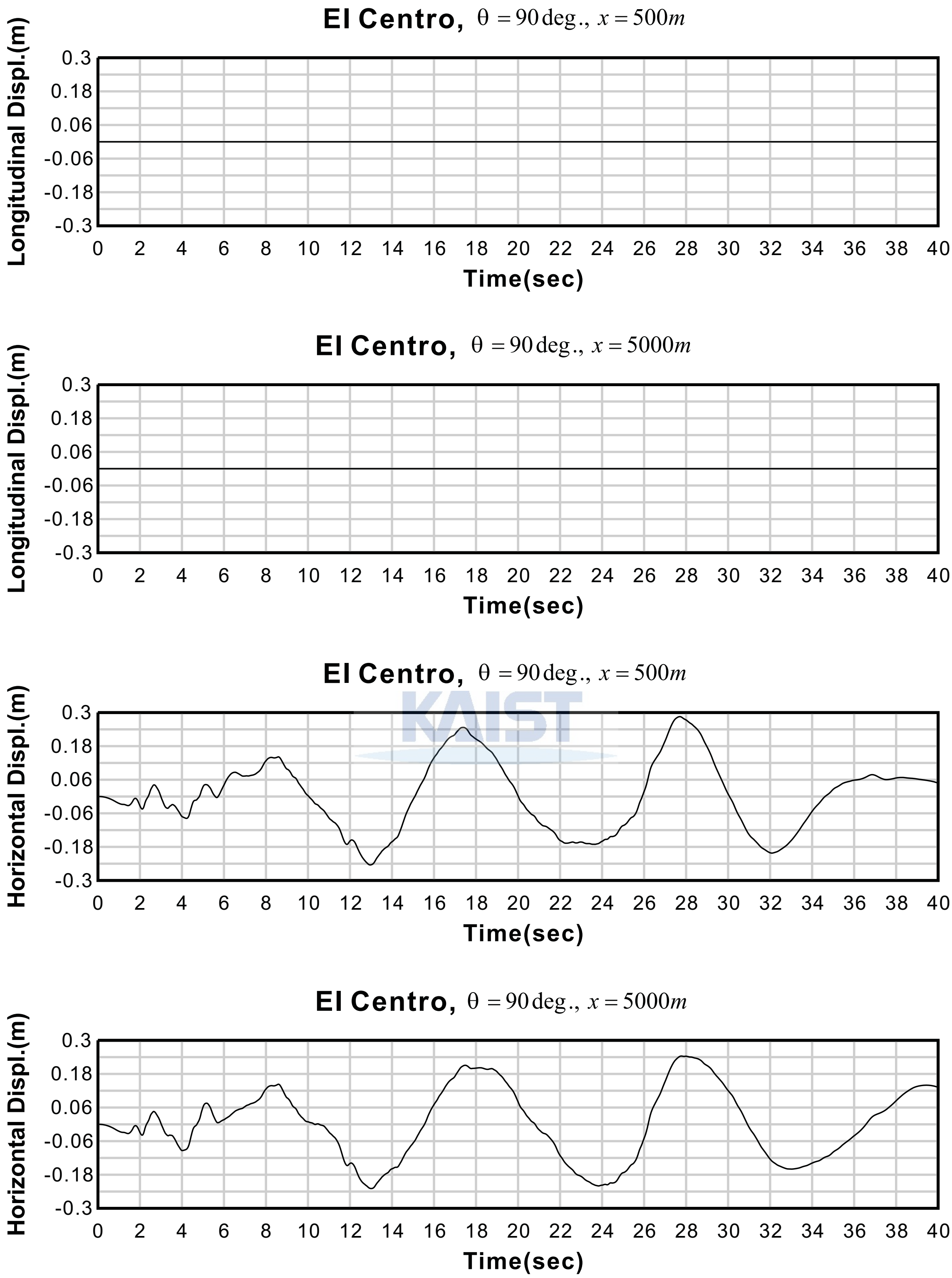

Fig. 36. Displacement response time history for El Centro ground motion, $\theta = 90\,\mathrm{deg.}$

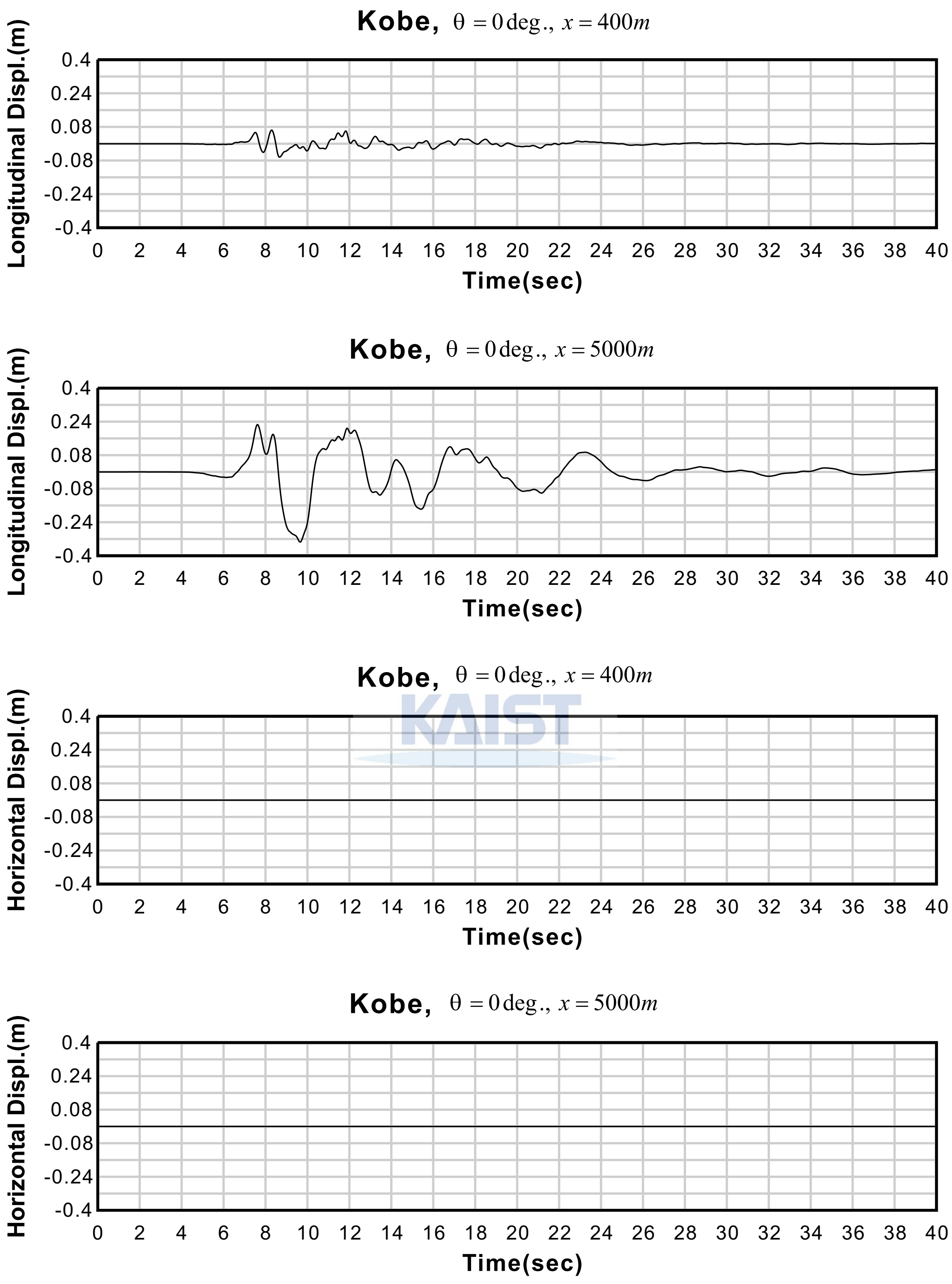

Fig. 37. Displacement response time history for Kobe ground motion, $\theta = 0\,\mathrm{deg}$.

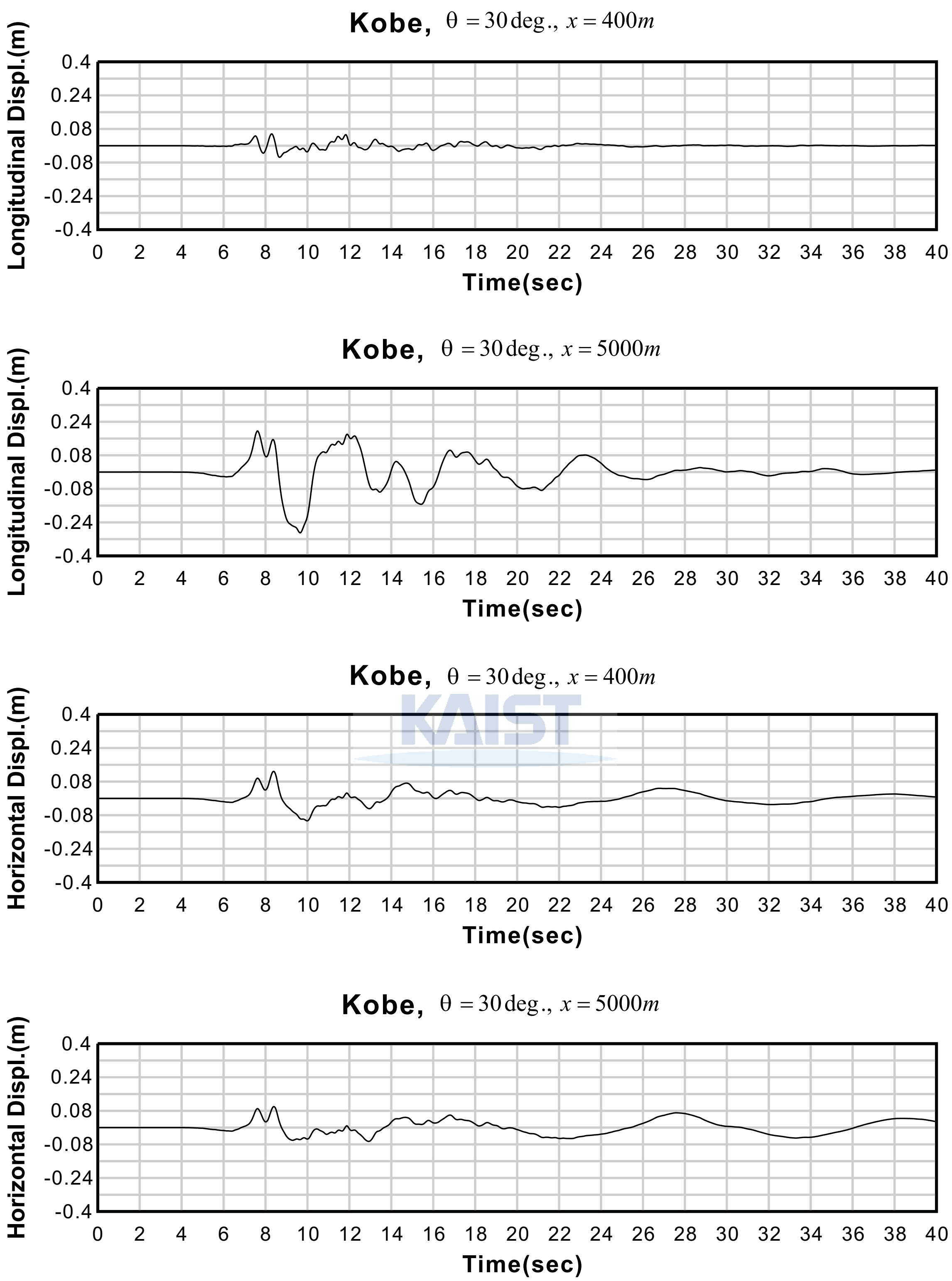

Fig. 38. Displacement response time history for Kobe ground motion, $\theta = 30\,\mathrm{deg}.$

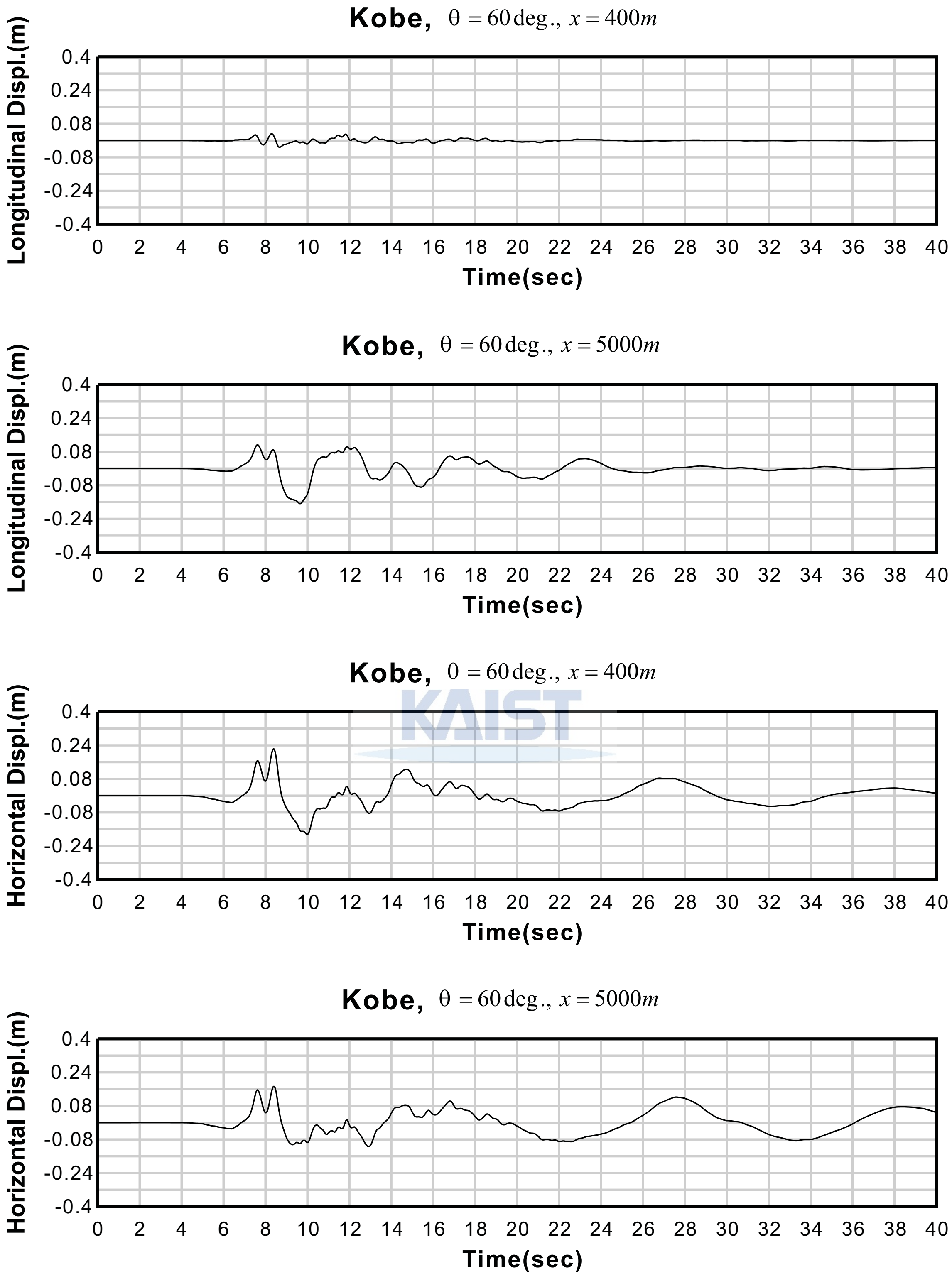

Fig. 39. Displacement response time history for Kobe ground motion, $\theta = 60\deg.$

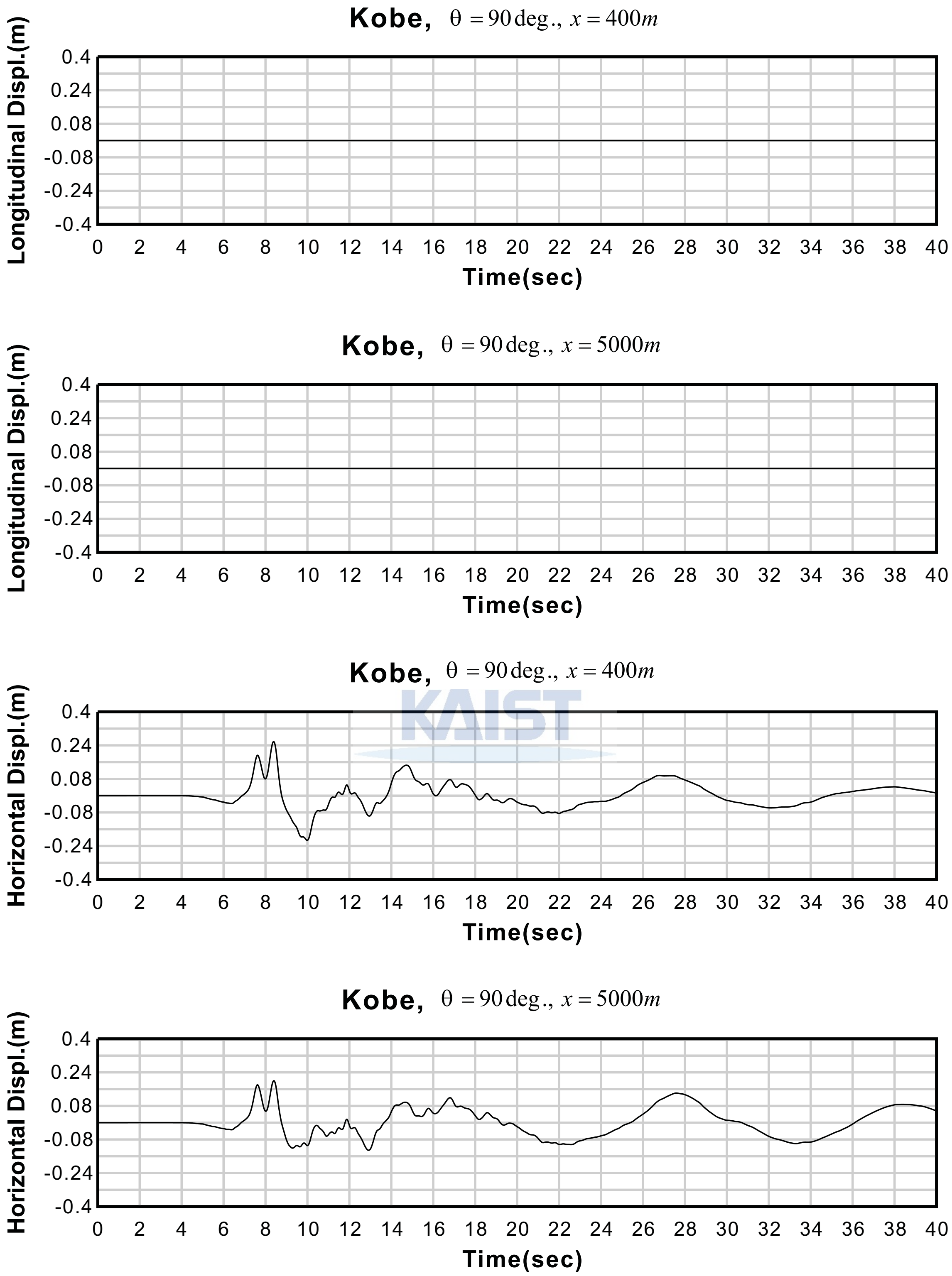

Fig. 40. Displacement response time history for Kobe ground motion, $\theta = 90\deg.$

4.4.3.2 Velocity responses time history

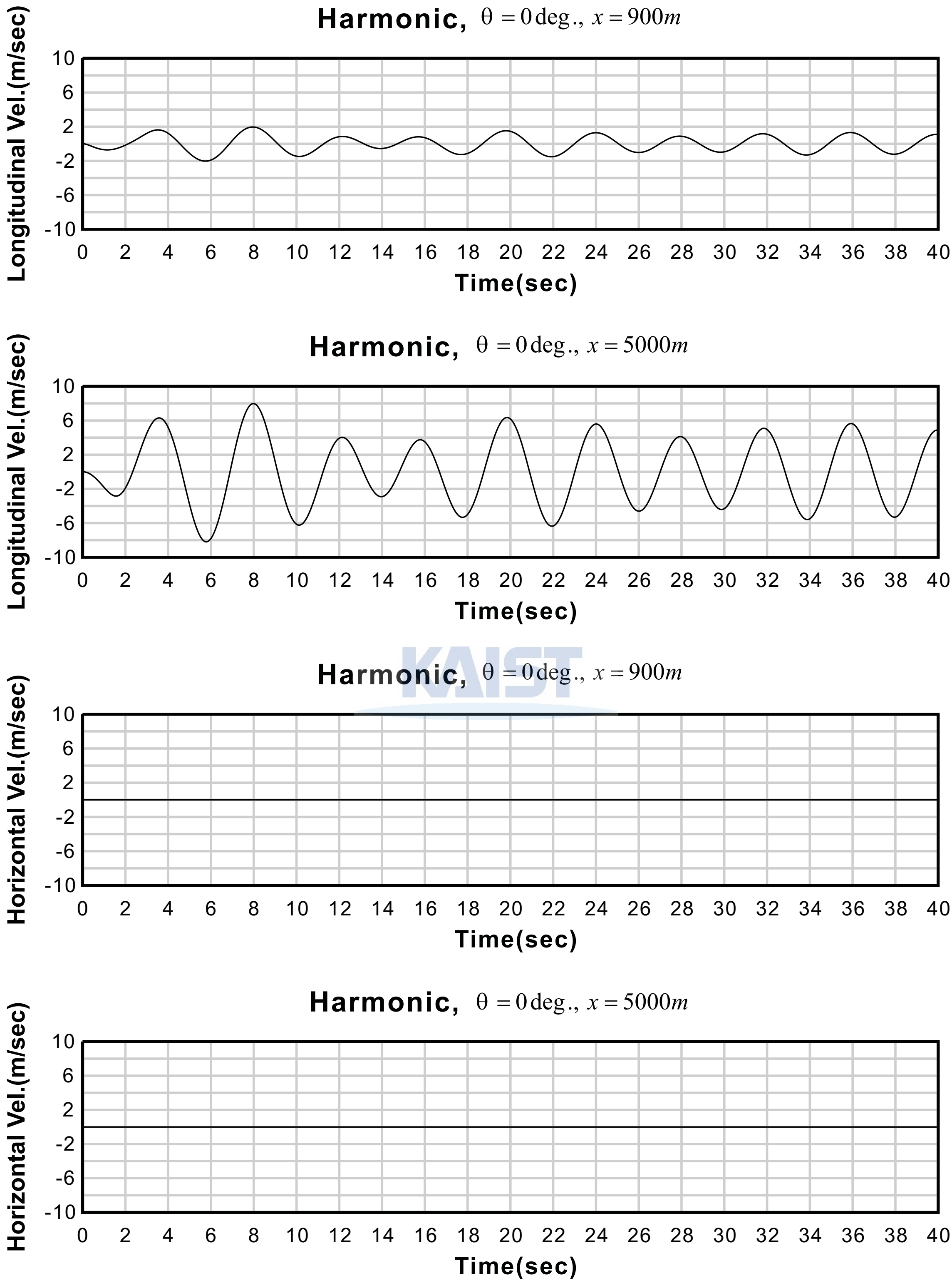

Fig. 41. Velocity response time history for harmonic ground motion, $\theta = 0\,\text{deg}.$

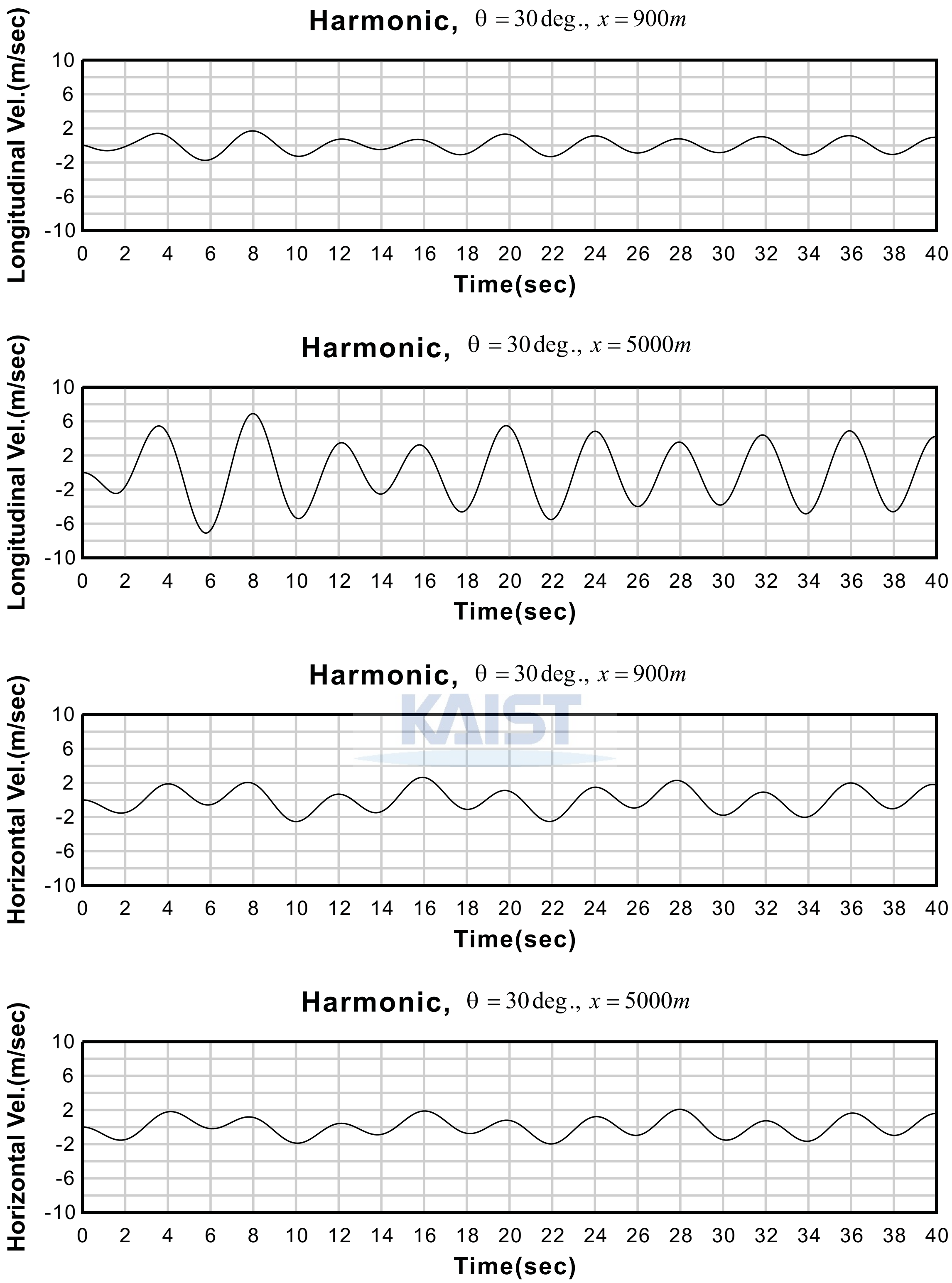

Fig. 42. Velocity response time history for harmonic ground motion, $\theta = 30\,\deg.$

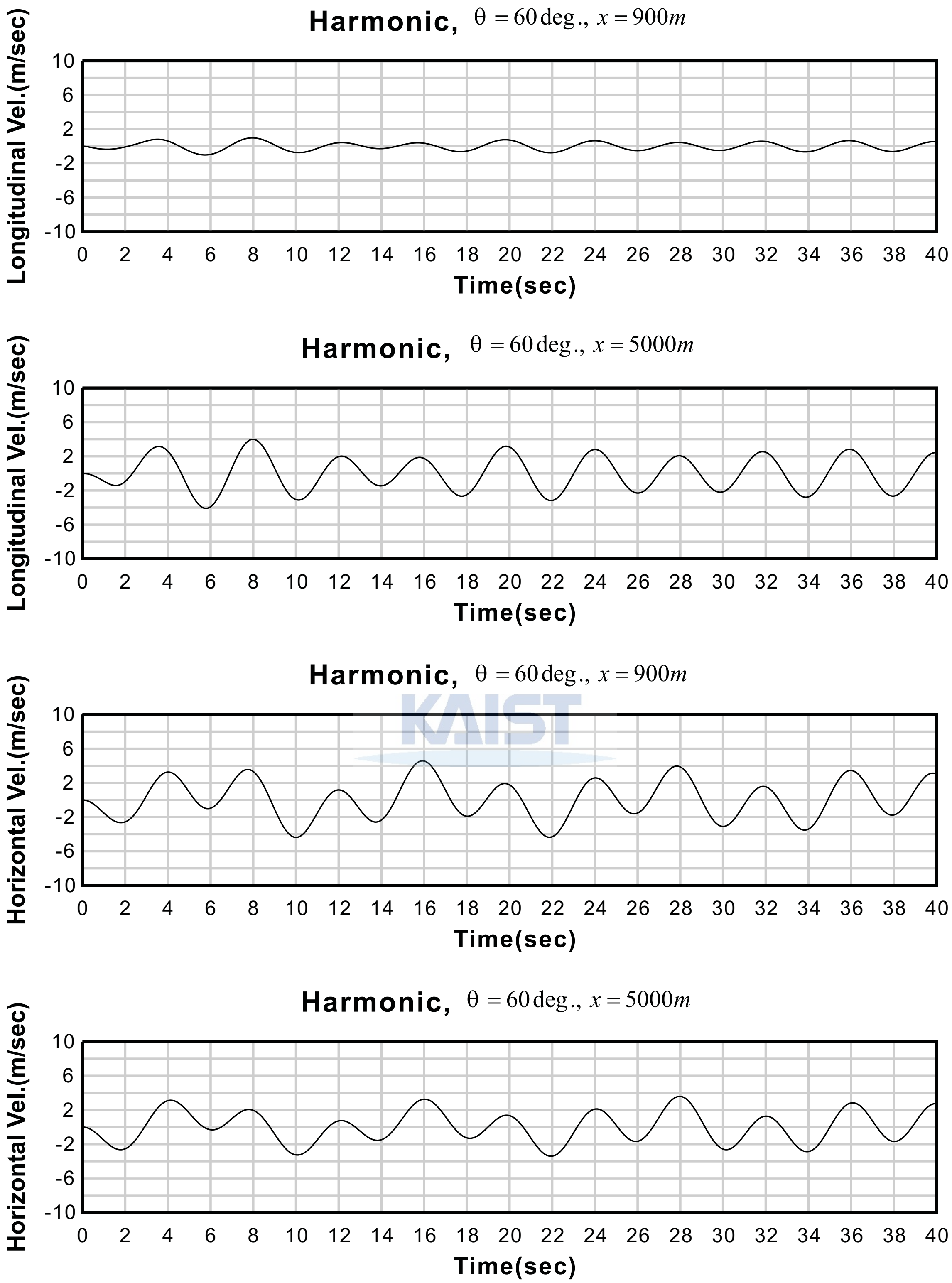

Fig. 43. Velocity response time history for harmonic ground motion, $\theta = 60\,\text{deg}.$

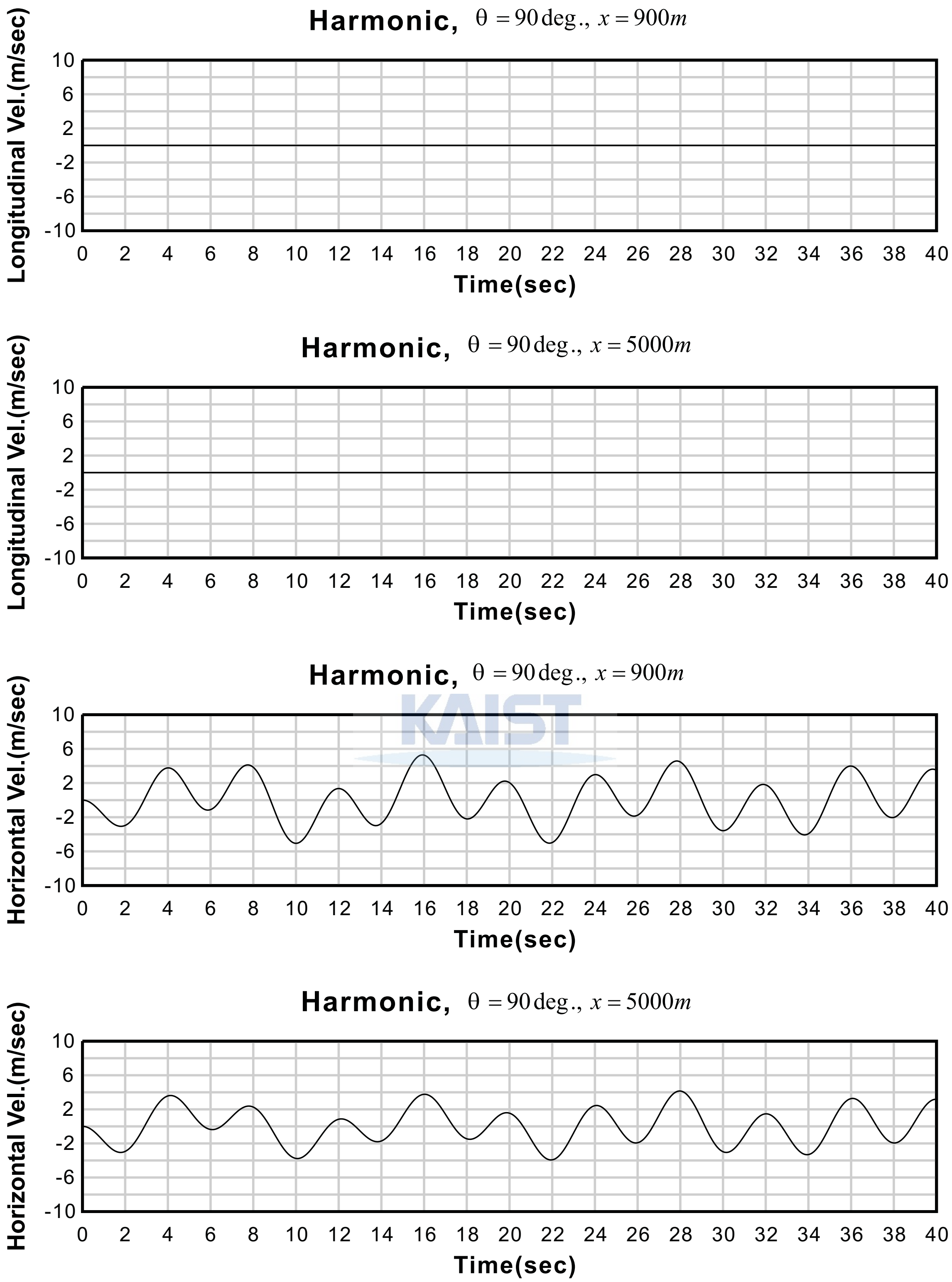

Fig. 44. Velocity response time history for harmonic ground motion, $\theta = 90\,\mathrm{deg}.$

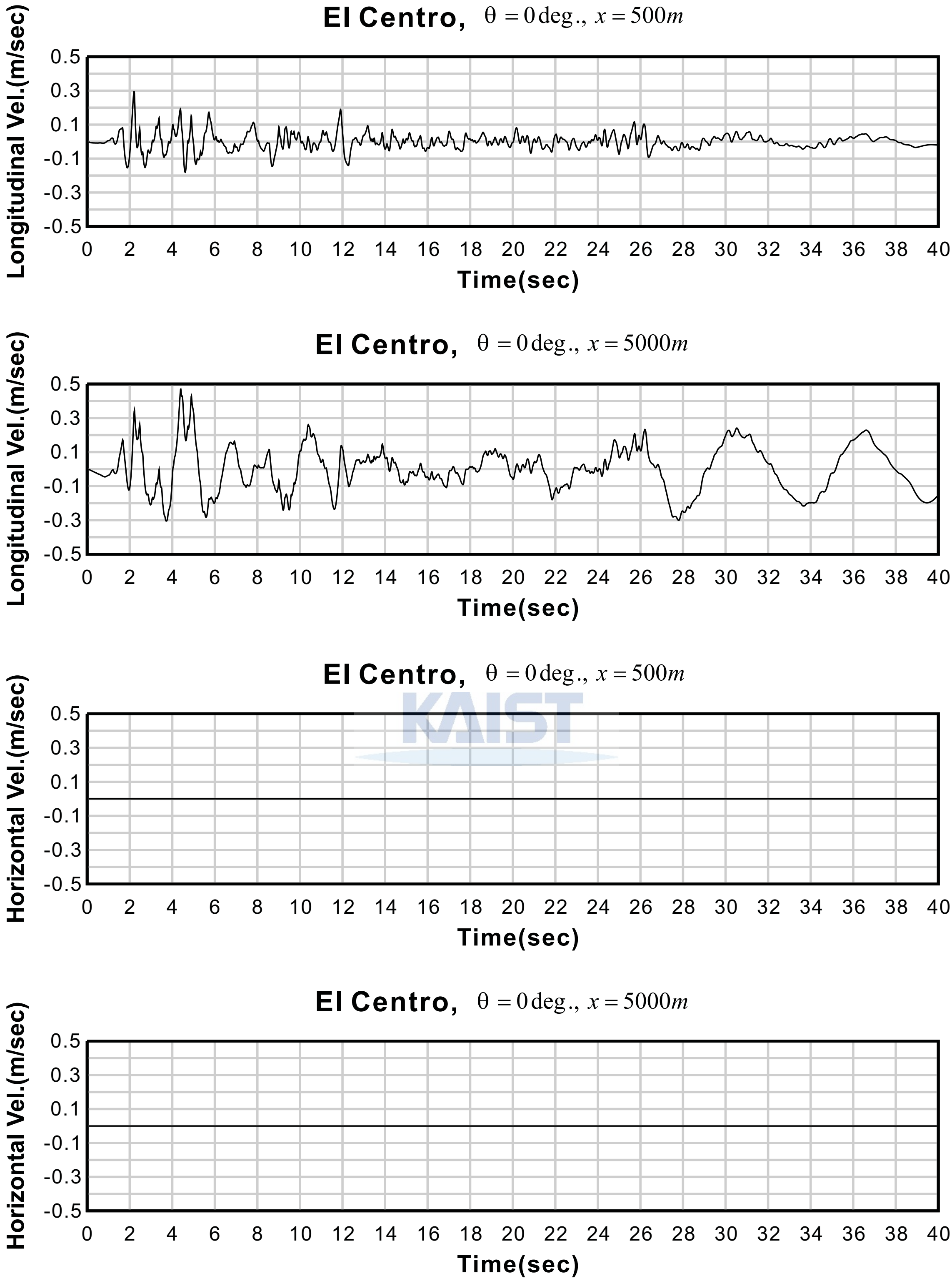

Fig. 45. Velocity response time history for El Centro ground motion, $\theta = 0\,\mathrm{deg.}$

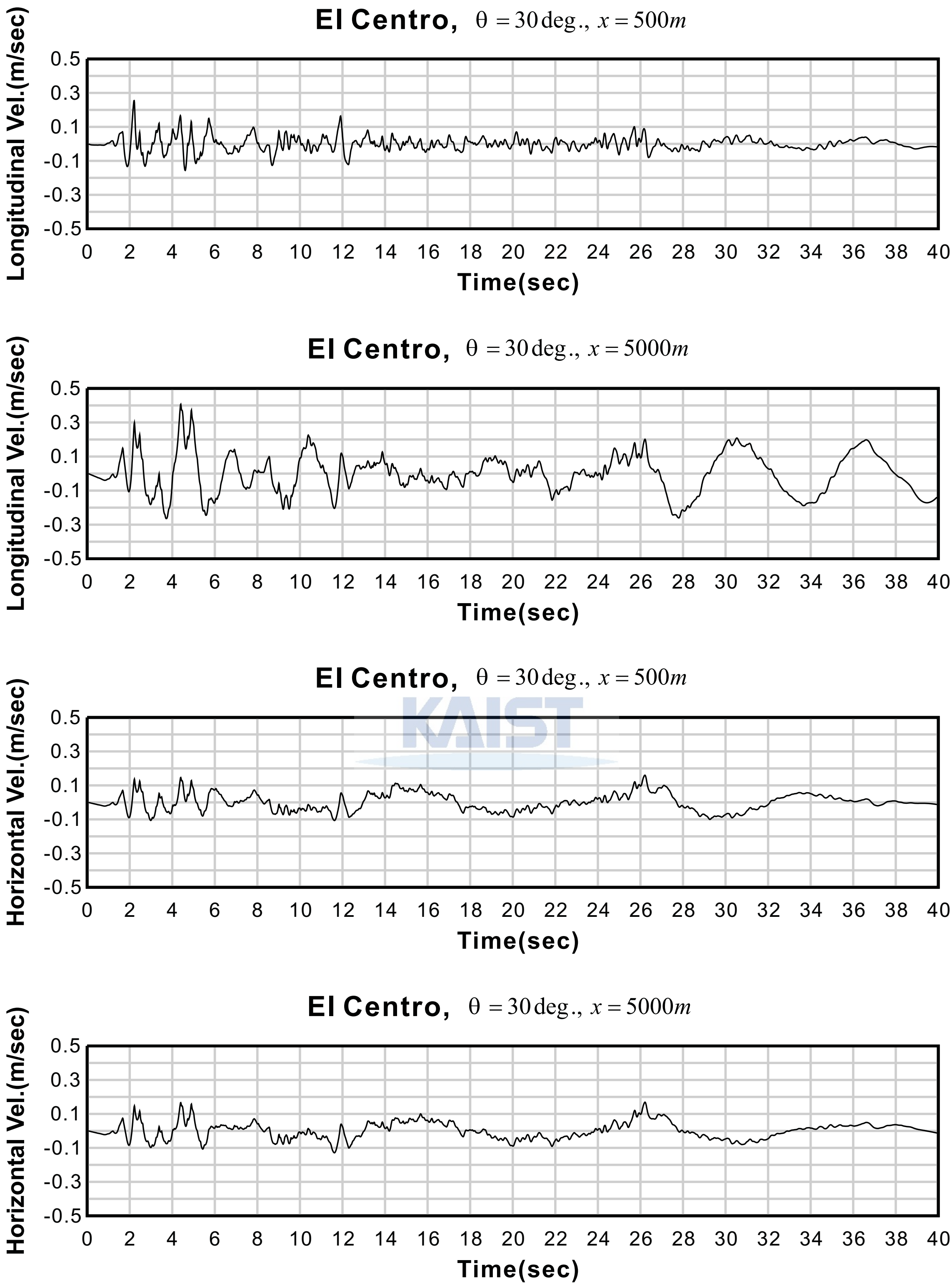

Fig. 46. Velocity response time history for El Centro ground motion, $\theta = 30\,\deg.$

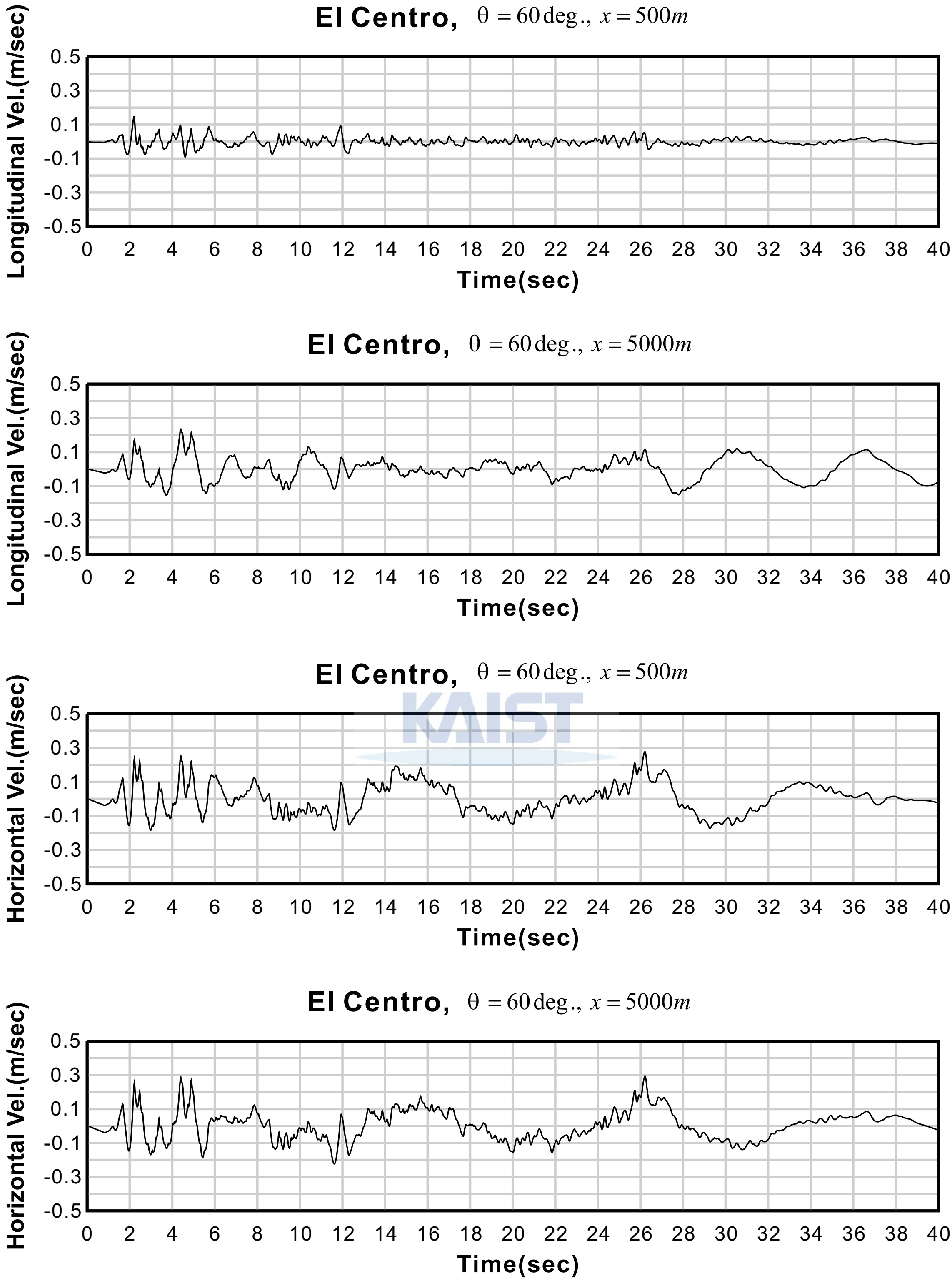

Fig. 47. Velocity response time history for El Centro ground motion, $\theta = 60\,\mathrm{deg.}$

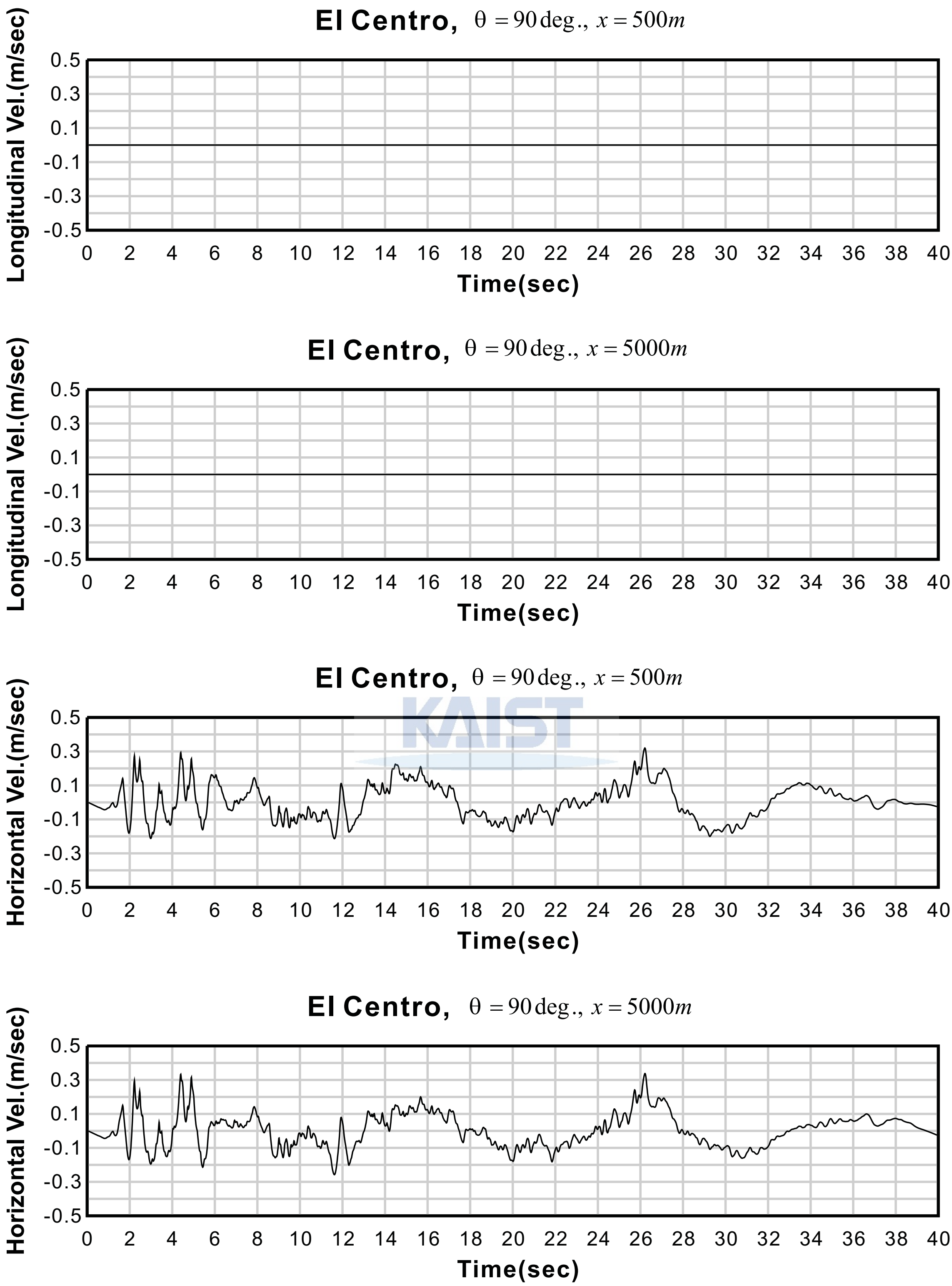

Fig. 48. Velocity response time history for El Centro ground motion, $\theta = 90\,\deg.$

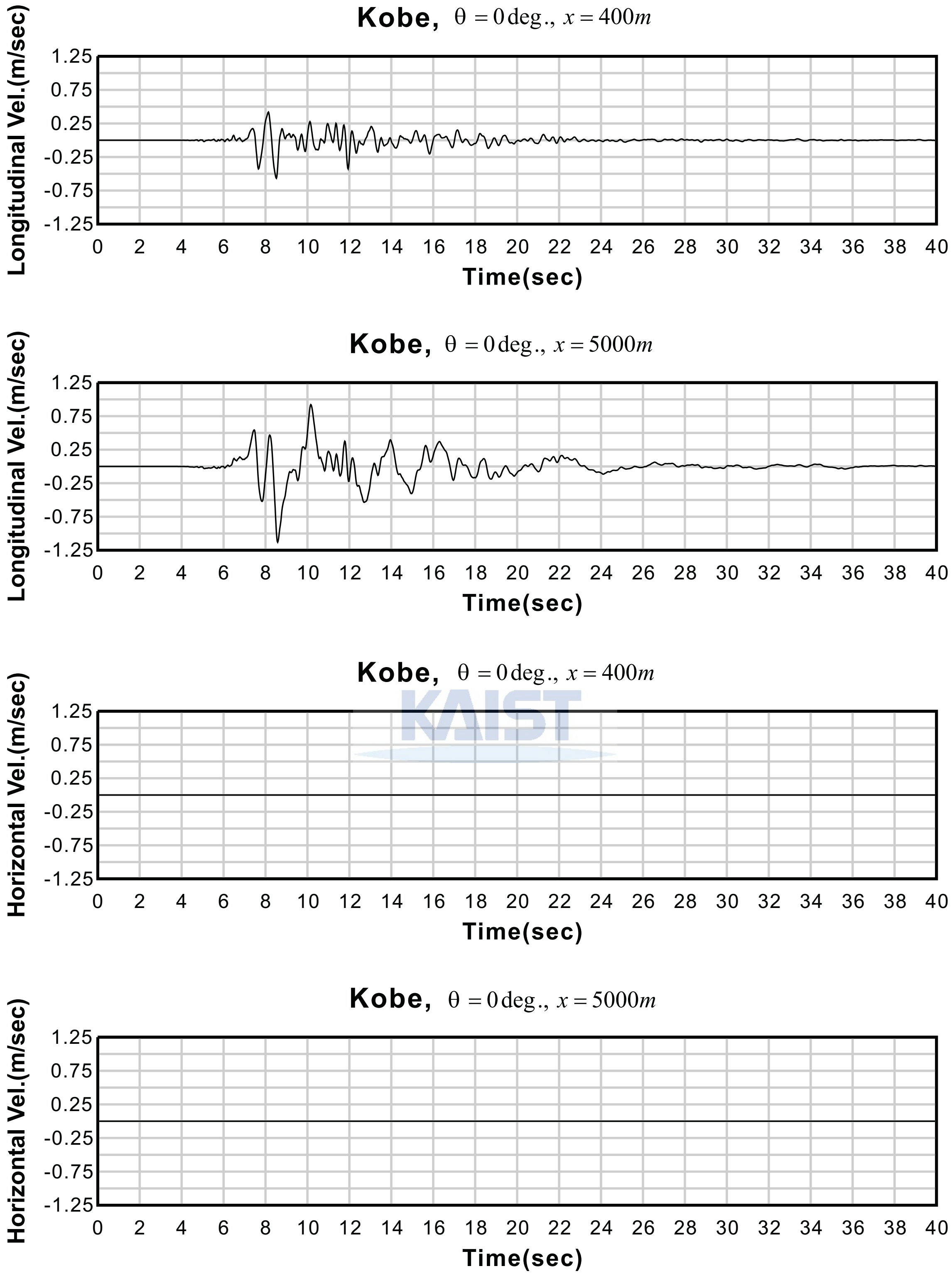

Fig. 49. Velocity response time history for Kobe ground motion, $\theta = 0\,\mathrm{deg}$.

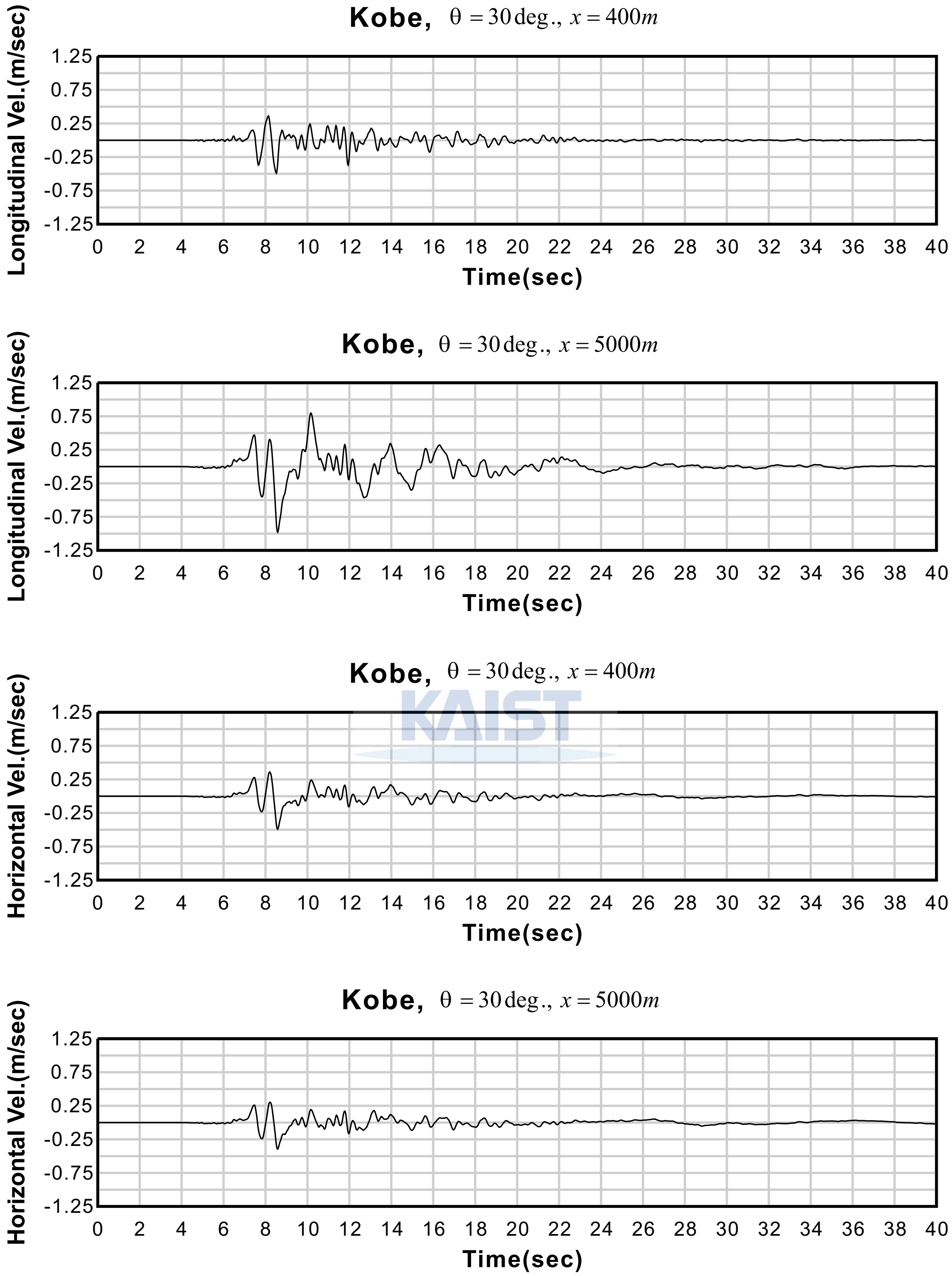

Fig. 50. Velocity response time history for Kobe ground motion, $\theta = 30\deg.$

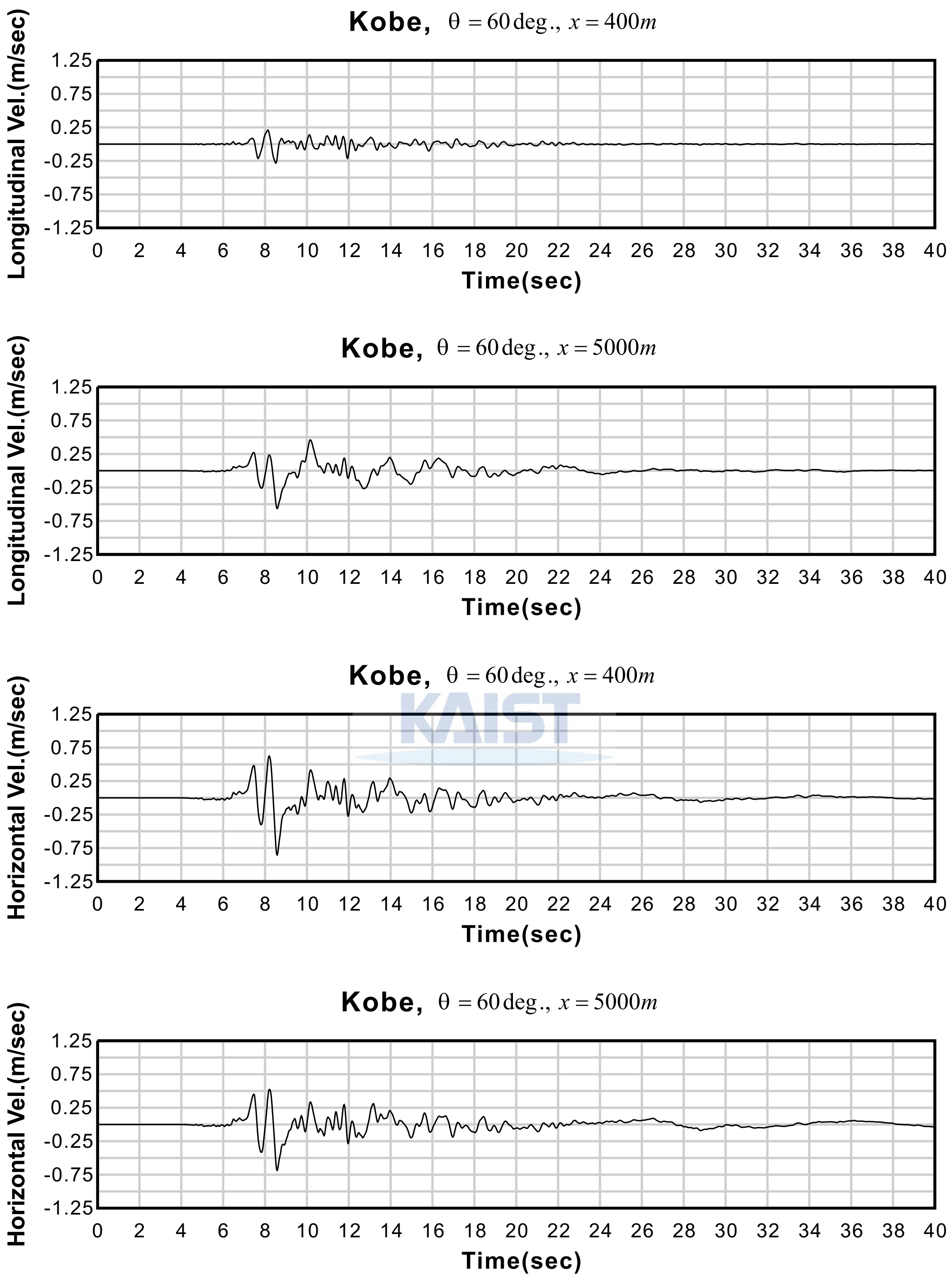

Fig. 51. Velocity response time history for Kobe ground motion, $\theta = 60\,\mathrm{deg}.$

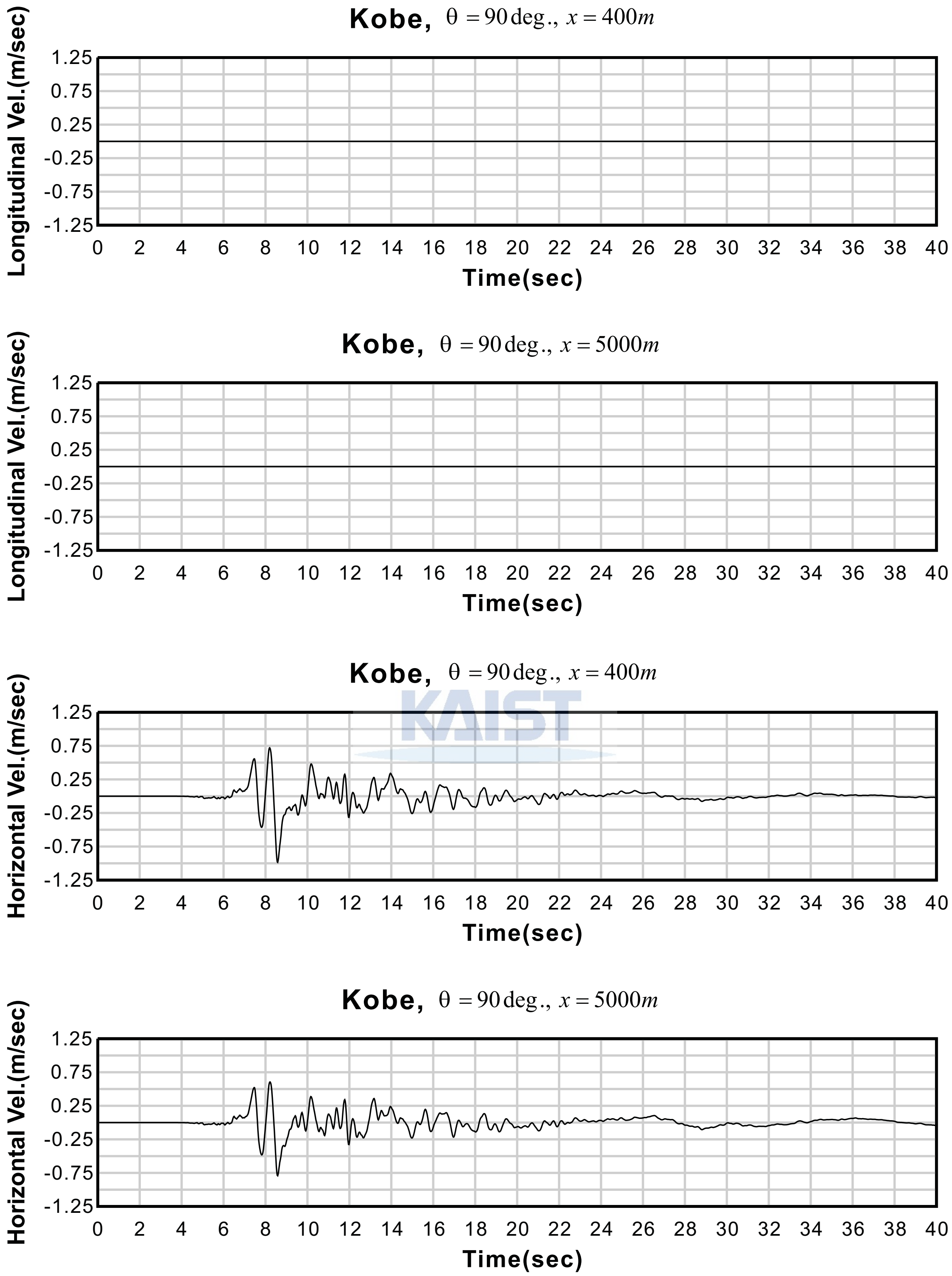

Fig. 52. Velocity response time history for Kobe ground motion, $\theta = 90\,\mathrm{deg}.$

4.4.3.3 Acceleration responses time history

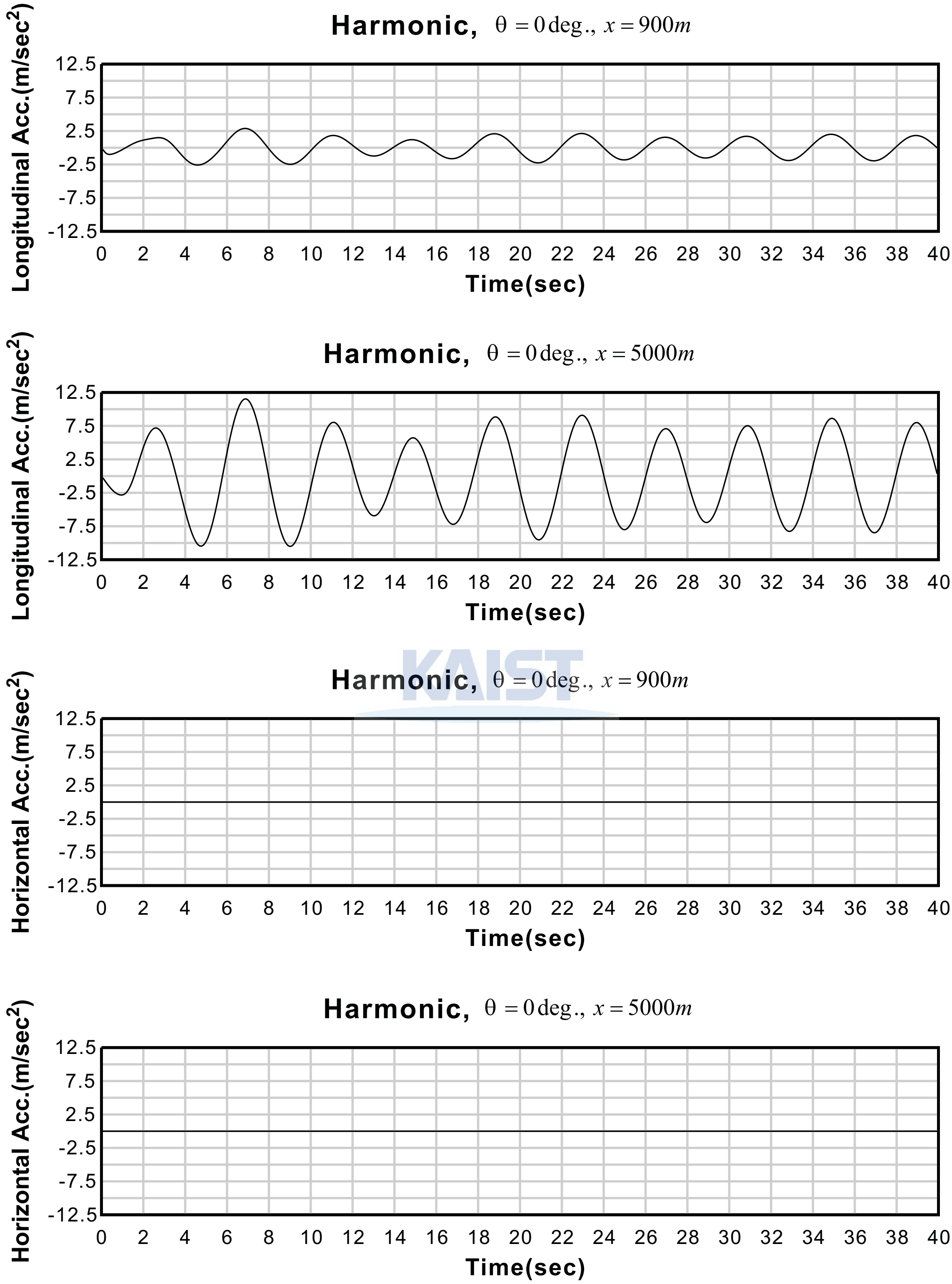

Fig. 53. Acceleration response time history for harmonic ground motion, $\theta = 0\,\text{deg.}$

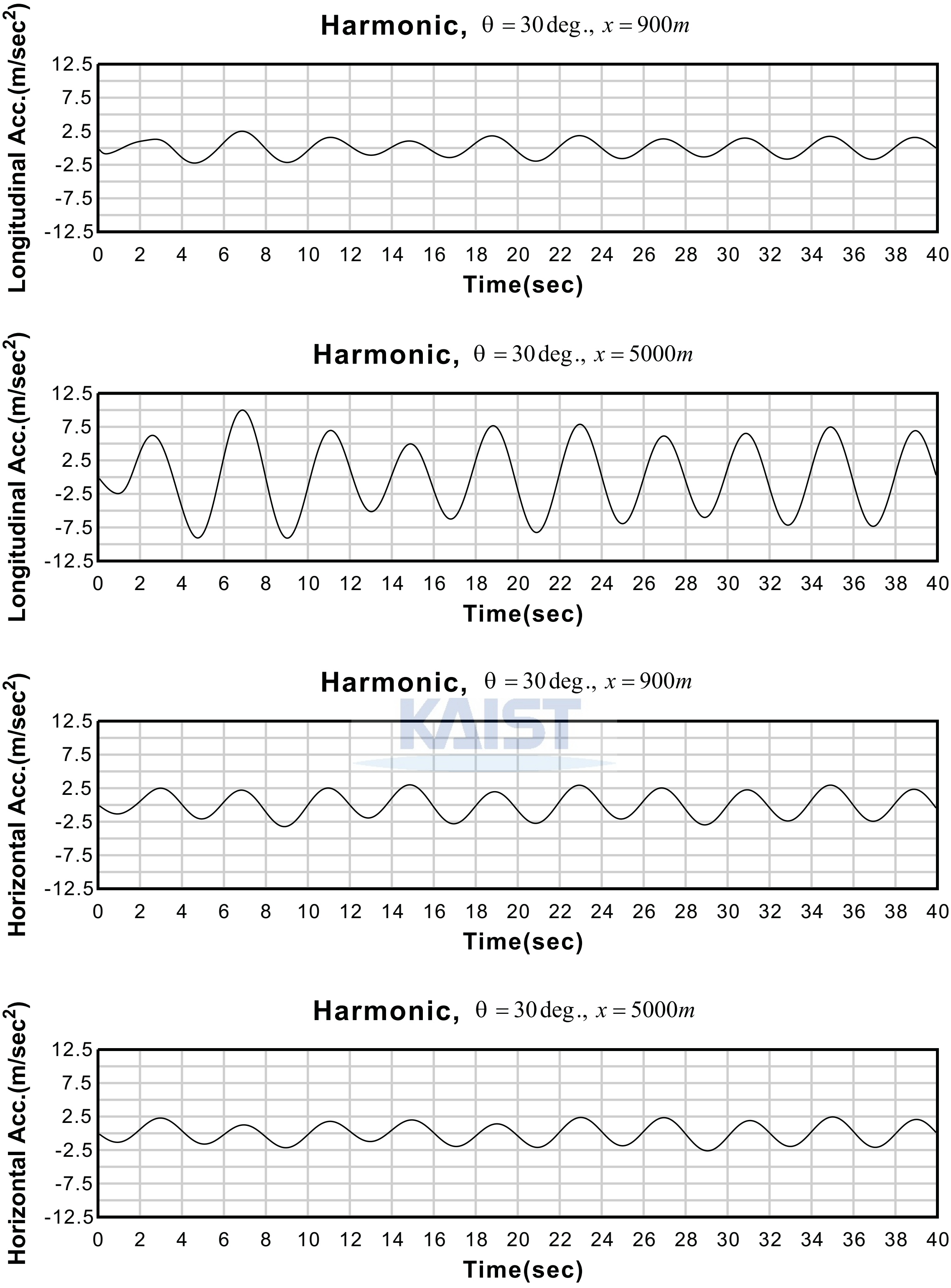

Fig. 54. Acceleration response time history for harmonic ground motion, $\theta = 30\deg.$

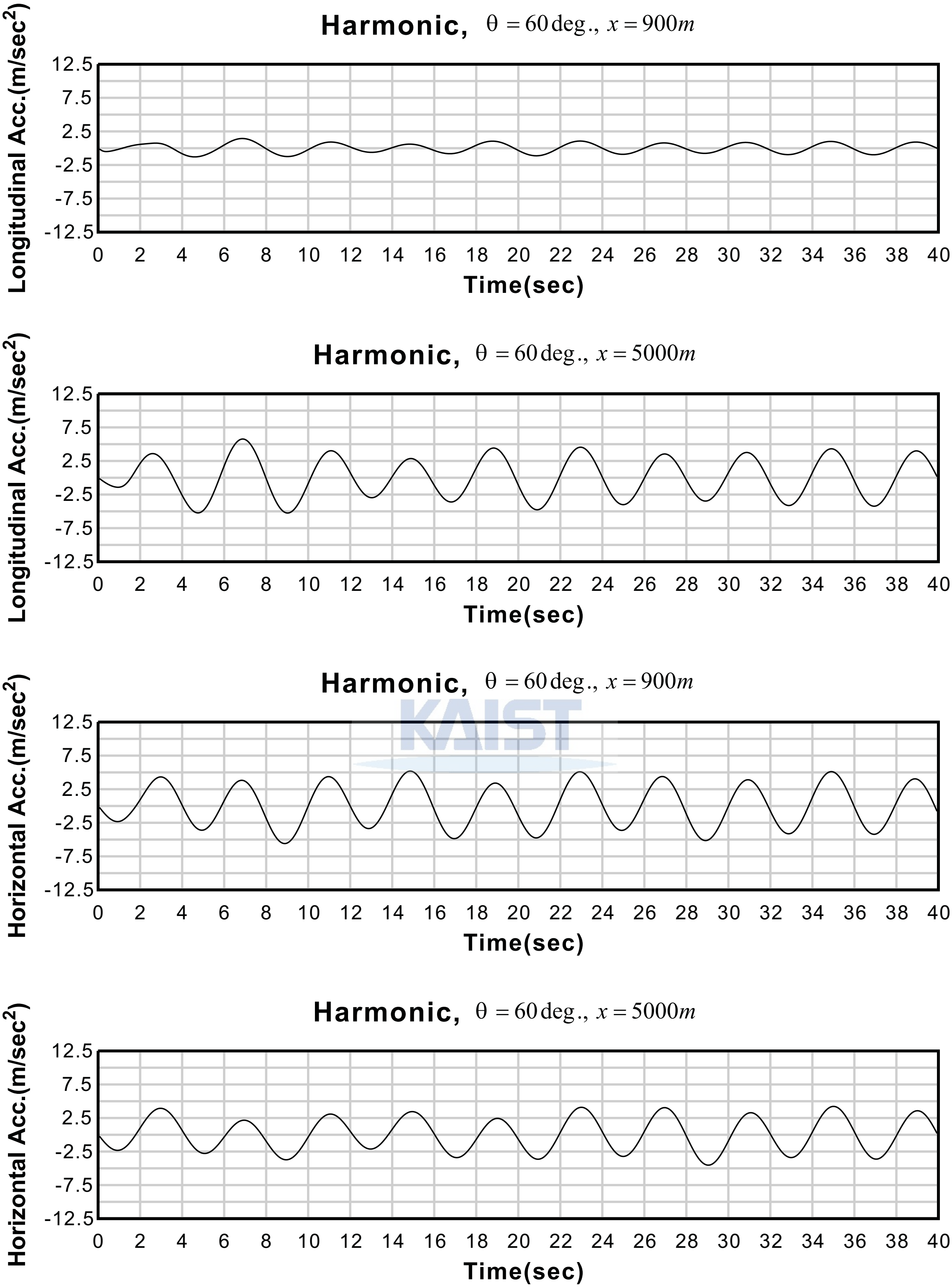

Fig. 55. Acceleration response time history for harmonic ground motion, $\theta = 60\,\mathrm{deg}$.

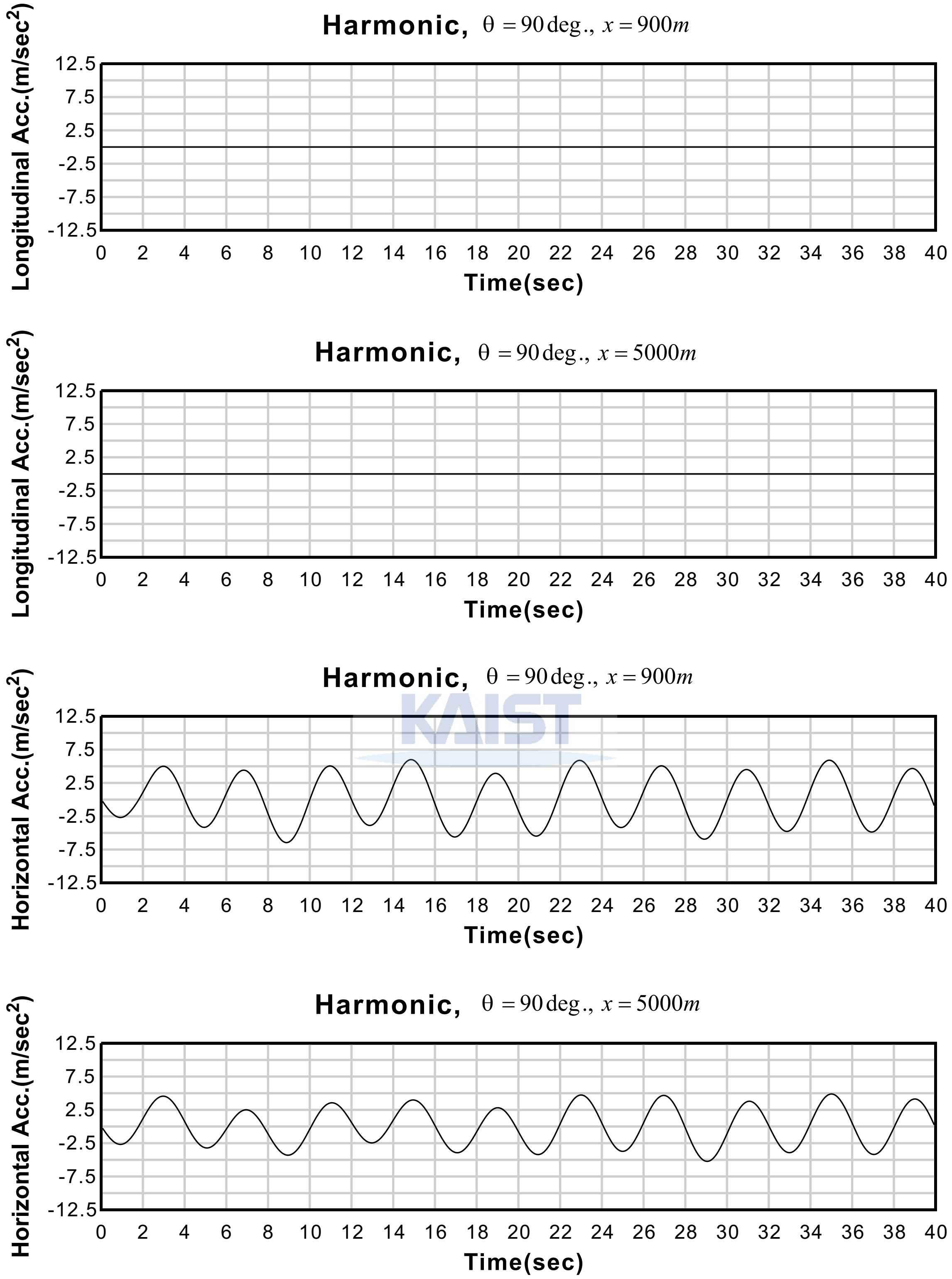

Fig. 56. Acceleration response time history for harmonic ground motion, $\theta = 90\,\deg.$

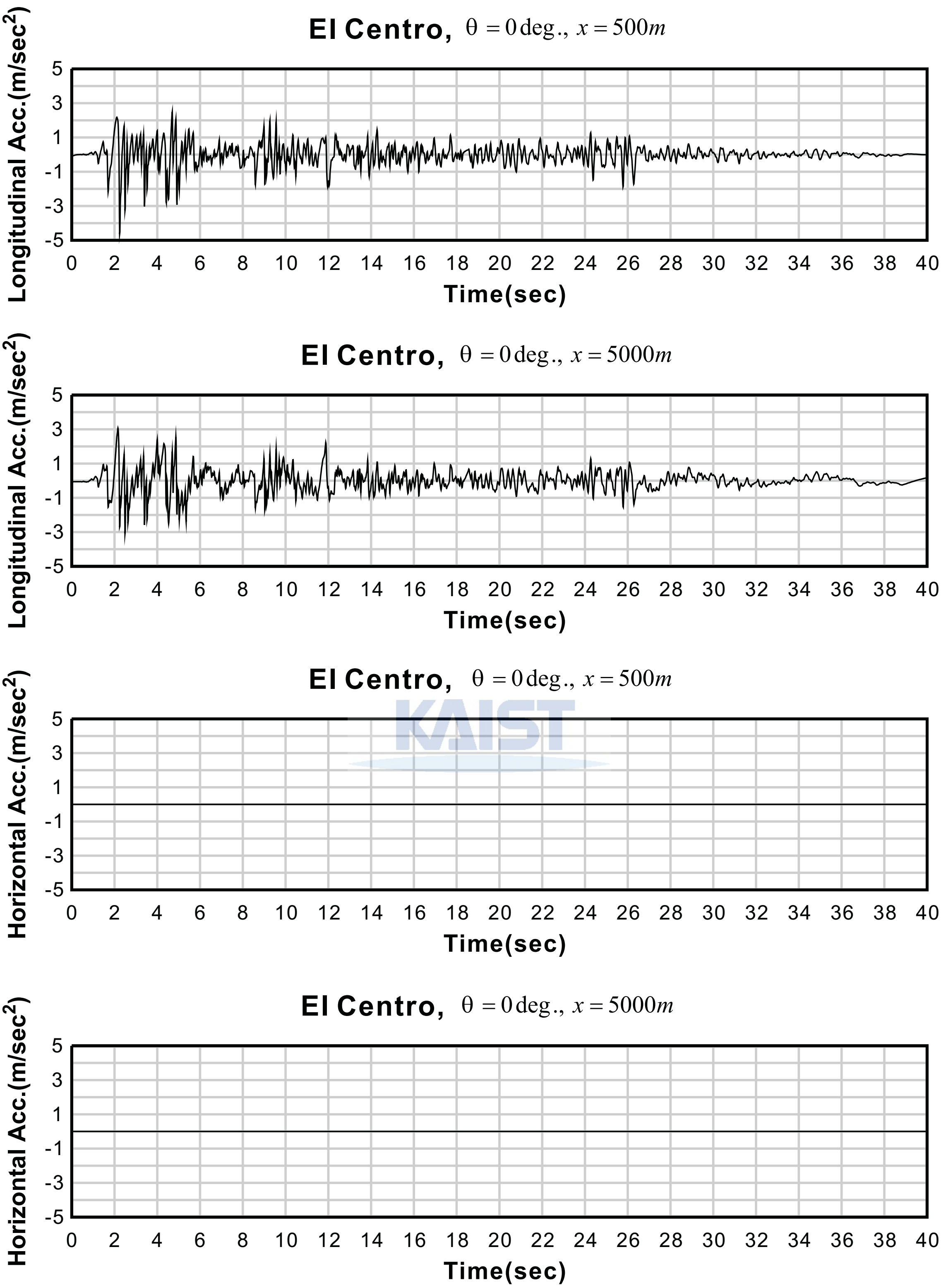

Fig. 57. Acceleration response time history for El Centro ground motion, $\theta = 0\,\text{deg.}$

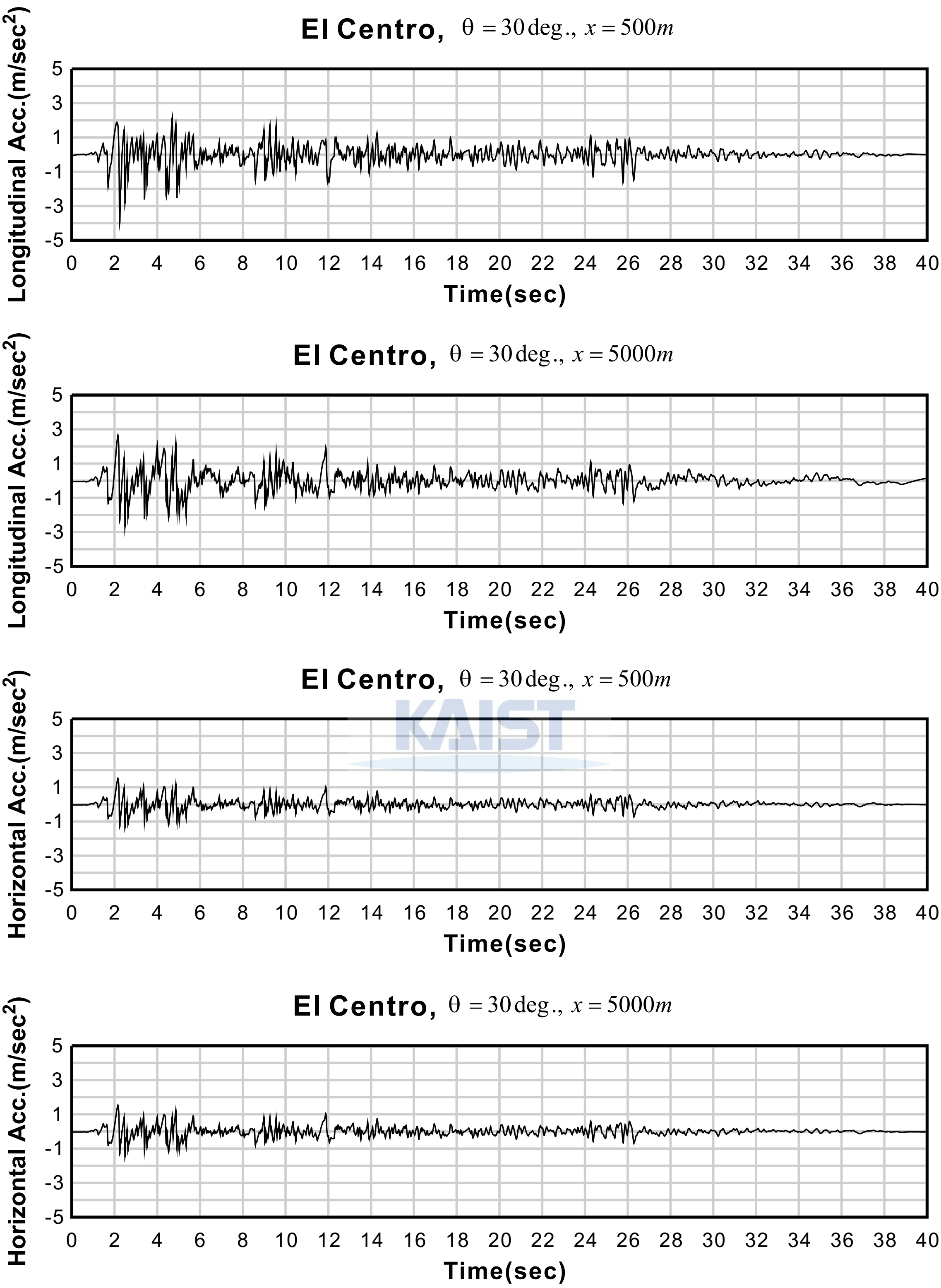

Fig. 58. Acceleration response time history for El Centro ground motion, $\theta = 30\,\mathrm{deg}.$

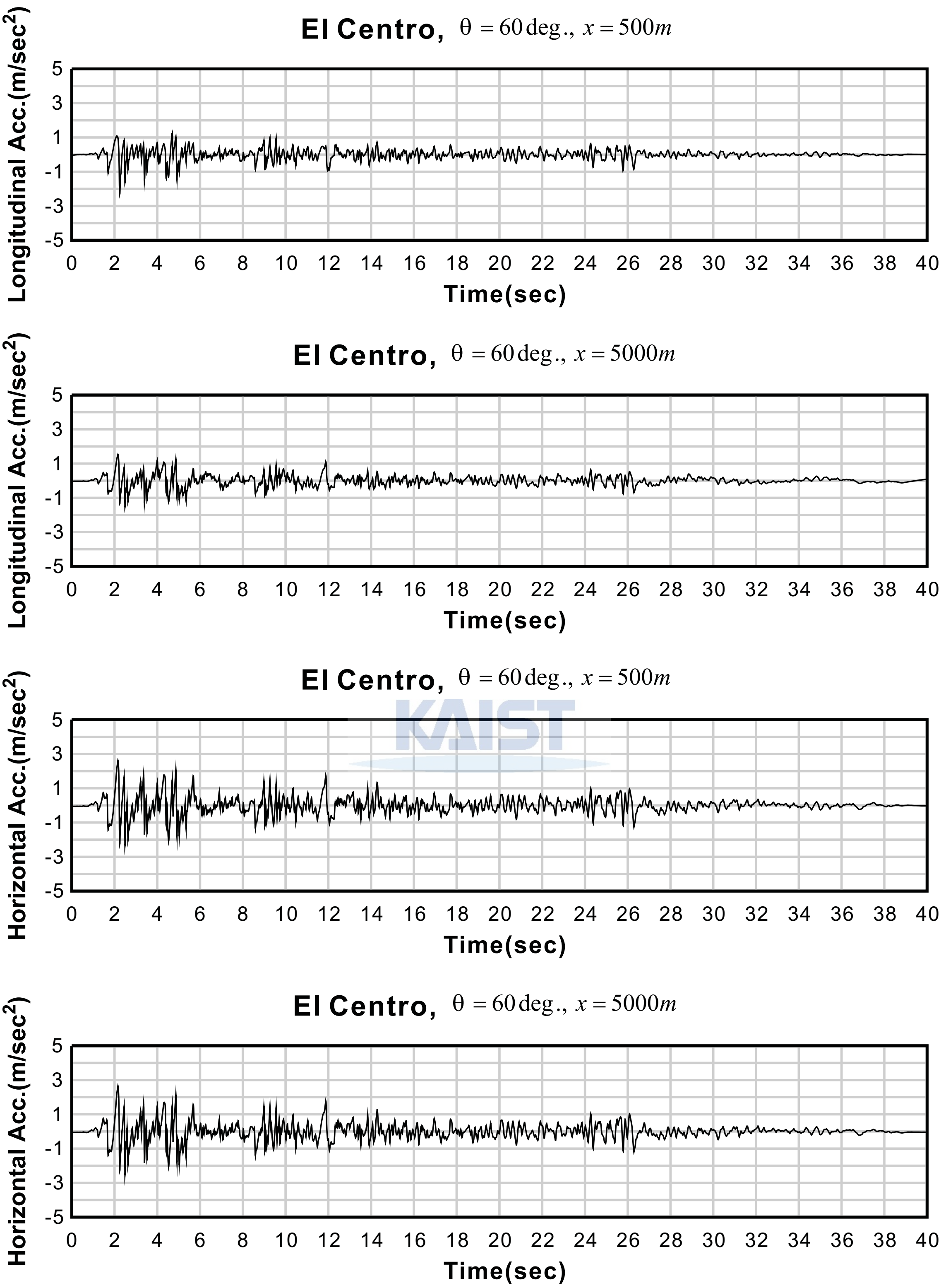

Fig. 59. Acceleration response time history for El Centro ground motion, $\theta = 60\,\text{deg.}$

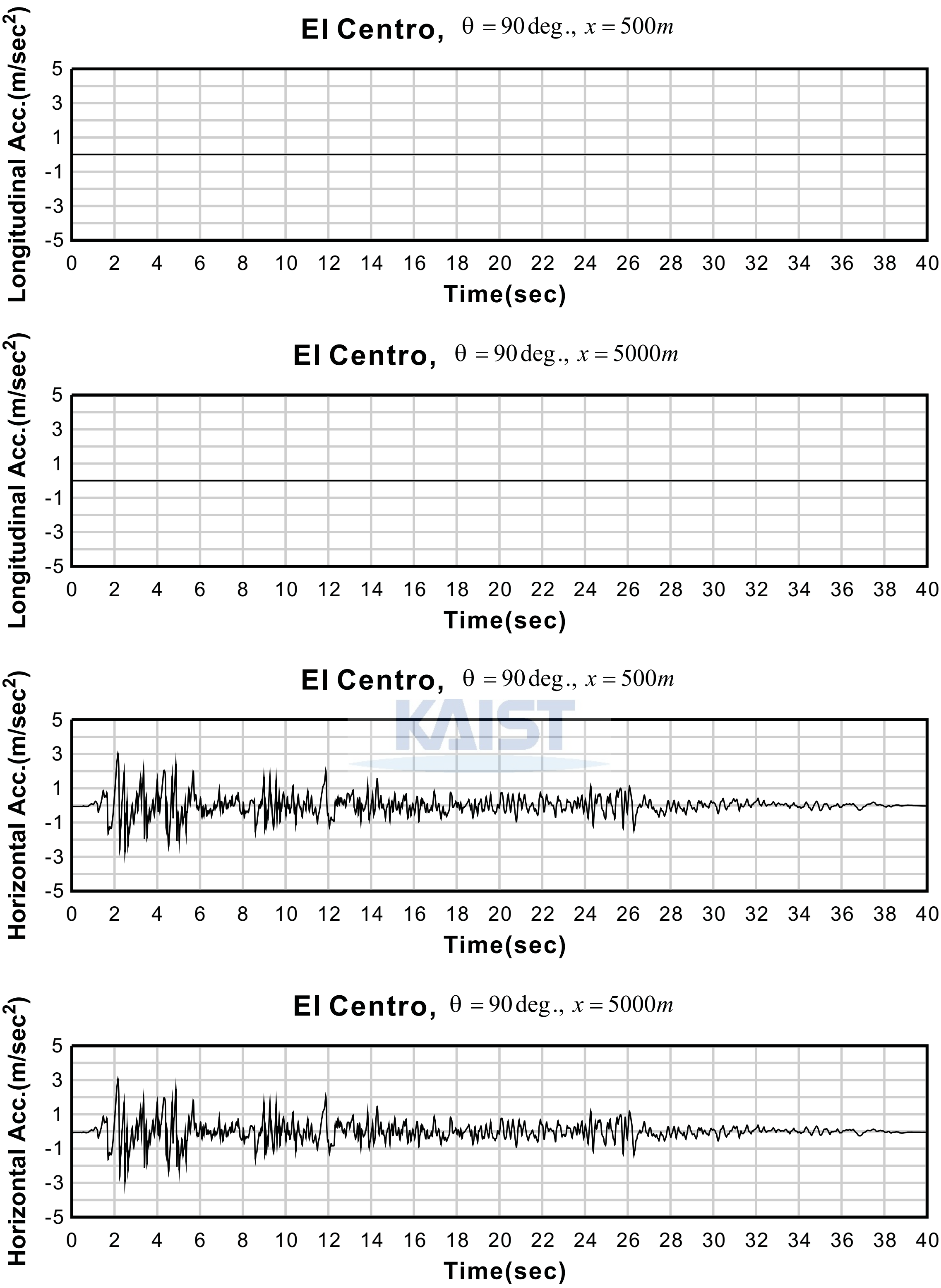

Fig. 60. Acceleration response time history for El Centro ground motion, $\theta = 90\deg.$

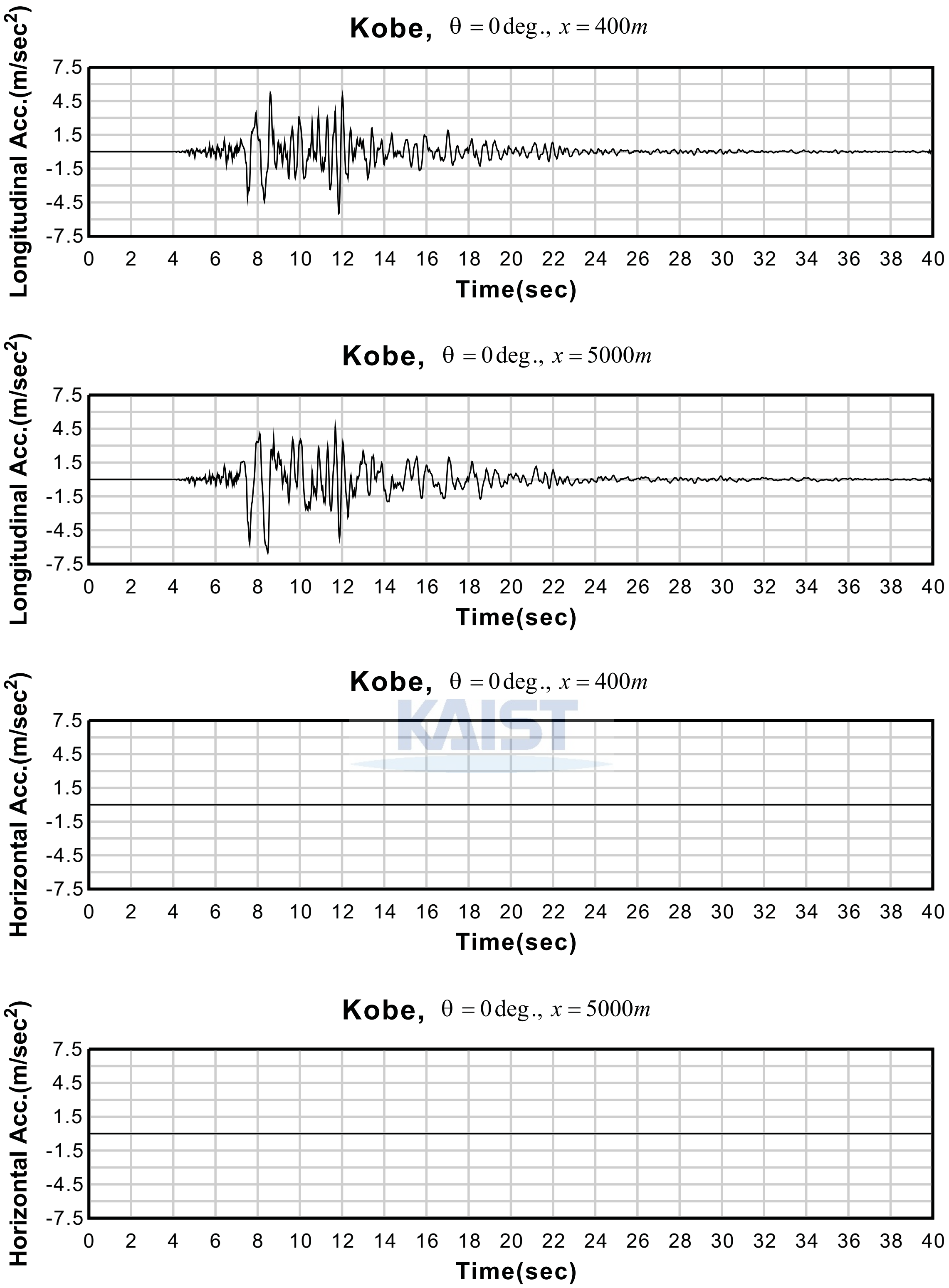

Fig. 61. Acceleration response time history for Kobe ground motion, $\theta = 0\,\mathrm{deg.}$

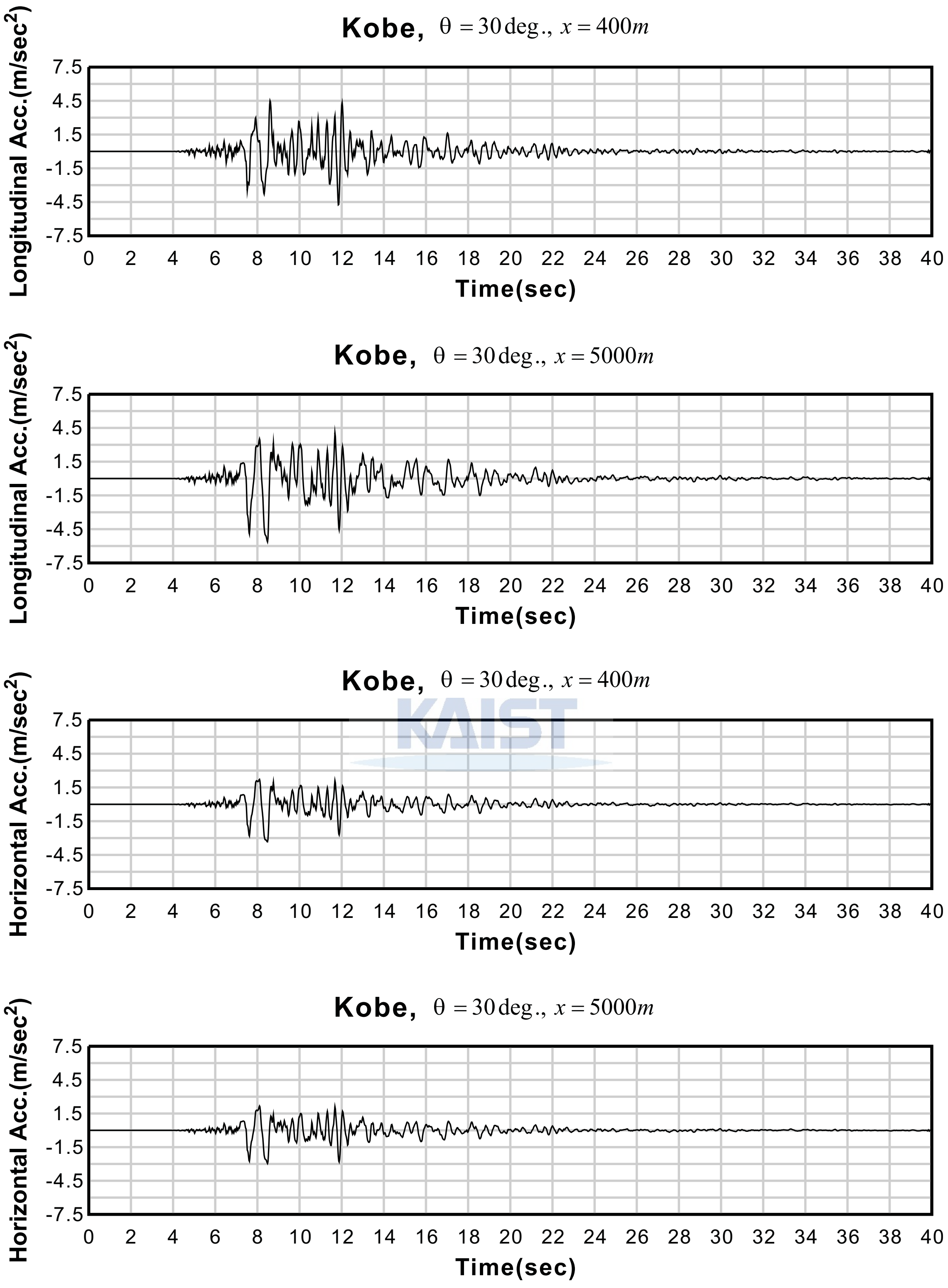

Fig. 62. Acceleration response time history for Kobe ground motion, $\theta = 30\,\mathrm{deg}.$

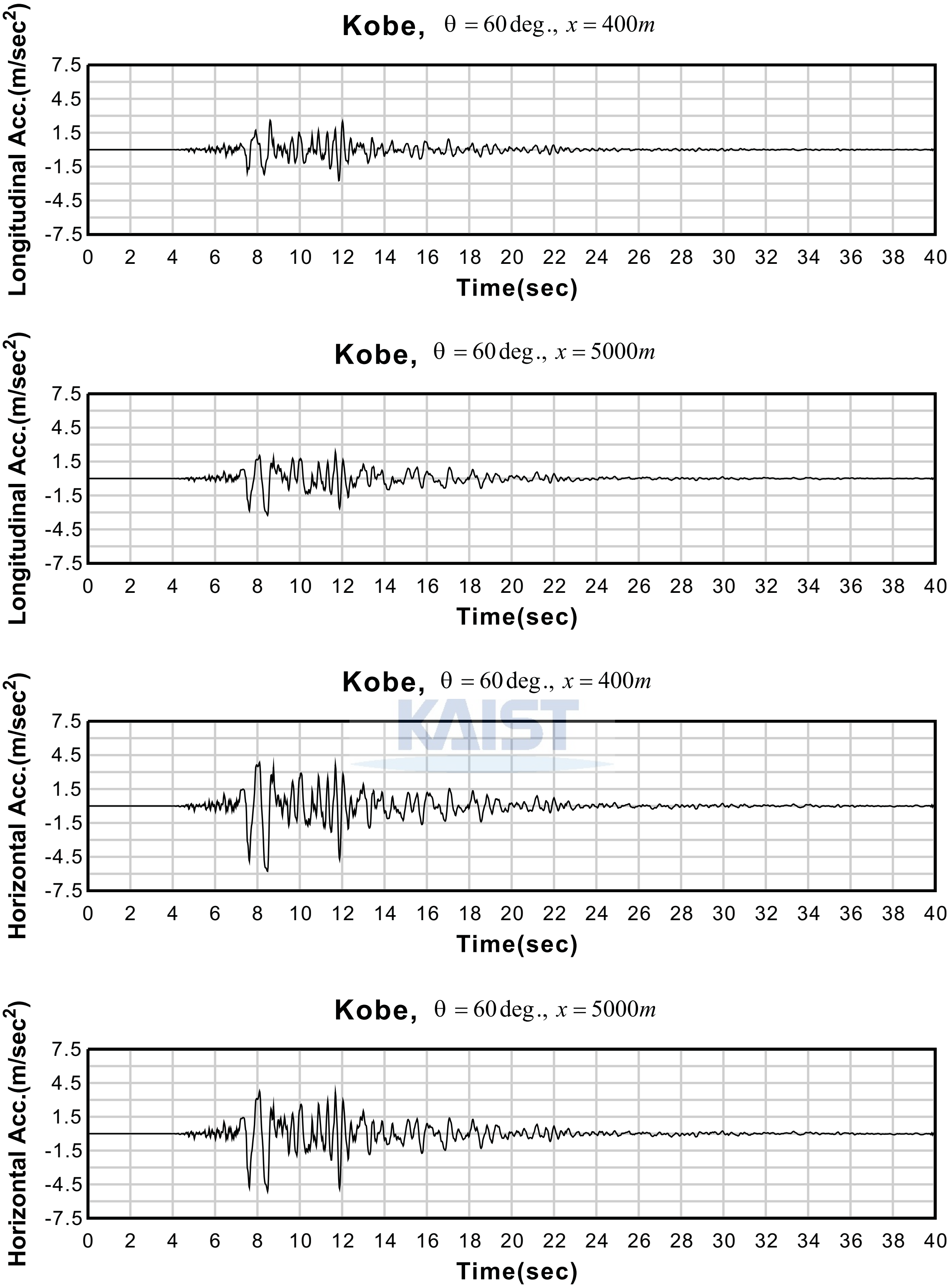

Fig. 63. Acceleration response time history for Kobe ground motion, $\theta = 60\,\mathrm{deg}.$

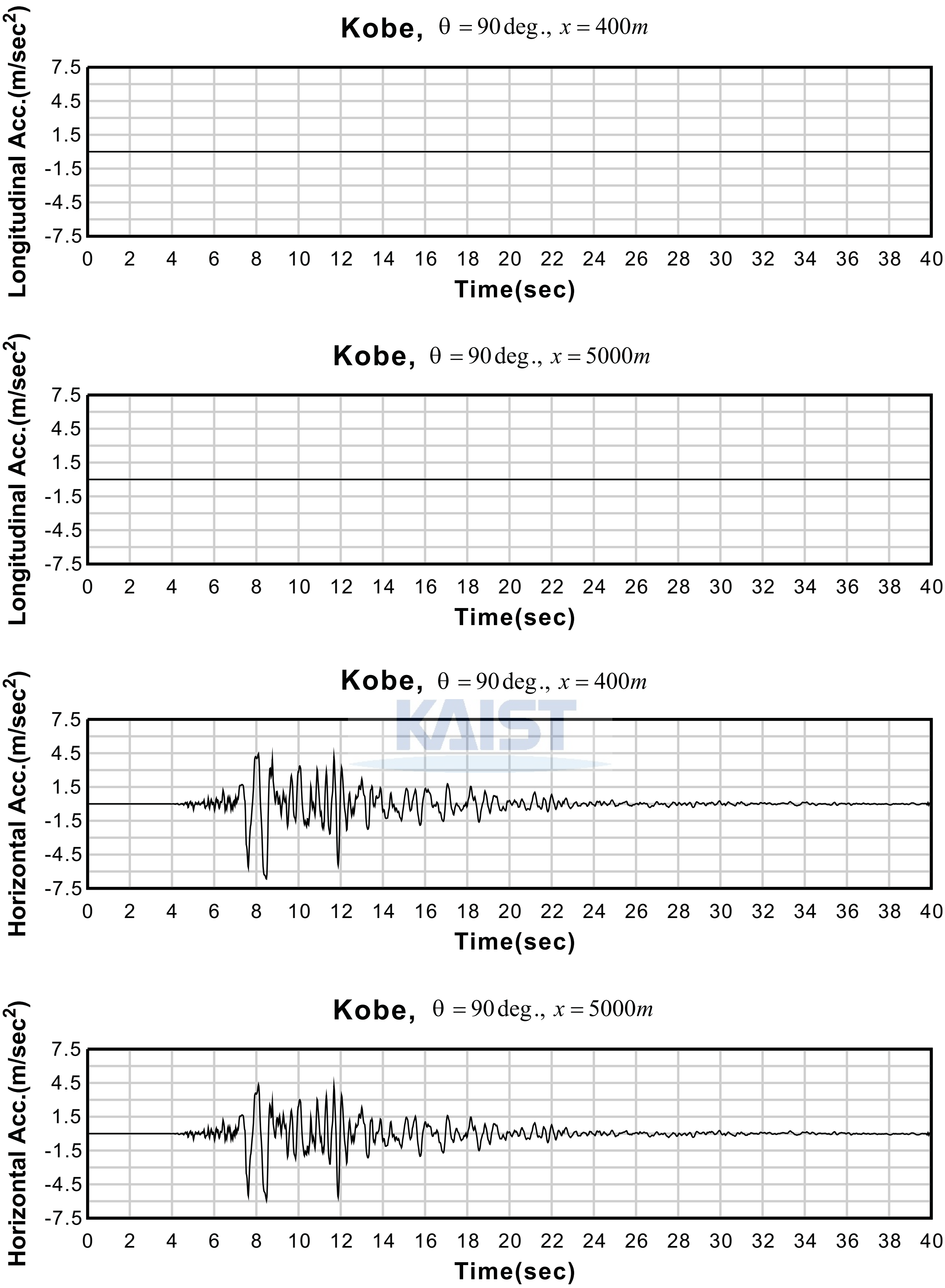

Fig. 64. Acceleration response time history for Kobe ground motion, $\theta = 90\,\deg$.

4.5 Maximum response distribution of bending moment

In previous sections, we calculated the time history of SFT responses. By using these results, we could calculate the bending moment for SFT about each time step. Bending moment is the one of representative factor to check the safety and structure design.

To consider ultimate conditions, we discussed the maximum response distribution of bending moment through the tunnel length. The maximum bending moment was occurred when seismic excitation angle $\theta = 90\deg.$ (i.e. horizontal excitation case).

From Fig. 65., bending moment distribution also satisfy bilateral symmetry between both ends. Assuming that the tunnel is fully fixed at its ends, i.e. displacements are equal to zero and bending moments are non-zero at the tunnel ends.

The maximum value of bending moment is occurred at the tunnel ends. It is described in Table. 5., below.

Table. 5. Magnitudes of maximum bending moment response

	Harmonic	El Centro	Kobe
Max. M_z $(kN \cdot m)$	1.3612E+07	9.4723E+05	2.2492E+06

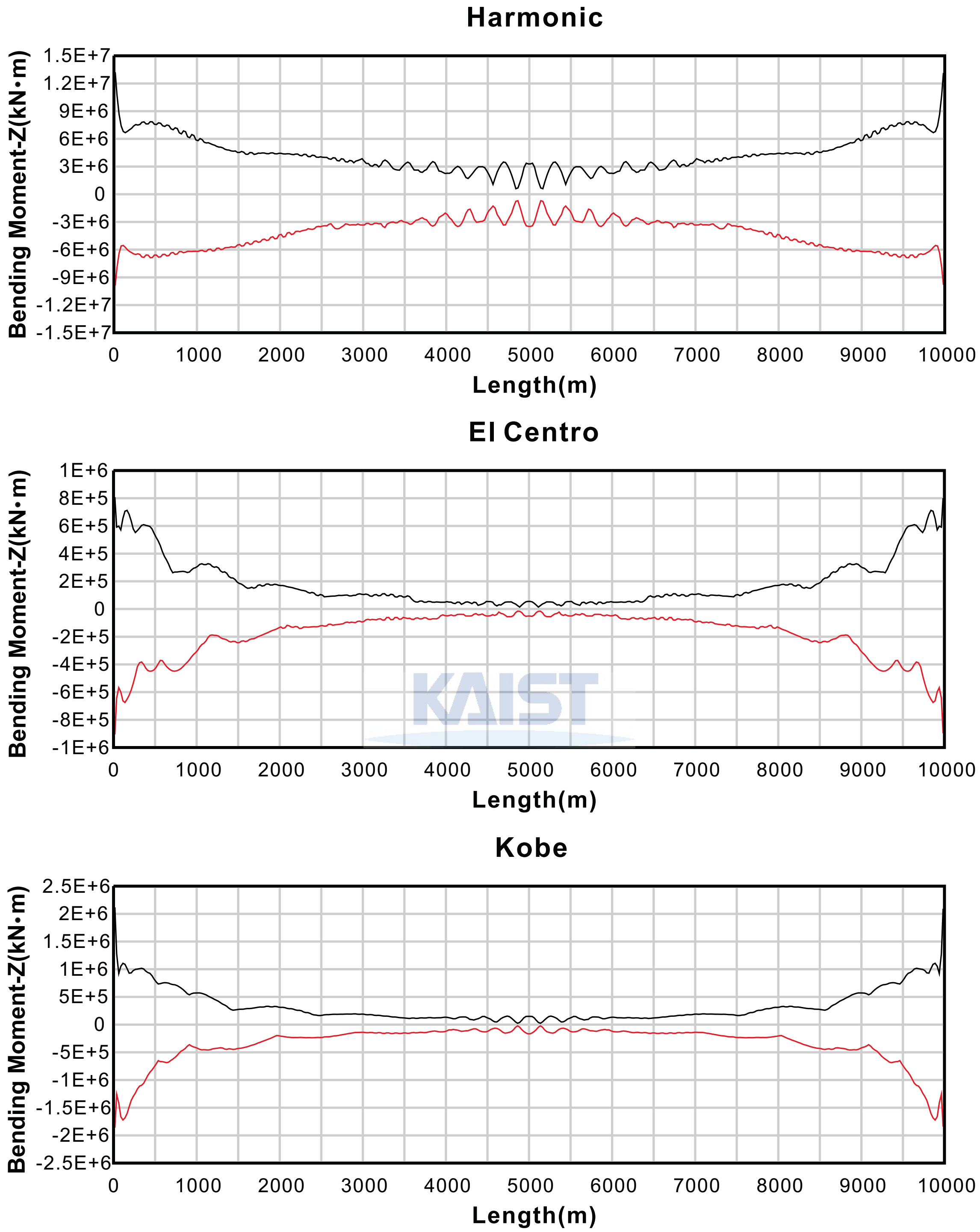

Fig. 65. Maximum response distribution of bending moment for three ground motions

Chapter 5. Conclusion

We developed the mathematical formulation for 3D hydroelastic analysis of tension leg type SFT under seismic ground motion. In order to consider fluid-structure interaction effectively, the present formulation estimated hydrodynamic loadings during seismic ground motion by linearizing the Morison equation. Because the formulation was based on Morison equation, hydrodynamic forces occurred by relative motion between structure, ground and fluid could be simplified. To analyze the dynamic responses of SFT in seismic excitation, we studied numerical methods for solving the developed equation of motion. By applying continuum mechanics based 3-D beam element, we could improve existing SFT dynamic analysis model in previous study. From the improvement of formulation and numerical modeling, we could analyze the macroscopic SFT models which have several kilometers. Several cases which according to change of ground motion and seismic excitation angle are investigated the characteristics of dynamic behavior of SFT model.

Firstly, during seismic analysis in still water, inertial force is dominantly effected to the dynamic responses of SFT compare with drag force. In other words, added mass effect is major difference to change dynamic response.

Secondly, displacement response of SFT is much smaller than its diameter and length. But, for the serviceability and safety for transportation point of view, it needs to be investigated in detail. Especially, the responses of tunnel segments which close by tunnel ends are changed rapidly within short time, so it needs a solutions to reduce dynamic response for safety.

In this study, we used imaginary model of SFT for application because there are no real SFT and plans have several tens of kilometers long like this application model in the world. That is major issue to delay the realization of SFT. Therefore, to obtain more realistic properties of SFT, we need to develop advanced model and verify the effect of fluid-structure interaction at the same time.

References

[1] Martire, G. (2000). “The development of submerged floating tunnels as an innovative solution for waterway crossings”, *Ph.D. Thesis*, University of Naples Federico II, Naples, Italy, 316 pages.

[2] Østlid, H. (2010). "When is SFT competitive?" *Procedia Engineering*, 4, pp. 3-11.

[3] Mazzolani, F. M., Landolfo, R., Faggiano, B., Esposto, M., Perotti, F., Barbella, G. (2008). "Structural Analyses of the Submerged Floating Tunnel Prototype in Qiandao Lake (PR of China)." *Advances in Structural Engineering*, 11(4), pp. 439-454.

[4] Pilato, M. D., Perotti, F., Fogazzi, P. (2008). "3D dynamic response of submerged floating tunnels under seismic and hydrodynamic excitation." *Engineering Structures*, 30(1), pp. 268-281.

[5] Ge, F., Lu, W., Wu, X., Hong, Y. (2010). "Fluid-structure interaction of submerged floating tunnel." *Procedia Engineering*, 4, pp. 263-271.

[6] Martire, G., Faggiano, B., Mazzolani, F.M., Zollo, A., Stabile, T.A. (2010). "Seismic analysis of a SFT solution for the Messina Strait crossing." *Procedia Engineering*, 4, pp. 303-310.

[7] Kunisu, H. (2010). "Evaluation of wave force acting on Submerged Floating Tunnels." *Procedia Engineering*, 4, pp. 99-105.

[8] Martinelli, L., Barbella, G., Feriani, A. (2011). "A numerical procedure for simulating the multi-support seismic response of submerged floating tunnels anchored by cables." *Engineering Structures*, 33(10), pp. 2850-2860.

[9] Brancaleoni, F., Castellani, A., D'Asdia, P. (1989). "The response of submerged tunnels to their environment." *Engineering Structures*, 11(1), pp. 47-56.

[10] Chopra, A. (2007). *Dynamics Of Structures: Theory And Applications To Earthquake Engineering*, Pearson/Prentice Hall, New Jersey, 876 pages.

[11] Yoon, K.H., Lee, Y.G., Lee, P.S. (2012). "A continuum mechanics based 3-D beam finite element with warping displacements and its modeling capabilities." *Structural Engineering and Mechanics*, 43(4), pp. 411-437.

[12] Živkovic, M., Koji , M., Slavkovi , R. and Grujovi , N. (2001). "A general beam finite element with deformable cross-section." *Comput. Meth. Appl. Mech. Eng.*, 190, pp. 2651-2680.

[13] Timoshenko, S.P. and Goodier, J.N., (1970) *Theory of Elasticity*, McGraw Hill, New York, 506 pages.

[14] Bathe, K. J., (1996) *Finite element procedure*, Prentice Hall, New York, 1037 pages.

[15] Long, X., Ge, F., Wang, L., Hong, Y. (2009). "Effects of fundamental structure parameters on dynamic responses of submerged floating tunnel under hydrodynamic loads." *Acta Mechanica Sinica*, 25(3), pp. 335-344.

[16] Lee, Kihwan (2012). "An offshore nuclear power plant mounted on gravity-based structures and its seismic performance", *Master's thesis*, Korea Advanced Institute of Science and Technology, Daejeon, Republic of Korea, 84 pages.

Summary

수중터널의 내진해석을 위한 수치해석기법 개발

지진하중은 계류선으로 지지되어 있는 수중터널(submerged floating tunnel)의 조건으로 인해 그 해석에 어려움이 존재한다. 본 연구에서는 지진하중 작용 시 유체-구조체 상호작용(fluid-structure interaction)을 고려한 수중터널의 3 차원 유탄성 해석 기법을 개발하였다. 지진하중에 의한 유체-구조체 상호작용은 모리슨(Morison)식을 선형화 하여 고려하였으며, 수중터널의 시간영역에서의 유탄성 해석을 수행하였다. 터널은 연속체 역학 기반의 3 차원 보 요소(continuum mechanics based 3-D beam element)를 이용하여 모델링 하였으며, 임의의 제원 및 환경조건을 설정하여 지진파의 종류와 진행방향에 따른 구조물의 동적 거동 특성을 비교 분석 하고자 한다.

핵심어: 3 차원 유탄성 해석 / 수중터널 / 모리슨 식 / 유한요소법 / 내진해석